AFRL-SN-WP-TR-2002-1131

THE ROLE OF ADAPTIVE PHOTOREFRACTIVE POWER LIMITING ON ACOUSTO-OPTIC RADIO FREQUENCY (RF) SIGNAL EXCISION

Dale M. Stevens

Multi-Chip Integration Branch (AFRL/SNDI)
Aerospace Components And Subsystems Technology Division
Sensors Directorate
Air Force Research Laboratory, Air Force Materiel Command
Wright-Patterson Air Force Base, OH 45433-7318

DECEMBER 2001

Final Report for 01 June 1997 – 31 August 2001

SENSORS DIRECTORATE
AIR FORCE RESEARCH LABORATORY
AIR FORCE MATERIEL COMMAND
WRIGHT-PATTERSON AIR FORCE BASE, OH 45433-7318

NOTICE

USING GOVERNMENT DRAWINGS, SPECIFICATIONS, OR OTHER DATA INCLUDED IN THIS DOCUMENT FOR ANY PURPOSE OTHER THAN GOVERNMENT PROCUREMENT DOES NOT IN ANY WAY OBLIGATE THE US GOVERNMENT. THE FACT THAT THE GOVERNMENT FORMULATED OR SUPPLIED THE DRAWINGS, SPECIFICATIONS, OR OTHER DATA DOES NOT LICENSE THE HOLDER OR ANY OTHER PERSON OR CORPORATION; OR CONVEY ANY RIGHTS OR PERMISSION TO MANUFACTURE, USE, OR SELL ANY PATENTED INVENTION THAT MAY RELATE TO THEM.

THIS REPORT IS RELEASABLE TO THE NATIONAL TECHNICAL INFORMATION SERVICE (NTIS). AT NTIS, IT WILL BE AVAILABLE TO THE GENERAL PUBLIC, INCLUDING FOREIGN NATIONS.
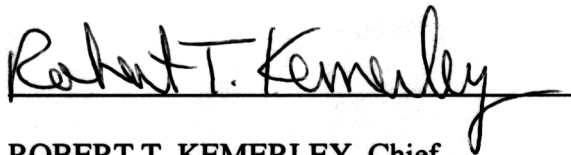
THIS TECHNICAL REPORT HAS BEEN REVIEWED AND IS APPROVED FOR PUBLICATION.

DALE STEVENS, Research Engineer
Multi-Chip Integration Branch
Aerospace Components Division

ALAN J. TEWKSBURY, Chief
Multi-Chip Integration Branch
Aerospace Components Division

ROBERT T. KEMERLEY, Chief
Aerospace Components Division
Sensors Directorate

Do not return copies of this report unless contractual obligations or notice on a specific document require its return.

REPORT DOCUMENTATION PAGE

Form Approved
OMB No. 0704-0188

The public reporting burden for this collection of information is estimated to average 1 hour per response, including the time for reviewing instructions, searching existing data sources, searching existing data sources, gathering and maintaining the data needed, and completing and reviewing the collection of information. Send comments regarding this burden estimate or any other aspect of this collection of information, including suggestions for reducing this burden, to Department of Defense, Washington Headquarters Services, Directorate for Information Operations and Reports (0704-0188), 1215 Jefferson Davis Highway, Suite 1204, Arlington, VA 22202-4302. Respondents should be aware that notwithstanding any other provision of law, no person shall be subject to any penalty for failing to comply with a collection of information if it does not display a currently valid OMB control number. **PLEASE DO NOT RETURN YOUR FORM TO THE ABOVE ADDRESS**.

1. REPORT DATE *(DD-MM-YY)*	2. REPORT TYPE	3. DATES COVERED *(From - To)*
December 2001	Final	06/01/1997 – 08/31/2001

4. TITLE AND SUBTITLE
THE ROLE OF ADAPTIVE PHOTOREFRACTIVE POWER LIMITING ON ACOUSTO-OPTIC RADIO FREQUENCY (RF) SIGNAL EXCISION

5a. CONTRACT NUMBER
IN-HOUSE

5b. GRANT NUMBER

5c. PROGRAM ELEMENT NUMBER
N/A

6. AUTHOR(S)
Dale M. Stevens

5d. PROJECT NUMBER
N/A

5e. TASK NUMBER
N/A

5f. WORK UNIT NUMBER
N/A

7. PERFORMING ORGANIZATION NAME(S) AND ADDRESS(ES)
Multi-Chip Integration Branch (AFRL/SNDI)
Aerospace Components And Subsystems Technology Division
Sensors Directorate
Air Force Research Laboratory, Air Force Materiel Command
Wright-Patterson Air Force Base, OH 45433-7318

8. PERFORMING ORGANIZATION REPORT NUMBER
AFRL-SN-WP-TR-2002-1131

9. SPONSORING/MONITORING AGENCY NAME(S) AND ADDRESS(ES)
Sensors Directorate
Air Force Research Laboratory
Air Force Materiel Command
Wright-Patterson Air Force Base, OH 45433-7318

10. SPONSORING/MONITORING AGENCY ACRONYM(S)
AFRL/SNDI

11. SPONSORING/MONITORING AGENCY REPORT NUMBER(S)
AFRL-SN-WP-TR-2002-1131

12. DISTRIBUTION/AVAILABILITY STATEMENT
Approved for public release; distribution is unlimited.

13. SUPPLEMENTARY NOTES
This material is declared a work of the U. S. Government and is not subject to copyright protection in the United States.
Report contains color.

14. ABSTRACT *(Maximum 200 Words)*
Acousto-optic RF signal excision techniques offer real-time, narrowband RF interference, frequency-domain filtering for broadband communication systems, but has been limited in its capability for adaptive processing and rejection of broadband RF interference. As a means to reduce these limitations, this effort examines the application of a novel photorefractive optical power limiting device to achieve adaptive notch filtering, and multi-channel acousto-optic deflection to achieve angle-of-arrival signal discrimination at the notch filter. This report describes basic principles of acousto-optic RF signal excision, including linear phased-array antenna, angle-of-arrival processing using a multi-channel acousto-optic deflector. The principles are verified experimentally by demonstration of frequency-domain filtering according to frequency and angle of arrival. This report also describes basic principles of photorefractive optical power limiting and gives a numerical solution of the band-transport model, and experimental measurement of notch-filter amplitude and spatial profiles for high-intensity and terminate at the dark-to-light illumination interface where excess charge accumulates. The results show that space and time excision of interference may be achieved, but the adaptive notch-filter width developed by high-intensity RF interference can overwhelm the angle-of-arrival resolution when small antenna arrays are used.

15. SUBJECT TERMS
Fourier optics, optical signal processing, spatial filtering, electro-optic devices, photorefractive nonlinear optics

16. SECURITY CLASSIFICATION OF:			17. LIMITATION OF ABSTRACT:	18. NUMBER OF PAGES	19a. NAME OF RESPONSIBLE PERSON (Monitor)
a. REPORT Unclassified	**b. ABSTRACT** Unclassified	**c. THIS PAGE** Unclassified	SAR	196	Dale M. Stevens **19b. TELEPHONE NUMBER** *(Include Area Code)* (937) 255-4557 x3360

Standard Form 298 (Rev. 8-98)
Prescribed by ANSI Std. Z39-18

Table of Contents

List of Figures

List of Tables

Preface

The Air Force research labs solicited proposals in 1996 to develop methods to reduce interference in broadband communication systems. A proposal received from Rockwell Science Center, authored by John Hong and Tallis Chang, described adaptive acousto-optic RF signal excision using a novel electro-optic power limiter. Because of the Air Force interest, the topic was selected and supported as an AFRL/SNDI in-house research and University of Dayton PhD dissertation project.

Abstract

Adaptive RF interference reduction for broadband communication systems continues to be problematic. The acousto-optic RF signal excision system offers real-time, narrowband RF interference, frequency-domain filtering for broadband communication systems, but has been limited in its capability for adaptive processing and rejection of broadband RF interference. As a means to reduce these limitations, this dissertation examines the application of a novel photorefractive optical power limiting device to achieve adaptive notch filtering, and multi-channel acousto-optic deflection to achieve angle-of-arrival signal discrimination at the notch filter.

This dissertation describes basic principles of acousto-optic RF signal excision, including linear phased-array antenna, angle-of-arrival processing using a multi-channel acousto-optic deflector. The principles are verified experimentally by demonstration of frequency-domain filtering according to frequency and angle of arrival. This dissertation also describes basic principles of photorefractive optical power limiting, which is a new approach for achieving adaptive, frequency-domain notch filtering. Photorefractive field shielding of electro-optic birefringence is examined by numerical solution of the band-transport model, and experimental measurement of notch-filter amplitude and spatial profiles for high-intensity, Gaussian-beam optical illumination and high-intensity, externally applied electric fields. Results indicate that for illumination-beam radius

larger than a few microns, power-limiting notch widths follow the illumination intensity and terminate at the dark-to-light illumination interface where excess charge accumulates. Also, when sufficient light intensity is applied, a space-charge field develops that will completely screen the externally applied E-O modulator half-wave voltage, at which point only a very small diffusion field remains, and the notch-depth limit is the extinction ratio of the polarizer-crystal-analyzer combination.

The theoretical models of the optical power limiting device and acousto-optic RF signal excision system agreed with the experimental results to within 18% for the frequency-domain, notch-filter width. The results show that space and time excision of interference may be achieved, but the adaptive notch-filter width developed by high-intensity RF interference can overwhelm the angle-of-arrival resolution when small antenna arrays are used.

List of Acronyms

A-O   Acousto-Optic

AOA   Angle of Arrival

BSO   Bismuth Silicon Oxide [$Bi_{12}SiO_{20}$]

C/A   Clear/Acquisition

CCD   Charge Coupled Device

CRPA   Controlled Radiation Pattern Antenna

DFT   Discrete Fourier Transform

EO   Electro-Optic

EOPL   Electro-Optic Power Limiter

GPS   Global Positioning System

HOE   Holographic Optical Element

IF   Intermediate Frequency

LO   Local Oscillator

NDF   Neurtral-Density Filter

PR   Photorefractive

RF   Radio Frequency

SLM   Spatial Light Modulator

List of Symbols

A	Amplitude
α	Diffraction angle
β	Rate of thermal excitation, seconds^{-1}
B	Coefficient of photoconductivity
BW	Bandwidth of a signal
cm	Centimeter
C	Coulombs
D	Lens diameter
D	Bragg cell channel width
d	Bragg cell channel-to-channel spacing
Δf	Minimum resolvable frequency
d_r	Antenna array element spacing
Δt	Transit time, Bragg cell
dB	Decibel
dBm	Decibel referenced to one milliwatt
D_n	Diffusivity
D_t	Width of Bragg cell transducer/crystal
E	Electric field
E_{SC}	Space-charge electric field
ϵ_o	Free-space permittivity
ϵ_r	Relative permittivity
f	Focal length of lens
f_x	Frequency, spatial, subscript x-axis (also y-axis, or z-axis)

f_a	Frequency, acoustic
ϕ	Phase
H	Height of Bragg cell transducer/crystal
I_0	Intensity, peak
I_c	Itensity, Control bias
J	Crrent density
k	Optic wavevector
K	Acoustic wavevector
k_b	Boltzmann's constant
KHz	Kilohertz
L	Bragg cell length
λ	Wavelength of light
Λ	Wavelength of sound
λ_{RF}	Wavelength of RF electromagnetic wave
M_2	Material figure of merit, crystal geometry
MHz	Megahertz
mm	Millimeter
μ	Mobility
μm	Micrometer
μsec	Microsecond
N	Number: resolvable spots, Bragg cell, or antenna elements,
N_A	Acceptor concentration $\#/cm^3$
N_D	Donor concentration $\#/cm^3$
nm	Nanometer
P_{ac}	Acoustic power,
q	Magnitude of electron charge
θ	Angle
r	space vector
R	Resistance
s	Ionization cross section per unit photon energy, $cm^2/Joule$,

σ	Conductivity
σ_d	Dark conductivity
T	Temperature degrees Kelvin
t	Time
τ_0	Excess carrier lifetime
υ_a	Acoustic sound velocity
V	Volts
V_π	Half-wave voltage of electro-optic modulator
υ	Frequency RF or acoustic
U	Wavefunction
ω	Radian frequency
W_0	half width of Gaussian beam
W_d	half width of Gaussian beam at value of EOPL dark intensity
W_{dc}	half width of Gaussian beam at value of EOPL control bias intensity
x_f	Space variable, frequency plane, x-axis
y_f	Space variable, frequency plane, y-axis
X	Aperture, x-axis (Bragg cell length in examples)
ξ_p	extinction ratio for polarizer –crystal-analyzer combination

Chapter 1

Executive Summary

1.1 Background

A problem with modern RF systems is their vulnerability to interference sources in a cluttered RF environment.[1] Of particular concern is GPS signal acquisition in the presence of RF interference. Figure 1-1 shows the power levels of high- and low-performance GPS receivers with respect to a baseline 1-watt interference source. The satellite signal level is -130 dBm when it reaches the earth. C/A code acquisition provides 24 dB of processing gain, and can acquire a signal with -106 dBm or less interference intensity. Thus, a 1-watt interference source can disrupt signal acquisition to a distance of about 50 miles. High performance receivers can achieve 54 dB of processing gain, so the same 1-watt interference is only effective to about 1.5 miles. Figure 1-1 shows that with an additional 30 dB of interference suppression, a 1-watt interference source does not disrupt communications except at very close range. The utility of a device that can provide 30dB interference rejection without seriously distorting the desired signal is evident. One solution is to increase the radiated power of the GPS satellites by 30 dB. Such a power increase will occur with GPS modernization.

1
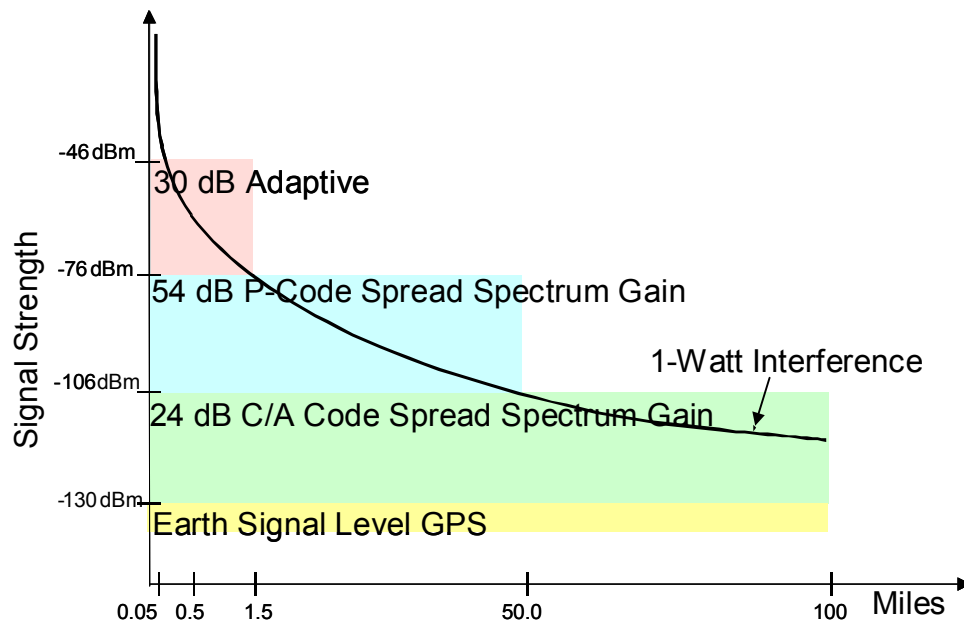
Figure 1-1 Effect of 30 dB adaptive filter on range of 1-watt interference source.

Another solution is to add adaptive filtering. Temporal and spatial adaptive filtering is used.

1.2 Temporal Filtering

Narrowband continuous wave RF interference can be removed using time-correlation filtering or notch filtering, as illustrated in Figure 1-2. In this case the desired signal to be tracked or recovered is contaminated by a large-amplitude, narrowband RF component, which completely precludes valid signal detection or tracking. The adaptive filter must estimate the frequency location of this component and build a notch filter to reduce its amplitude. Digital notch filtering can be used to reject narrowband

Corrupted Signal

Transfer Function

Recovered Signal

f_o

- **Estimate & track frequency of interference**
- **Adapt notch filter response**
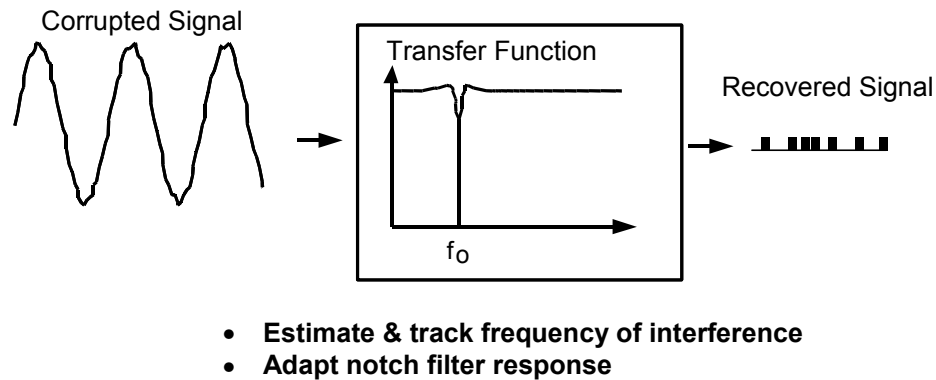
**Figure 1-2 Temporal filtering uses a notch-filter transfer function
to remove interference from corrupted signal.**

interference. A digital simulation of a notch filter communication receiver was

constructed in order to evaluate different system configurations. The results, which are

presented in Section 3.1, Digital Simulation, show that the notch-filtering approach is

effective for removing all types of narrowband interference, except wideband barrage

noise.

An acousto-optic RF signal excision system has potential for providing adaptive,

real-time narrowband RF interference rejection and is the subject of this research. A

brass-board system was constructed in the laboratory in order to test system concepts. A

diagram of the setup is shown in Figure 1-3. A quick explanation of the system follows:

A laser beam is expanded to illuminate a Bragg cell that deflects the light according to

the frequency spectrum of the applied RF signal. The Bragg cell output gives a Fourier

transform of the RF signal represented by a distribution of light intensity located at the

focal plane of the lens. Frequency domain signal processing is achieved since
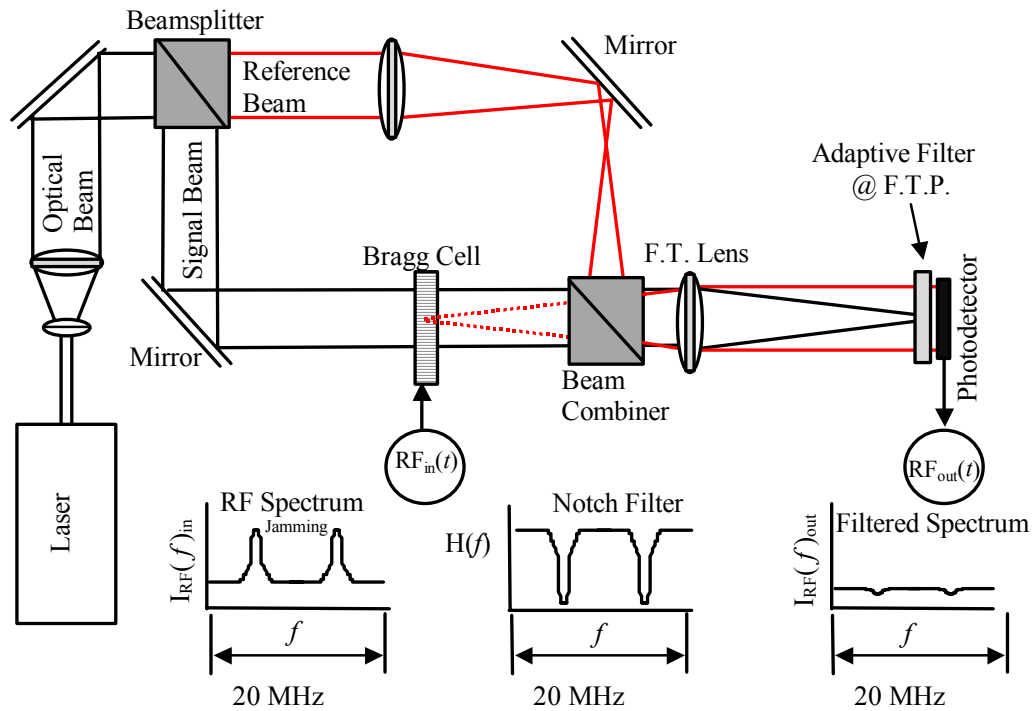
Figure 1-3 Acousto-optic RF signal excision system: Bragg cell RF spectrum analyzer, adaptive notch filter, heterodyne detection from [29].

narrowband RF interference is manifest as bright light that can be adaptively attenuated

by the Electro-Optic Power Limiter (EOPL). The filtered optical signal is demodulated at

the detector, using the reference optical beam. A review of optical signal processing

theory is presented in Section Chapter 2,Linear Systems and Fourier Optics, and a

discussion of acousto-optic RF signal excision is presented in Section 3.2 Acousto-Optic

RF Signal Excision. Results of experimental demonstrations are provided in Chapter

5.1.1 Heterodyne RF Spectrum Analyzer. The results demonstrated feasibility, but

showed that frequency resolution is hindered by depth of focus issues in the EOPL.

1.3 Spatial Filtering

Notch filtering is ineffective against broadband RF interference. Figure 1-4 illustrates an approach for removing broadband RF interference using Controlled Radiation Pattern Antennas (CRPAs). The signals from each antenna element are phase-shifted and combined to produce a composite-gain pattern that places nulls in the directions of the interference sources. The number of spatial nulls that can be formed with spatial filtering is limited to N-1, where N is the number of antenna elements in a receiver array. The number of antenna elements is kept low due to computational burden. While narrow-band interference is a common occurrence in a cluttered RF environment, broadband interference, with its high power requirements, is due to hostile jamming. To remove both types of interference, a combination of temporal and spatial filtering processes is desired so that narrow-band RF interference can be eliminated by efficient notch filtering without using the few spatial null or gain directions available from the CRPA. This need is compounded by the fact that the GPS receiver must be able to lock on to five or more
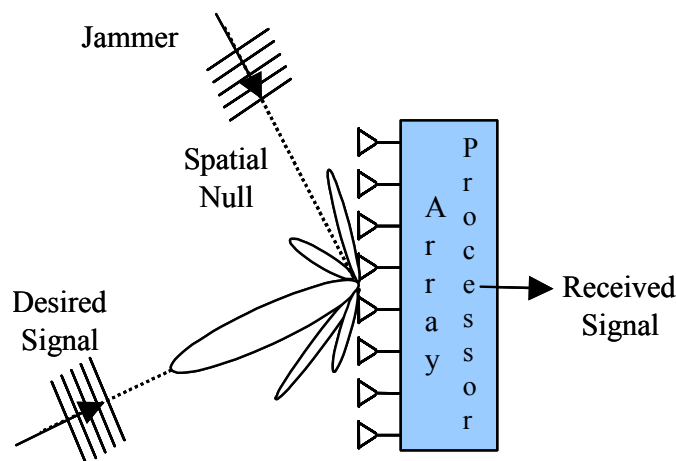
Figure 1-4 Spatial filter uses CRPA to place nulls in direction of RF interference source.

satellites located at different positions in space in order to successfully determine a user's position.

Realizing the advantage a combination of spatial and temporal filtering gives, this research effort investigated the use of a multi-channel Bragg cell in the acousto-optic RF signal excision system in order to achieve a space-time signal processing capability. Figure 1-5 is a conceptual illustration of this approach. The output of a linear antenna array is fed to a multi-channel Bragg cell optical signal processor, which produces a 2-D Fourier transform of instantaneous frequency and Angle Of Arrival (AOA) as a physical distribution of light at the focal plane of a lens. This lens is shown in the figure as a Holographic Optical Element (HOE). The figure shows signal frequency represented along the vertical axis while signal AOA is represented along an orthogonal horizontal axis. An adaptive notch-filter function can excise high intensity broadband RF interference while passing low intensity sources if the AOA separation can be resolved so that each RF source does not overlap. An eight-channel Bragg cell was incorporated into the brass-board RF spectrum analyzer. The results of these experiments are presented in Chapter 5.1.3, Angle-of-Arrival Separation Using Multi-Channel Bragg Cell. The results demonstrated the feasibility of AOA filtering, but showed that when a low number of antenna elements are used, the AOA notch-filter depth is hindered by the increase size of focused spots that occurs for high-intensity beams.

A novel method for achieving a collinear signal- and reference-beam design to reduce phase noise was conceived as part of this research. The approach uses a dual focus illumination beam produced by an HOE, that is not shown in Figure 1-5. The

Angle of Arrival

λ

Fourier
Transform Plane

θ

EOPL Blocks Bright
Broadband Interference

HOE

freq

EOPL
Passes
Spread-
Spectrum
Signal.

φ_1 φ_2 φ_3 • • • φ_n

Phased Array
Receiver

Area
Heterodyne
Detection

← d →

$$\phi = \frac{2\pi d}{\lambda} \sin \theta$$

$\theta = $ AOA

Narrowband Interference
Removed by Optical Power
Limiting Filter

Reference Beam

Signal Beam

Dual Focus
Light Beam

Multichannel
AOM

Micro-Optic Components
Reduce Size to a few square inches.

Figure 1-5 Proposed approach for space/time acousto-optic RF signal excision.

Fourier transform holographic lens, which is shown, is a potential approach to correct

higher order diffraction from the multi-channel Bragg cell. Both concepts were not

pursued beyond the "idea" stage and are suggested for further study in Section6.2,

Recommendations for Future Work.

1.4 Electro-Optical Power Limiter

The Electro-Optical Power Limiter (EOPL) is a novel device that has potential to

improve adaptive notch filtering in optical processing systems. The main thrust of this

dissertation is a study of this novel device for acousto-optic RF signal excision

application. The EOPL was first reported in 1988.[2] The EPOL responds to high-

intensity light by limiting its power. The basic operation of the EOPL is shown in Figure

1-6. A transverse Electro-Optic (EO) modulator is shown for two modes of operation:

low and high optical intensity applied to the crystal. In normal operation the applied half-

wave voltage creates optical birefringence that rotates the polarized optical beam by 90°.

Ideally, all light passes through an analyzer, which is oriented orthogonally to the input

polarization. For the case of high-intensity beams, photoionized charge overcomes

random thermal current, drifts out of the illuminated region, and collects at a dark edge to

create a space-charge field that shields the applied voltage. The EO birefringence is

reduced, and the beam is attenuated at the analyzer.

An objective of this research is to characterize the EOPL with respect to its

suitability as an adaptive frequency plane optical notch filter. To model the EOPL, the

photorefractive band transport theory was applied to the crystal configured as an EO
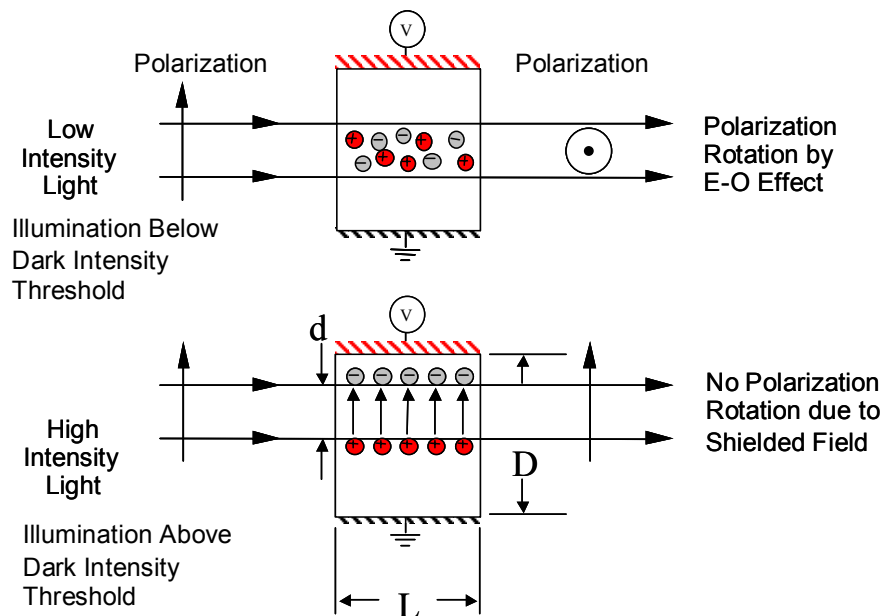
Figure 1-6 Photorefractive electric field shielding in EO modulator.

8

amplitude modulator. The model was then solved numerically. A discussion of the EO

and photorefractive processes is presented in Chapter 4. Results of the modeling are

presented in Sections 4.3.2 and 4.4. An experiment to measure the EOPL notch-filter

width and depth in an acousto-optic RF excision system was performed, and the results

were found to compared closely to the model. Experimental results are presented in

Chapter 5.2, Electro-Optic Power Limiter. The results indicate that trapped photoionized

charge can be confined to narrow regions on the order of a few microns at the dark edges

of illumination, so that electric field spreading is comparable with the optical field

intensity. The frequency-domain filter notch width grows in response to the intensity of

the focused spot and with respect to the dark-intensity threshold, and the notch depth is a

function of the extinction ratio for the crossed polarizers and photorefractive crystal

combination, which is -55 to -45 dB using high quality polarizers and a Bismuth Silicon

Oxide $[Bi_{12}SiO_{20}]$ (BSO) crystal.

Chapter 2

Linear Systems and Fourier Optics

This section describes the mathematical approach used in this dissertation to represent the optical signal processing approach to frequency-domain filtering. It is prudent to balance simplicity and precision when selecting a mathematical model to describe physical phenomena. A simplified model must be consistent with the experimental results to a degree that achieves utility for analyzing new design implementations, as well as a means of better understanding the basic principles involved. For example, the wave diffraction process has accurate differential equation models, but they are difficult to compute. Finite element solutions can be used, but the resulting accuracy is not always justified by the computational burden required to obtain such accuracy. The process of simple harmonic motion for electromagnetic and acoustic propagation enables a simplified mathematical description of these physical phenomena through Fourier analysis and linear systems theory, that has been applied particularly well to the analysis of Acousto-Optic (AO) signal processing systems. Paraxial approximations and small signals apply in most all cases, so that most often the models used in practice involve an analysis of the angular spectrum of plane waves for both optic and acoustic signals. The convenience,

usefulness, and popularity of this approach are compelling reasons for using it wherever possible.

2.1 Basic System Concept

A system analysis involves determining the response of a particular system to a range of inputs. This approach is outlined in Figure 2-1, which shows a system block diagram of input function, system transfer function, and output response.[3,4] The system is defined by a set of equations, usually second-order differential equations. By keeping the description of the model linear and shift invariant, the analysis is greatly simplified through the use of linear systems theory.[5,6] In this case the input is decomposed into a system of orthogonal basis functions (Fourier analysis), the system transfer function is applied to the input functions, which modifies the amplitude and phase of the input basis functions; and the output is obtained by summing the results. This approach is very intuitive because the basis functions are sinusoids and the decomposition is simply the signal spectrum. Figure 1-2 also illustrates this basic approach.

For many optical materials the well known Maxwell's electromagnetic wave equations apply as a set of second-order differential equations with constant coefficients that completely describe the propagation of light within the material. In this case a linear

| Input (f) Eigenfunction Angular Spectrum of Plane Waves | $\times$ | System (f) Amplitude & Phase modulation Notch Filter Transfer Function | Σf | Output (t) Convolution Integral |
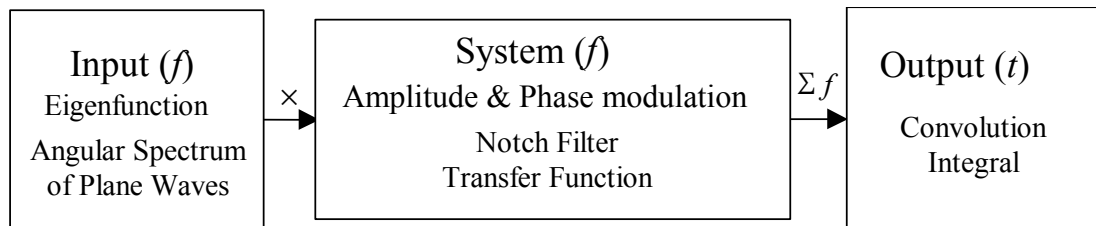
Figure 2-1 Linear system block diagram.

11

systems approach can be applied to analyze optical systems as well as provide a framework to develop an intuitive feel for the physical processes involved. Another advantage is the ease with which linear components such as lenses or transducers can be incorporated into the system description. In addition, this approach is useful for approximating nonlinear systems by examining small regions where linearity can be assumed.

Fourier analysis is the process of decomposing a complicated input function into a spectrum of system eigenfunctions; that is, functions with derivatives proportional to the original functions. Consequently, sinusoidal eigenfunctions are unchanged except in amplitude and phase as they pass through a linear and shift invariant system. By defining a system according to a transfer function that describes the system's amplitude and phase response to a spectrum of eigenfunctions, an analysis of the system output simply involves modifying the amplitude and phase of the input eigenfunctions according to the system transfer function. For filtering systems the transfer function is often described as an notch function having a spectral width and amplitude depth. The phase response, described by lead or lag, generates less interest because it often disappears when intensity is considered.

2.2 Plane Wave Eigenfunctions

In optics an eigenfunction of the propagation equations is recognized as an idealized monochromatic plane wave which is given by the complex function

$$U(\mathbf{r}, t) = A\, e^{j(\omega t - \mathbf{k} \cdot \mathbf{r})} \qquad\qquad (\,2\text{-}1\,)$$

where time variation is indicated by radian frequency $\omega = 2\pi\upsilon = 2\pi/\text{T}$, with frequency, υ and time period, T. Spatial variation is represented by a wave vector $\mathbf{k}$ that defines a propagation direction, and is given by $\mathbf{k} = 2\pi/\lambda(\alpha\mathbf{x}+\beta\mathbf{y}+\gamma\mathbf{z}) = 2\pi(f_x\mathbf{x}+f_y\mathbf{y}+ \sqrt{\lambda^{-2} - f_x^2 - f_y^2}\ \mathbf{z})$, where α, β, and γ are direction cosines, f_x, and f_y are spatial frequencies, and $|\mathbf{k}| = 2\pi/\lambda$. The real part of the complex function in Equation (2-1) is taken to represent an electric or magnetic field. As the name implies, the plane wave has plane surfaces of constant phase normal to the wave vector $\mathbf{k}$ at any instant t, such that

$$\omega t - \mathbf{k} \cdot \mathbf{r} = \text{constant} \qquad\qquad (\,2\text{-}2\,)$$

so that $\mathbf{k} \cdot \mathbf{r} = 2\pi q + \arg\{A\}$, q being an integer which represents wavefronts comprised of planes. That is, the plane wave phase function traces out wavefronts that are parallel planes perpendicular to the direction of propagation, $\mathbf{k}$, and separated by the optical wavelength, λ.

Using the plane wave as a basis function, the representation of any space-time function can be achieved using the space-time and frequency Fourier transform relations, defined as

$$U(x,y,z,t) = \iiint F(\alpha, \beta, \gamma, \upsilon)\, e^{j\frac{2\pi}{\lambda}(\alpha x+\beta y+\gamma z-\upsilon\lambda t)}\, \mathrm{d}\alpha\, \mathrm{d}\beta\, \mathrm{d}\gamma\, \mathrm{d}\upsilon \qquad (\,2\text{-}3\,)$$

$$F(\alpha, \beta, \gamma, \upsilon) = \iiint U(x,y,z,t)\, e^{-j\frac{2\pi}{\lambda}(\alpha x+\beta y+\gamma z-\upsilon\lambda t)}\, \mathrm{d}x\, \mathrm{d}y\, \mathrm{d}z\, \mathrm{d}t. \qquad (\,2\text{-}4\,)$$

Here the representation of any arbitrary space-time function as spectrum of complex sinusoidal components (eigenfunctions) is indicated in Equation (2-3). Equation (2-4) defines the unique spectrum $F(\alpha,\beta,\gamma,\upsilon)$ for the space-time function U(x, y, z, t). Note that the space and time elements of the Fourier transform have opposite signs in the exponent.

The sign conventions are chosen so that the direction of propagation and frequency is in a positive sense (r = z positive z direction). Fourier analysis has found wide use in systems analysis because of the development of a fast computation algorithm for the Fourier transform. The discrete Fourier transform is described in Chapter 3.

Because the frequency components are unchanged in a linear system, it is convenient to use phasor notation when working with idealized monochromatic plane waves by dropping the time dependence in favor of working with just a complex amplitude function. Thus,

$$U(\mathbf{r},t) = U_p(\mathbf{r})e^{j\omega t} \qquad\qquad (2\text{-}5)$$

where

$$U_p(\mathbf{r}) = A(\mathbf{r})e^{j\phi\mathbf{r}} \qquad\qquad (2\text{-}6)$$

is referred to as the complex amplitude. The complex amplitude is composed of real functions a(**r**) and ϕ(**r**) that represent amplitude and phase respectively at position **r**. The optical frequency, ω (known apriori), is now assumed.

2.3 Angular Spectrum of Plane Waves

Optical signal processing systems involve the use of amplitude and phase transparency functions. The analysis of these elements is simplified using the concept of an analysis plane, an optic axis, and the angular spectrum of plane waves. Generally, the optic axis is chosen to be the z-axis and the electric fields of the light are linearly polarized in either the x or y directions. The variation of light amplitude and phase incident upon an x-y analysis plane located at z = 0 can be expressed as a function of only the x and y

coordinates. Equation (2-3) can be rewritten to combine the complex phase components

with regard to an (x,y) analysis plane, with propagation indicated along the z-axis such as

$$U(x,y,z) = F(\alpha,\beta,\gamma)\, e^{j\frac{2\pi}{\lambda}(\alpha \mathbf{x} + \beta \mathbf{y})}\, e^{j\frac{2\pi}{\lambda}\gamma \mathbf{z}}, \qquad\qquad (2\text{-}7)$$

And by choosing z=0, a 2-D phase function results as follows:

$$U(x,y;0) = F(\alpha,\beta,0)\, e^{j\frac{2\pi}{\lambda}(\alpha \mathbf{x} + \beta \mathbf{y})} = F(f_x,f_y)\, e^{j2\pi\left(f_x \mathbf{x} + f_y \mathbf{y}\right)} \qquad (2\text{-}8)$$

The spatial frequencies, $f_x = \alpha/\lambda$ and $f_y = \beta/\lambda$ have a physical interpretation as the spatial

period for plane-wave wavefronts that intersect the analysis plane. That is, a plane wave

traveling with direction vector $\mathbf{k} = \alpha/\lambda\mathbf{x}, +\beta\lambda\mathbf{y} + \sqrt{1-\alpha^2 - \beta^2}\,/\lambda$ has wavefronts that

uniquely intersect the analysis plane according to spatial frequencies $f_x = \alpha/\lambda$ and $f_y = \beta/\lambda$.

This interpretation is illustrated in Figure 2-2. The figure shows a reference plane at z =

0,and a 2-D pattern of lines having spatial separation Λ_x and Λ_y (mm/line) that represent

lines of constant phase for a single plane wave. The spatial frequency components $f_x =$

$1/\Lambda_x$ and $f_y = 1/\Lambda_y$ (lines/mm) define a unique angle of propagation for the plane wave as

indicated by $\mathbf{k}$, where f_x defines a unique angle of propagation in the (x,z) plane, and f_y

defines a unique angle of propagation in the (y,z) plane. If a phase transparency $\phi =$

$n_1\exp[j2\pi(f_x x + f_y y)]$ is illuminated by a plane wave traveling along the optic axis with

wave vector $\mathbf{k} = 2\pi/\lambda\mathbf{z}$ and $f_x = 0, f_y = 0$, the plane wave phase will be modulated by the

spatial components $f_x = \alpha/\lambda$, and $f_y = \beta/\lambda$, and a propagation component with wave vector,

$\mathbf{k} = \alpha/\lambda\mathbf{x}, +\beta\lambda\mathbf{y} + \sqrt{1-\alpha^2 - \beta^2}\,/\lambda$, is generated.
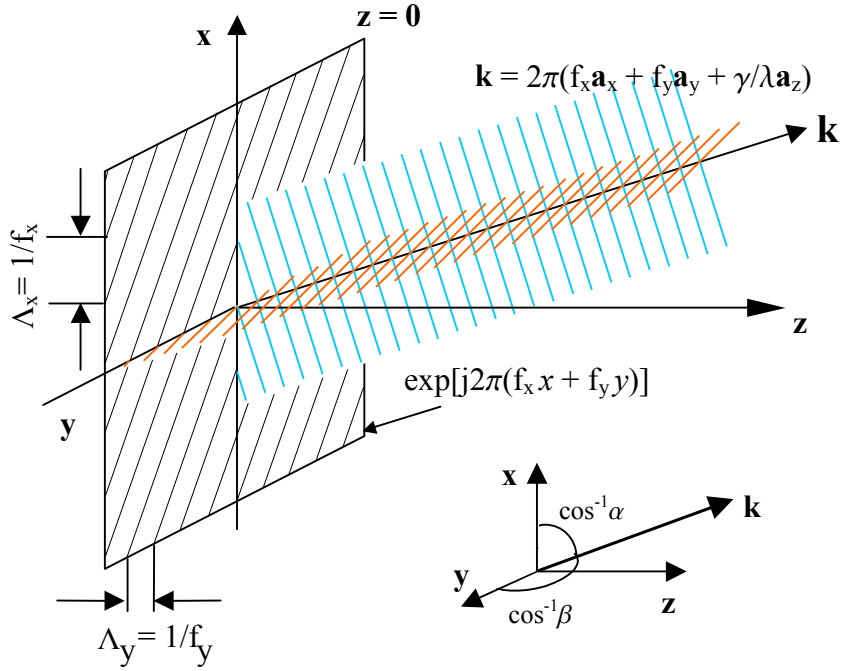
Figure 2-2 Lines of constant phase and spatial frequencies for a plane wave.

A general amplitude or phase transmission function can be defined as

$$t_A(x,y) = \frac{U_i(x,y,0_-)}{U_o(x,y,0_+)} \qquad (2\text{-}9)$$

where a multiplication operation in the spatial domain, $U_o = t_A U_i$, is implied. In order to apply this function to our system analysis model, Equation (2-4) is used to obtain a Fourier transform of the transmission function. In the frequency domain, the multiplication operation in Equation (2-9) becomes a convolution operation

$$A_{out}(f_x, f_y) = A_{in}(f_x, f_y) \otimes T(f_x, f_y). \qquad (2\text{-}10)$$

As an example, an A-O modulator can be represented by a sinusoidal phase transmittance function. A bounded transmittance function is required to represent the A-O cell aperture. The transmittance function for an idealized 2-D A-O cell is

$$T_A(f_x, f_y) = A_{AO}(f_x, f_y) \otimes T_W(f_x, f_y)$$

(2-11)

where $A_{AO}(f_x, f_y)$ represents a spatial phase function in the A-O cell and $T_W(f_x, f_y)$ represents the Fourier transform of the aperture function that truncates the plane wave illumination. As is discussed in Section 3.2.1.2, the frequency component f_x is associated with the RF signal spectrum of ultrasonic acoustic waves created in the A-O cell, and f_y is associated with the AOA phase offset for each channel in an antenna array. It should be apparent that when illuminated by an optical plane wave, the spatial distribution of phase within the transmittance function creates a light component that propagates with unique angular spectrum $\mathbf{k}(f_x, f_y)$. Higher orders can be generated as described in Chapter 3.2.1, Acousto-Optic Modulation.

2.4 Optical Transfer Function

In the previous section it was shown that input functions to optical systems that have been decomposed into a system of sinusoidal eigenfunctions can be interpreted as an angular spectrum of optical plane waves. The optical system transfer function is now examined. A transfer function for free space optical propagation is a well-known result obtained by finding solutions to the Helmholtz optical wave equation, The Helmholtz equation is derived from Maxwell's equations and applies to time-independent wave functions such as those given in Equation (2-7). The Helmholtz optical wave equation is given by

$$\Delta^2 U + k^2 U = 0 \qquad\qquad (\text{2-12})$$

where Δ^2 is the Laplacian operator. Solving for the z dependence using Equations (2-7) and (2-8) gives the result[5]

$$\frac{A_z(f_x, f_y; z)}{A_0(f_x, f_y; 0)} = e^{j \pm \frac{2\pi}{\lambda} \gamma z} = e^{j \pm k z \sqrt{1 - (\lambda f_x)^2 - (\lambda f_y)^2}} \qquad\qquad (\text{2-13})$$

where the + sign indicates positive propagation. This result shows the relative phase change of the plane wave for propagation over a distance z. The radical provides two fundamental solutions for the cases $(\lambda f_x)^2 + (\lambda f_y)^2 < 1$, which retains a complex exponent, and $(\lambda f_x)^2 + (\lambda f_y)^2 > 1$, which gives a real exponent and results in an evanescent wave with rapid attenuation.

When the propagation angles are small relative to the optic axis, Equation (2-13) can be simplified by using the paraxial approximation $\sqrt{1+x} \approx x/2$ for x << 1. Note that the paraxial approximation will always apply to the diffraction angles that are the subject of this dissertation. Applying the paraxial approximation to Equation (2-13) gives

$$\frac{A_z(f_x, f_y; z)}{A_0(f_x, f_y; 0)} = H(f_x, f_y) \approx e^{jkz} \, e^{-j\pi\lambda z(f_x^2 + f_y^2)} . \qquad\qquad (\text{2-14})$$

This result shows the phase relationship between the angular plane wave spectrum at the input and output analysis planes for free space propagation. In order to obtain the light distribution at the plane of interest, $z = z_1$, an inverse Fourier transform of $A_z(f_x, f_y)$ is required.

2.5 Fourier Transform Using a Lens

The plane-wave wavefronts that compose the optical signals converge at infinity so that

the angular spectrum of plane waves forms a spatial distribution of light that is

proportional to a Fourier transform in the far field, or the region of Fraunhofer

diffraction. Frequency-domain optical signal processing takes advantage of the fact that

this result is also found at a more convenient location, that is, the focal plane of a

properly configured lens. The ideal lens configuration for obtaining a Fourier transform

is shown in Figure 2-3. As an example, a truncated plane wave object (an input) placed a

focal length in front of the lens is imaged at the back focal length of the lens in the shape

of a sinc function; that is, an exact Fourier transform of the input object. This result is

obtained in the following manner.[5,7] The relationship between the field at $z = d_0$ and the

spatial frequency function $A_0(f_x, f_y)$ at $z = 0$ involves only the phase function for free
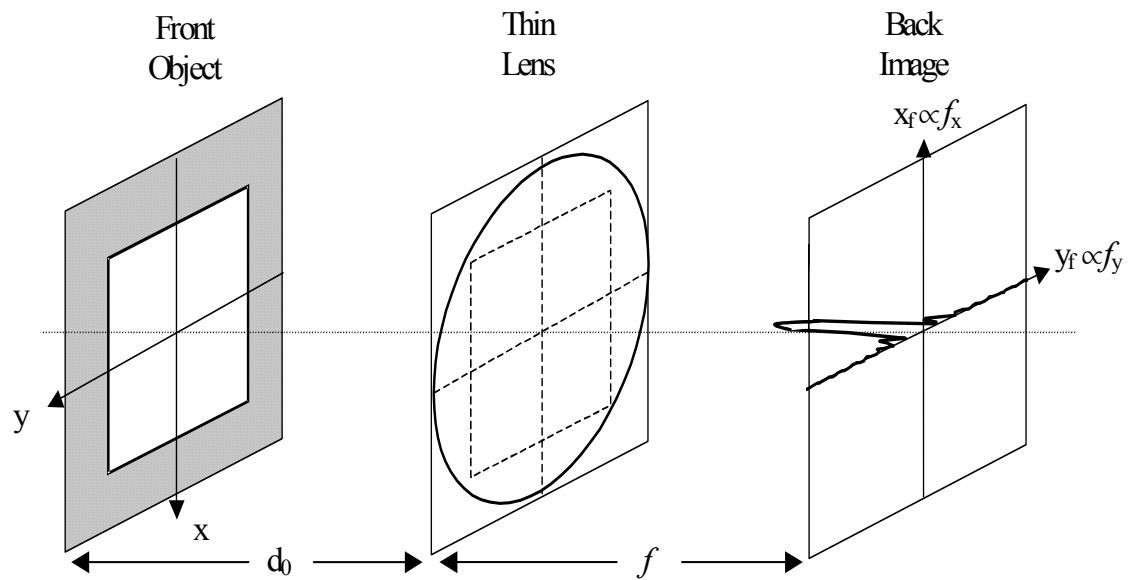
Figure 2-3 Object position for exact Fourier transform using a positive lens, $d_0 = f$.

space light propagation, as given by Equation (2-14) and repeated here for the case of

z=d_0,

$$A_l(f_x, f_y) = A_0(f_x, f_y) e^{jk d_0} e^{-j\pi\lambda d_0 (f_x^2 + f_y^2)}.$$
(2-15)

Using a paraxial approximation, the quadratic phase factor for a thin lens is

$$U_l = e^{-j\frac{k}{2f}(x^2 + y^2)}$$
(2-16)

where the lens focal length is f. The light distribution immediately behind the lens is given by

$$U_l'(x, y) = e^{-j\frac{k}{2f}(x^2 + y^2)} \mathfrak{I}_{xy}^{-1} \left\{ A_0(f_x, f_y) e^{jk d_0} e^{-j\pi\lambda d_0 (f_x^2 + f_y^2)} \right\}.$$
(2-17)

An expression for the light distribution at the back focal plane of the lens is obtained using the Fresnel diffraction integral, which is given as

$$U(x, y) = \frac{e^{jkz}}{j\lambda z} e^{j\frac{k}{2z}(x^2 + y^2)} \iint \left\{ U(\xi, \eta) e^{j\frac{k}{2z}(\xi^2 + \eta^2)} \right\} e^{-j\frac{2\pi}{\lambda z}(x\xi + y\eta)} \, d\xi, d\eta.$$
(2-18)

It is seen that the result contains a Fourier transform of two terms, enclosed in brackets, the complex field U(ξ, η) and a quadratic phase exponential. The quadratic phase term will be canceled exactly by the quadratic phase of the thin lens, as the next step shows. By substituting Equation (2-17) into Equation (2-18) for z=f, the lens focal length, propagation from d_0 to the back focal plane of the lens, gives the expression

$$U_f(x, y) = \frac{e^{jkf}}{j\lambda f} e^{j\frac{k}{2f}(x^2 + y^2)} \mathfrak{I}_{xy} \left\{ \mathfrak{I}_{xy}^{-1} \left\{ A_0(f_x, f_y) e^{jk d_0} e^{-j\pi\lambda d_0 (f_x^2 + f_y^2)} \right\} \right\}_{\substack{f_x = x/\lambda f \\ f_y = y/\lambda f}}.$$
(2-19)

Equation (2-19) reduces further to

$$U_f(x,y)=\frac{e^{jk\,f+d_0}}{j\lambda f}\,e^{j\frac{k}{2f}\left(1-\frac{d_0}{f}\right)(x^2+y^2)}\,A_0(\frac{x}{\lambda f},\frac{y}{\lambda f})\qquad(\,2\text{-}20\,)$$

which shows that a true Fourier transform is obtained at the image plane when $d_0=f$. The

remaining phase term disappears when light intensity is considered.

The scaling relationships used above between spatial frequency f_x and f_y and the

coordinates of the (x,y) analysis plane arise from the direction cosines for the plane wave

vector $\mathbf{k}(\alpha,\beta,\gamma)$. A common result in optics is the inverse relation between diffraction

angle and aperture, $\sin\alpha=\lambda_0/\Lambda_x$, and this result is seen in the following relationships for

spatial frequency:

$$f_x=\frac{\sin\alpha}{\lambda}\approx\frac{x}{\lambda z}\ ;\ f_y=\frac{\sin\beta}{\lambda}\approx\frac{y}{\lambda z}\qquad(\,2\text{-}21\,)$$

where often the case $z=f$ applies for the lens focal length. It is evident that the physical

size of the Fourier transform distribution of light is a function of the lens focal length,

which, in turn, establishes the system length. Size is an important criterion for system

application, and the focal length of the acousto-optic RF excision system cannot be

picked arbitrarily. The focal length is dependent on the adaptive filter device used at the

Fourier transform plane and its (1) capability to resolve optical spatial frequency, and (2)

requirement for depth of focus to achieve adaptive power limiting. Another factor

affecting the size of the system with respect to width and height is the resolvability of the

frequency components in the (x,y) analysis plane, which is the topic of the next section.

2.6 Resolution and Space Bandwidth Product

A key specification for the performance of a filter system is signal resolution, which is a fundamental result of the length of the sample time, or the size of the sample space. As will be shown is Section 3.1, the A-O modulator is an optically addressed, tapped delay line which is used to sample an RF time signal $f(t)$ and spatially and temporally modulate the signal onto an optical carrier $U_o(x,y,z)$. The RF signal applied to the A-O crystal modulates the refractive index to create a spatial phase distribution function such as

$$f(x,t) = e^{j\phi\left(t-\frac{x}{v_a}\right)}$$

(2-22)

where ϕ is an optical phase modulation function proportional to the applied signal, and v_a is the acoustic velocity. For example $\phi(t,x) = \cos[\omega(t-x/v_a)]$ is a sinusoidal wave function propagating across the crystal, and the time signal with radian frequency ω is converted to a distribution of spatial frequency with wavelength $\Lambda = 2\pi v_a/\omega$. As time progresses, new sections of the signal are introduced into the object plane that modulates the light carrier, and the signal spectrum is obtained as a continuous function of time. The sample time of the signal, Δt, is determined by the aperture size X (A-O modulator length) divided by the velocity of sound in the crystal v_a, given as

$$\Delta t = \frac{X}{v_a} \quad .$$

(2-23)

The conversion of temporal frequency to spatial frequency is a function of the sound velocity in the A-O crystal, and the inverse relation shows that a slower acoustic velocity increases the sample time for better RF resolution. The remarkable statement of the

uncertainty principle given by the sampling theorem is that the inverse relationship

between time and frequency $\Delta t = 1 \div \Delta f_t$ (or space and frequency $\Delta x = 1 \div \Delta f_x$) requires that

the sampling width Δt (or Δx) and resolvability of temporal frequency, Δf_t (or spatial

frequency Δf_x) cannot be made arbitrarily small simultaneously. Therefore, to obtain

smaller resolution of signal frequency requires signal sampling over a larger time period

Δt (for most practical purposes). Thus, for a minimum RF signal resolution, Δf_t, the

minimum resolvable spatial frequency is

$$\Delta f_a = \frac{\Delta f_t}{v_a} = \frac{1}{\Delta \Lambda_a} = \frac{1}{X} \qquad (\,2\text{-}24\,)$$

where Δf_a is the smallest detectable change in the spatial frequency that is displayed

within the A-O modulator aperture, and a little hand waving gave $X = \Delta \Lambda_a$ which will be

discussed further. The minimum detectable diffraction angle is

$$\sin \theta = \frac{1}{X} = \frac{\lambda}{\Delta \Lambda_a} = \frac{\lambda \, \Delta f_a}{v_a}. \qquad (\,2\text{-}25\,)$$

Figure 2-4 illustrates the principle of the Rayleigh resolution criterion and spatial

frequency resolution. The Fourier transform of the rectangular aperture function that

represents the time aperture for an illuminated phase grating is a sinc function given by

$$\mathrm{rect}\!\left(\frac{x}{X}\right) \Leftrightarrow X \, \mathrm{sinc}(X \, f_x) \qquad (\,2\text{-}26\,)$$

where X is the width of the aperture, and sinc $(x) \equiv \sin(x)/x$. The Fourier transform of

the idealized infinite extent phase grating is a Kronecker delta function located at position

$x_f = f_x \lambda z = \lambda z / \Lambda_x$ where $z = f$ at the focal plane and the distance coordinate at the Fourier
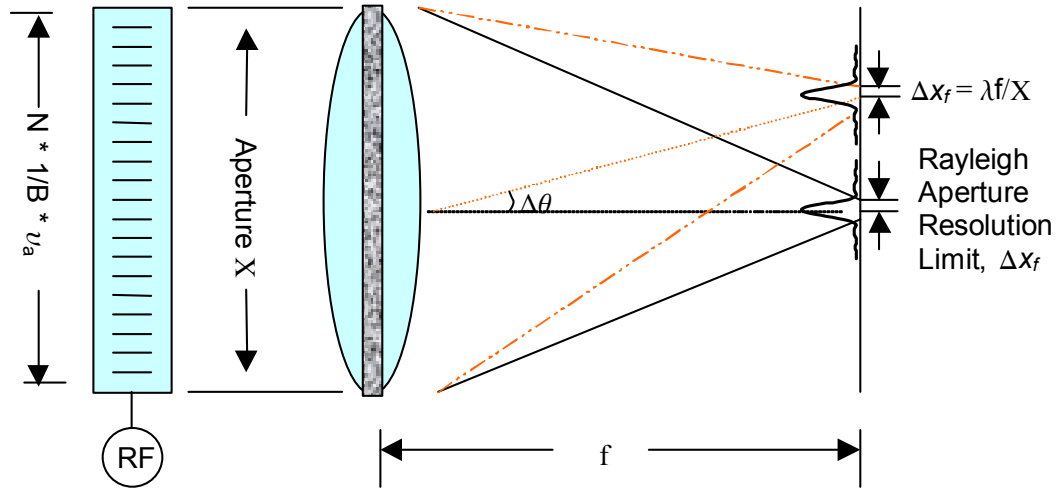
Figure 2-4 Rayleigh resolution for aperture and acoustic phase grating using a lens.

transform plane is designated x_f. The delta function is convolved with the aperture sinc function and the result is a sinc function displaced from the center of the z-axis by an amount x_f. The Rayleigh resolution criterion states that the minimum resolution between two sinc functions occurs when the peak of the second sinc function is aligned with the minimum of the first sinc function, as shown in Figure 2-5. The first minimum of a sinc^2 function occurs at $\text{sinc}^2(1) = 0$, so solving for the minimum intensity, $Xf_x = Xx_{f\text{-min}}/\lambda f = 1$ gives $x_{f\text{-min}} = \Delta x_f = \lambda f/X$. Thus, the minimum resolvable spatial frequency is $\Delta f_x = \Delta x_f/\lambda f$, which when applied to Equation (2-21) gives $\Delta f_x = 1/X$.

As an example, the aperture size required to resolve a given spatial frequency with 1% accuracy requires $\Delta f_x = 0.01 f_x = 1/100\Lambda_x$. That is, $X = 100\Lambda_x$, or in words , 100 cycles of spatial frequency must be presented within the aperture to resolve the frequency to within 1/100 cycles.
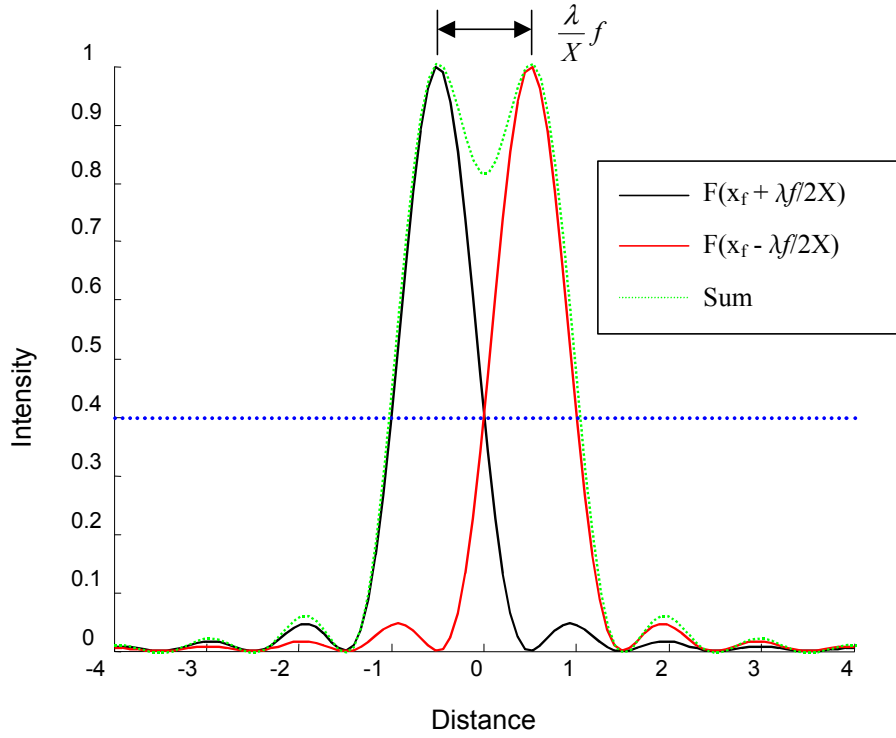
Figure 2-5 Rayleigh resolution criterion for sinc function profiles.

The signal bandwidth, BW divided by the number of resolvable frequencies is the

number of resolvable spots that can be imaged in the Fourier transform plane, and is

known as the time bandwidth product

$$N = \frac{BW}{\Delta f} = BW\Delta t.$$ (2-27)

The time bandwidth product is a useful measure of resolution for A-O cells. This

resolution criterion was used to calculate the collimated beam width for the experimental

system demonstration as follows: the spread spectrum communication system has

bandwidth, BW = 20 MHz, and 0.5% signal resolution, or 200 spots, was desired. The

sample time is N/B = 200/20MHz = 10 μ sec, and the time aperture is X = $\Delta t \upsilon_a$ = 10 μ sec

25

$\times$ 0.62 mm/μ sec = 6.2 mm, (using TeO$_2$, A-O cell, slow acoustic wave). Beam deflection is a continuous function of the input voltage power spectrum; however, the spot width versus deflection distance for a given frequency prevents the resolution of any two nearby spectral components by better than BW/200. As was mentioned at the end of the previous section, for notch filtering, the focal length of the lens, f, determines the resolvable spot size, $2\Delta x_f = 2\lambda f/X$, at the Fourier transform plane and is selected to match the spatial resolution limitations of the notch filter. The photorefractive power limiter also has a depth of focus issue, see Equation (4-10), which is a function of the spot size and hence the lens focal length.

Thus, the working definition for Bragg cell frequency resolution is $\Delta f = 1/\Delta t = 1/$[Bragg cell time aperture], but for notch filtering, the resolution criteria must be adjusted to account for the disparity between beam size and intensity. When signal intensity increases by 14 dB, as shown in Figure 2-6, the energy in the side lobes increases and washes out the peak of the neighboring spot. As will be shown in Section 3.2.3, the optimized system response, H(f), for an optical RF excision systems requires Gaussian apodization of the illumination function in order to minimize the energy in the sidebands. Also the frequency resolution criterion increases to 3Δf for 30 dB excision, and 4Δf for 40 dB excision. This effect is also discussed in Section 4.3.2.3 because the optical power limiting threshold has a similar response to high-intensity beams.

The first-order model for an A-O modulator (see Section 3.2.1.1) assumes constant phase along the y-axis. Multi-channel A-O modulators have parallel channels that can be used to display phase difference between signals as spatial variation in the y-

26
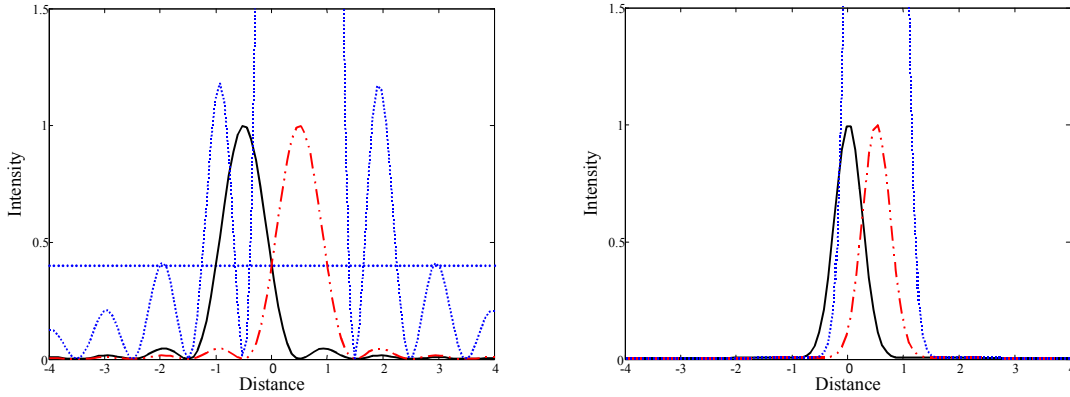
Figure 2-6 Δ*t* resolution criterion increases with intensity disparity. (a) Sinc function, (b) Gaussian function, clipped beam has 14 dB greater intensity.

axis. Figure 2-7 illustrates an idealized multi-channel A-O modulator and "effective lines of phase" wavefronts (shown by the light-colored lines) that are intended to be consistent with the f_x & f_y spatial frequencies illustrated in Figure 2-2. The difference in phase, ϕ, between each channel, see Equation (3-12), creates an effective f_y component that can obviously be resolved into higher orders, as shown in the figure by the second set of dashed lines. Following the procedure outlined thus far, the highest angular deflection at the focal plane for the first order phase lines is limited by the width of each channel, $\alpha_{f\text{-}max}$ = λ/d, and the minimum resolvability of each peak is a function of the total width; that is, the number of channels times the width of each channel, N×d, so that $\alpha_{f\text{-}min}$ = λ/Nd. The number of resolvable channels is therefore $\alpha_{f\text{-}max\,/}\,\alpha_{f\text{-}min}$ = N, the number of channels used. The number of resolvable degrees of phase is 180/N. The higher orders are described in Section 3.2.1.2; however, this simple analysis gave an accurate measure for the position of first-order diffraction beams obtained experimentally and shown in Figure 5-10 through Figure 5-12.
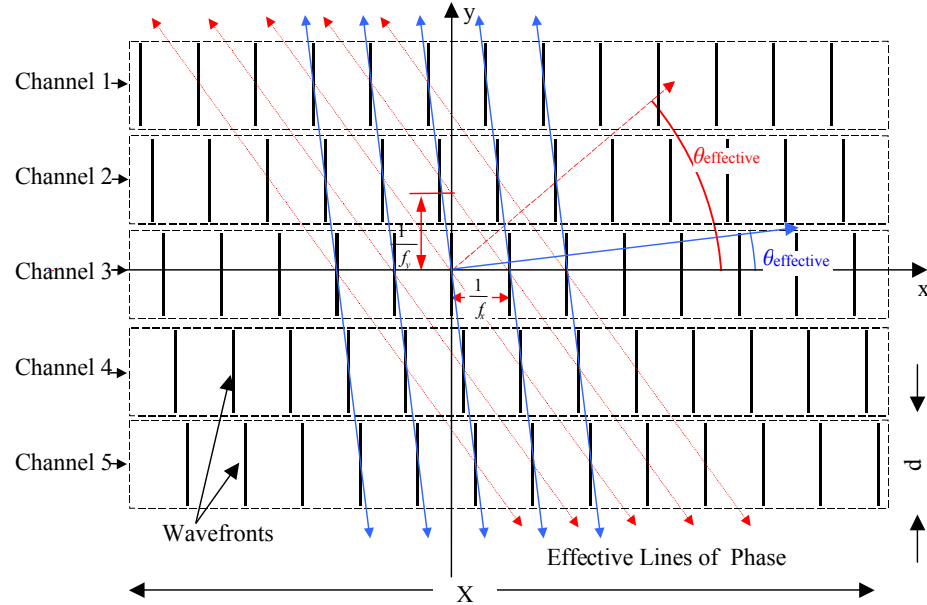
Figure 2-7 Linear array antenna phase relationships show effective lines of phase and AOA for two orders.

This chapter has provided an overview of the optical signal processor from a perspective of linear systems and the angular spectrum of plane waves. It shows that a time signal can be sampled and represented by a spatial frequency spectrum located at the Fourier transform plane. Phase differences between multiple channels, associated with linear AOA, can be displayed as a two-dimensional function of spatial frequency. The next chapter discusses how signal filtering is achieved by implementing a notched-transparency function at the Fourier transform plane that provides amplitude attenuation for selected spectral components.

Chapter 3

Frequency Plane Filter Signal Excision

This chapter provides an overview of the frequency domain signal excision process that is used to reject unwanted spectral components from broadband signals. Two signal excision approaches are discussed: digital signal processing and analog optical signal processing. With the advent of high-speed digital processors, digital signal processing is a good choice for many applications. Analog electronic and optical devices are now playing supporting roles as hybrid processors that add size and cost and are therefore used only where better performance pays. Time will tell how long this digital advantage will last, and what developments will advance the promise of optical processing.

Because of the flexibility and pervasiveness of digital tools used to simulate physical systems, a digital simulation of the acousto-optic RF signal excision system was programmed and used in this research to examine the expected performance of the analog optical system.[8,9] The same key algorithm is shared by the digital and A-O approaches: Fourier transform, frequency filtering, and inverse Fourier transform; therefore, a single chapter is used to describe both topics.

3.1 Digital Simulation

This section describes a digital simulation of the acousto-optic RF signal excision system. The objective of the simulation is to investigate the effects of (1) notch filtering on signal integrity (2) a multi-channel Angle Of Arrival (AOA) approach to broadband RF interference reduction.

The digital simulations used to model the signal excision system are similar to actual digital filters used in receivers. In fact, fully software-based receivers are being developed. The single-channel digital computations can be achieved at acceptable speeds and are an obvious choice for digital receivers; however, the multi-channel optical parallel processor offers a computational advantage with regard to dense narrowband and broadband RF interference environments.

Results of the digital simulation are shown in Figure 3-3 through Figure 3-6. The Matlab® code[10] is provided in Appendix B, along with a more complete description of the process involved in writing the code. The results show that the single-channel, temporal notch filter is effective against narrowband RF interference, but not effective against broadband interference, where the adaptive filter clips most all frequencies of the signal. The simulations also show that adding a multi-channel AOA capability to the temporal filter is effective for rejecting broadband interference.

3.1.1 Temporal Filter

Figure 3-1 is a box diagram showing three parts of a spread spectrum digital communication system: transmitter, communications channel, and receiver. The best
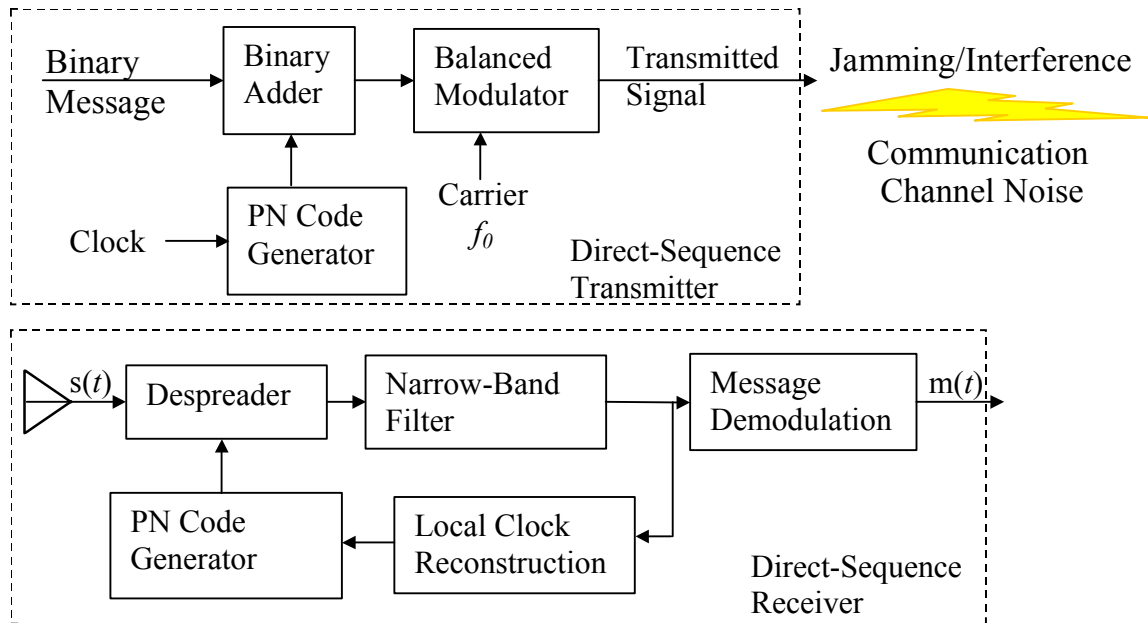
Figure 3-1 Block diagram of spread spectrum communications system, from [9].

insertion point for the acousto-optic RF signal excision system is at the first Intermediate

Frequency (IF) of the GPS signal, which is centered at 173 MHz. This frequency is

available as an output on some older GPS military receivers. An optimum Bragg cell

center frequency is 40 MHz, so further down conversion might be desired to process the

signal acousto-optically. The baseband signal has a bandwidth of slightly over 20 MHz.

These values are represented digitally by a "relative" minimum resolution of [20 MHz

bandwidth÷200 spots] = 100KHz, and calculations were not actually performed at these

rates.

The digital simulation was constructed using discrete models of each system

component, most of which are shown in Figure 3-2. The following components were

modeled: (1) An input signal is represented by a unique PN sequence of amplitude ±1,

mixed with sinusoidal interference, resolvable to 200 frequencies. (2) The Bragg cell time

Input Signal

N - Tap Delay Line

N Sample DFT

Frequency Domain

Array of Power Limiting Devices

Summing Amplifier

Filtered Output Signal (time domain)

Output f(a)

Output Suppression

$f(a) = a$

$f(a) = G$

$F(a) = a - a(a_2 - a_1)$

Input Limiting Range $(a_2 - a_1)$ dB

a_1

a_2

Input a
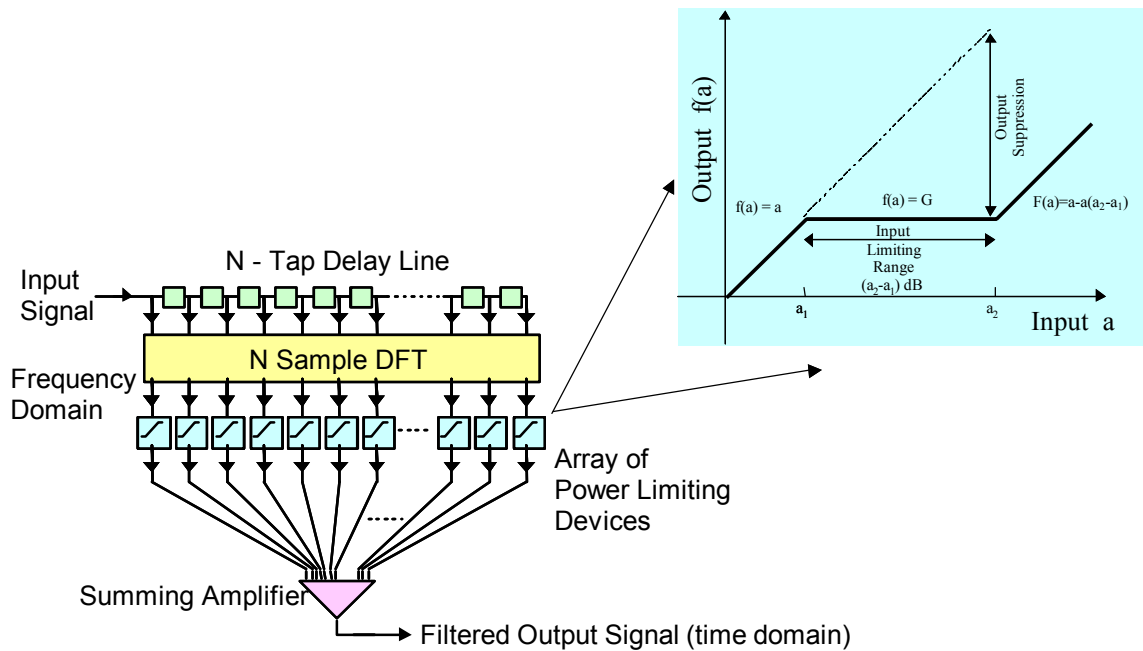
Figure 3-2 Discrete model for temporal filter; N-tap delay line, discrete Fourier transform, adaptive filter algorithm, summing amplifier.

sampling is represented by a tapped delay line long enough to resolve the highest

sinusoidal frequency.[11] (3) The Fourier transform provided by the Bragg cell deflection &

optic lens is represented by a discrete Fourier transform operation. (4) The EO power

limiting is represented by a logic function. (5) Heterodyne detection and inverse Fourier

transform is represented by summing all the signal frequency components. (6) Receiver

decoding is represented by a correlation operation, and the correlation coefficient was

used to assess the effectiveness of the interference rejection.

In order to simulate real-time sampling, the code+interference is input into the n-

tap delay line one bit at a time. The RF spectrum of the input signal is obtained using the

Discrete Fourier Transform (DFT) operation that is part of the Matlab package. The

frequency resolution for the DFT operation is consistent with the time aperture

requirements (number of illuminated grating lines) of the Bragg cell. At each time step

that the input signal is clocked into the tapped delay, a DFT is taken of the N bit

sequence. The DFT represents the Fourier transform plane of the optic lens where the

frequency filter is placed. Matlab computes the DFT of a length N vector x(n)

accordingly:

$$X(k) = \sum_{n=1}^{N} x(n) e^{-j2\pi (k-1)\left(\frac{n-1}{N}\right)}$$
(3-1)

where X(k) is an N length vector. Though not used in this simulation, the inverse DFT is

given by

$$x(n) = \frac{1}{N} \sum_{n=1}^{N} X(k) e^{j2\pi (k-1)\left(\frac{n-1}{N}\right)}.$$
(3-2)

The E-O power limiter is modeled by a subroutine called nonlinear. Each

frequency component from the Fourier transform is examined by the subroutine and

modified according to the power limiting transfer function: maps one-to-one unless a

value X_0 is exceeded, values that exceed X_0 are attenuated according to intensity, $Y_{out}(i)$

$= X_0^2 \times Y_{in}(i) \div Y_{in}(i)^2$, the bigger $Y_{in}(i)$ gets the smaller $Y_{out}(i)$ becomes. A function that

accounts for analyzer leakage at the polarizer extinction ratio limit, $\xi_p = X_1$, is included in

the logic: $Y_{out}(i) = (X_0^2/X_1^2) \times Y_{in}(i)$. After the logical filter operation, the filtered time

signal is recovered for each "real time" step by summing all frequency components. The

effectiveness of the filtering is determined by correlating the recovered signal with the

original PN code. Figure 3-3 shows the effect of frequency filtering on the ability to

correlate a known PN sequence that has been corrupted with four narrowband

interference components. The correlation plot gives the correlation coefficient for each

33

time value of the signal, and the peak occurs at the position where the signal PN and

stored PN code matched in time. In the figure, the filtered output shows that the ±1

signal amplitude levels were recovered by filtering, while the unfiltered output is

identical to the "noisy" signal. The correlation plot for unfiltered signal shows no

correlation peak, while the filtered signal had almost exact correlation. The filtering

operation was repeated as more and more high intensity spectral components were added.

Figure 3-4 shows a plot of the correlation coefficient versus the number of frequency

bands that were intense enough to trigger filtering. Note that without filtering, a single
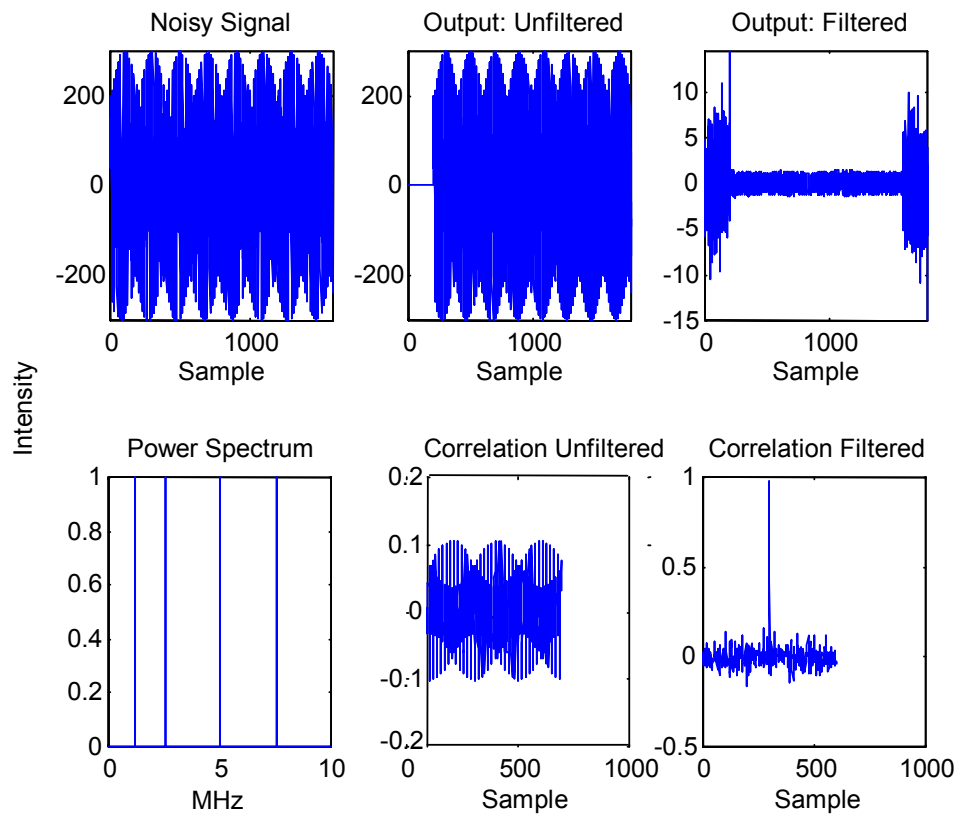
Figure 3-3 Digital simulation results for temporal filter: noisy signal, power spectrum, filtered & unfiltered output, filtered & unfiltered correlation.

high intensity spectral component prevented correlation; however, with filtering 10% of the band is filled before a noticeable decrease in the correlation coefficient occurs, and over 50% of the frequency band can be filtered before a significant degradation of PN sequence correlation occurs. The "Not Filtered" plot was only carried out for 15 cases. The plot in Figure 3-4 was done to examine the effect of broadband interference on a spectral compression filter. Two different models for the power compressor were investigated: (1) completely blocking the signal and (2) power limiting while preserving phase. There was no difference between these two models as shown by the two lines plotted in the lower graph.
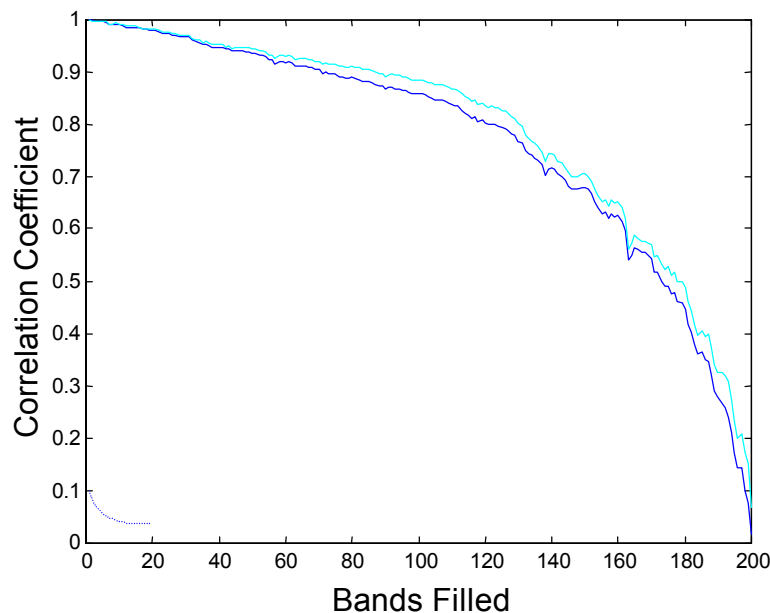
Figure 3-4 Correlation versus spectrum bands filled by high intensity components.

3.1.2 Spatial Filtering Model

The digital simulation was expanded to demonstrate the feasibility of AOA signal processing. A second orthogonal dimension to the Fourier transform plane was added to the original digital simulation. The results showed that with AOA separation and rejection, broadband interference could be eliminated. The key to a successful model was constructing a time signal having the proper AOA information. The AOA phase delay in each channel is $\phi = \dfrac{2\pi}{\lambda_{RF}} d \sin\theta$, where d is the antenna spacing, and θ is the AOA. For a given antenna spacing, d, and signal source direction, θ, a unique phase delay is determined for each frequency component of the time signal, $2\pi/\lambda_{RF\_n}$, where
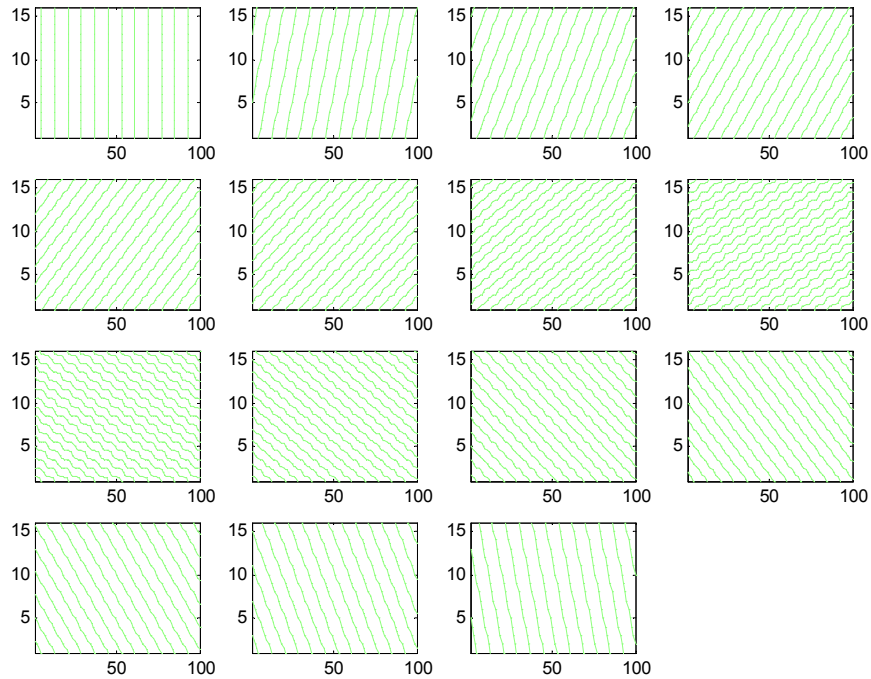
Figure 3-5 N-1 discrete resolvable angles of arrival used in digital simulation

n = 1:128. Constructing a time domain signal with the proper AOA phase information required that the signal be constructed in the frequency domain by adding the appropriate phase delay to each of the 128 frequency components in the signal bandwidth, then using an inverse Fourier transform to get the time signal. Figure 3-5 shows each of the 15 resolvable AOA possible for a 16-channel array (seven different angles, two different quadrants) for a single-frequency time signal, $2\pi/\lambda_{RF}$, (1 out of a possible 128). The 2-D DFT array size was [256X16].
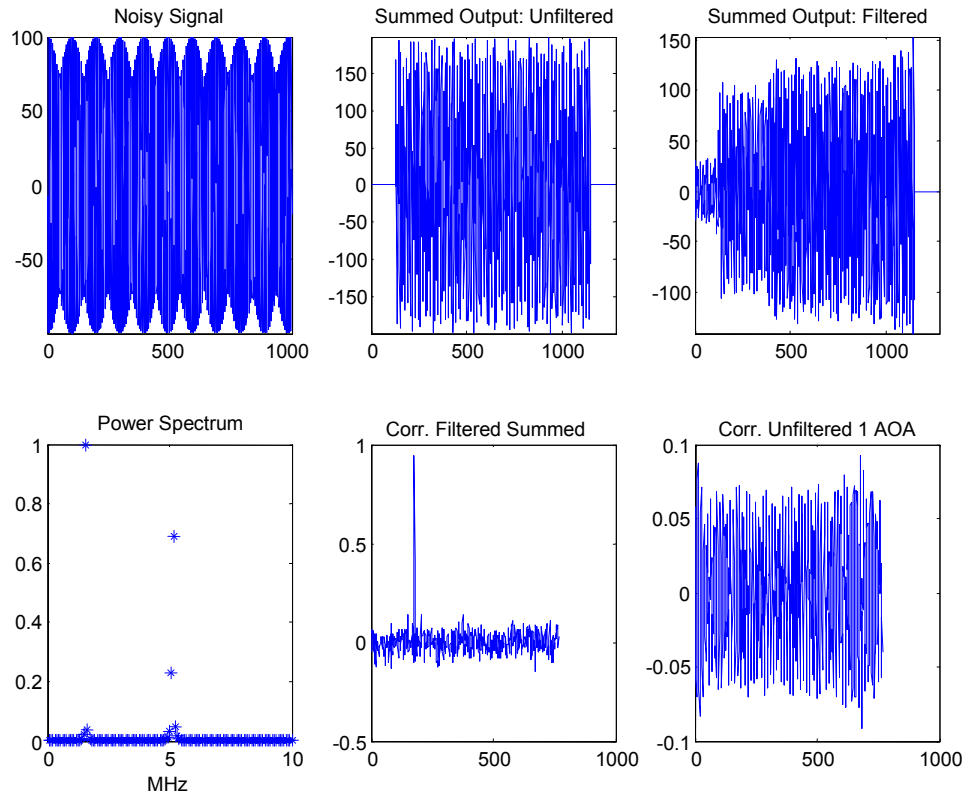
Figure 3-6 Digital simulation results for spatial filter: Noisy signal, power spectrum, filtered & unfiltered output, filtered & unfiltered correlation.

Figure 3-6 shows the results of the 2-D simulation. The AOA filtering successfully removed broadband noise. The noisy signal and its power spectrum are shown on the left hand side. Note that the power spectrum shows two peaks, but there is width associated with each peak, an indication that unresolvable sinusoids were used for the interference components, a condition that prevented recovery of the signal using just the frequency filtering described earlier (an easy way to construct a noisy signal). The filtered and unfiltered reconstructed signals are plotted, as well as the results of correlation between the original PN code and the filtered reconstructed signal, and correlation between the original PN code and the unfiltered reconstructed signal.

3.2 Acousto-Optic RF Signal Excision

The advantage of optical signal processing lies in the parallel nature of light that allows processing of many hundreds, if not thousands, of complex operations simultaneously. For example, the signal time sample, Fourier transform, excision of unwanted frequency components, and inverse Fourier transform all occur virtually simultaneously in real time using a Bragg cell, lens, optical spatial filter, and heterodyne detector. The drawback of an optical system, to date, has been the inefficiency of converting electrical signals to the optical domain, modulation of the optical signals by other optical or electrical signals according to (1) real time input, (2) electronic feedback, or (3) stored memory, and then converting the optical result back to the electrical domain for further electronic processing, storage, or display. In spite of these difficulties, it is the potential of parallel optical signal processing that still generates interest for research and development of novel improvements.

This section describes the components for an analog optical version of the frequency domain signal excision system discussed in the previous section. The A-O modulator used to obtain a power spectrum of the RF signal is described in Section 3.2.1. The frequency plane notch filter system response is discussed in Section 3.2.2.

3.2.1 Acousto-Optic Modulation

The optical output of an Acousto-Optic (A-O) modulator is a power spectrum of an input RF signal. This signal transform operation, which is difficult to achieve in other ways, allows the exploitation of many types of frequency-domain optical signal processing. After the first demonstration of A-O diffraction in 1932, it took the development of the laser in the 1960's to revive interest in acousto-optics as a means of spatially modulating coherent light by electrical signals in order to take advantage of optical signal processing techniques. A-O modulators continue to be an important optical device, in spite of its potential for nonlinear diffraction at high-modulation intensity that limits the spurious-free dynamic range. Also when considering spread spectrum pseudo-random noise signals, the drive power requirements are relatively high. Advantages are extremely large bandwidth capability of hundreds of megahertz, high throughput, and low cross talk between channels. Acousto-optics has a rich history of academic and technological development, and there are a number of excellent texts and articles that one can refer to in order to supplement the brief introduction contained in this chapter.[12, 13, 14]

3.2.1.1 Single-Channel Acousto-Optic Modulator

An A-O device consists of a transparent crystal optimized for photoelastic and A-O quality. See Table 3-1 for a listing of some popular A-O material characteristics. In

addition to the crystal, a piezoelectric transducer is cut to vibrate in a longitudinal (compressional) mode and bonded to the crystal so that application of an RF signal will mechanically vibrate and launch into the crystal an acoustic pressure wave that propagates through its length. The result is an ultrasonic delay line that has a sample time given by the length of the crystal divided by the acoustic speed $\Delta t = L/v_a$ (signal duration within the illumination aperture).

There are two modes of A-O modulator operation: thin phase diffraction (Raman-Nath), which results in multiple diffractive orders, and thick phase diffraction (Bragg), which results in a high-efficiency single diffraction order. The Bragg cell is typically used for RF spectral analysis and laser beam deflection.. Figure 3-7 is a descriptive illustration of an A-O modulator operating in the Bragg mode. Plane wave illumination, $E(t,\mathbf{r}) = \mathrm{Re}\{A\exp[j(\omega_l t - \mathbf{k} \cdot \mathbf{r})]$, and the sound field propagating in the crystal, $s(t) = \mathrm{Re}\{A\exp[j(\omega_a t - \mathbf{K} \cdot \mathbf{r})]\}$, are shown as rays having wave vector $|\mathbf{k}| = \omega_l/c = 2\pi/\lambda$ and $|\mathbf{K}| = \omega_a/v_a = 2\pi/\Lambda$, respectively. The two fields can only interact for a particular value of the incident angle, θ_B, known as the Bragg angle, which is given by the relation

$$\sin \theta_B = \frac{\mathbf{k}}{2\mathbf{K}} = \frac{c\omega_a}{2nv_a\omega_l} \qquad\qquad (\,3\text{-}3\,)$$

where n is the crystal index of refraction, v_a is acoustic velocity, and c is the free space velocity of light. A very simple description of the A-O interaction between light and sound is given by the particle model for Bragg diffraction, which is a statement of the conservation of energy.[15] The light wave consists of photons having particle momentum, $m = h\mathbf{k}/2\pi$, and the sound wave phonons having particle momentum, $m = h\mathbf{K}/2\pi$, where h

is Plank's constant. Conservation of momentum in a collision requires that either a phonon is annihilated, as in $\mathbf{k}' = \mathbf{k} + \mathbf{K}$, where light momentum is shifted toward the direction of sound travel, as shown in Figure 3-7, or a phonon is created, as in $\mathbf{k}' = \mathbf{k} - \mathbf{K}$, where light momentum is shifted in the opposite direction of sound travel. Similarly, conservation of energy, $(E = h\nu)$, in a collision requires that either a phonon is annihilated, as in $\omega_l' = \omega_l + \omega_a$, and the light frequency is upshifted by an amount equal to the frequency of the applied RF signal, or a phonon is created, as in $\omega_l' = \omega_l - \omega_a$, where the light frequency is downshifted. The A-O frequency shift can also be described by a Doppler effect.

Three principal diffracted beams are shown in Figure 3-7, which represent the lower, upper, and center frequencies of the Bragg-cell bandwidth . It should be noted that a wide diffraction bandwidth is desired for use in signal processing, but the simplified Bragg theory presented here predicts only one optimum diffraction angle; however, the
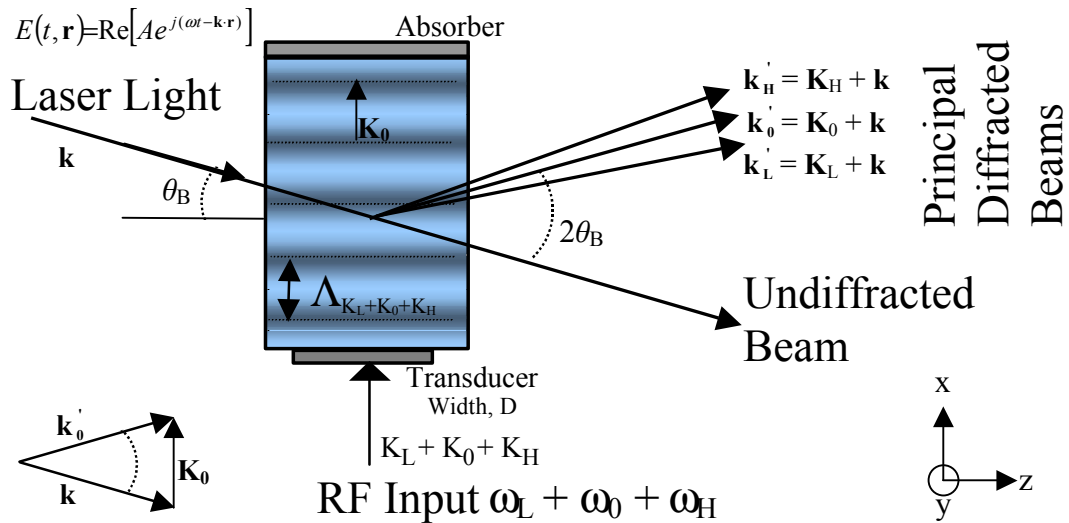
Figure 3-7 Acousto-optic Bragg deflection. Wave vectors conserve momentum.

41

finite width of the transducer and sound wave diffraction in the crystal provides an RF

bandwidth for a given Bragg angle in isotropic crystals. In practice, large bandwidths are

achieved by crystal anisotropy, which allows conservation of momentum to be satisfied

over a larger range of acoustic frequencies than for isotropic crystals. Thus, anisotropic,

A-O materials, such as TeO_2, have advantages for high RF bandwidth; slow acoustic

speeds give better signal resolution; and high refractive index gives larger efficiency.

First-order modeling of the phase function within the crystal ignores sound wave

diffraction, so the acoustic beam has constant width in the x-direction and no variation in

the y-direction. Any index variation in the y-direction is assumed to occur only between

separate Bragg cell channels, as shown in Figure 2-7. A voltage signal, s(t) =

Re{Aexp[j($\omega_a t$)]}, applied to the transducer causes linear oscillation according to the

input signal's frequency and magnitude, creating an acoustic wave that propagates along

the length of the cell. The acoustic wave compression and rarefaction modulate the

crystal refractive index due to the photoelastic effect and create a dynamic phase grating

that can be expressed in terms of an amplitude transmittance function

$$t_a = \exp\left[j\frac{2\pi n_1 D}{\lambda} \hat{s}\left(t - \frac{x}{\upsilon_a} \right) \right] rect\left(\frac{x}{2W} \right) rect\left(\frac{y}{2W} \right) \qquad (3\text{-}4)$$

where $\hat{s}(t)$ represents the input electrical signal, s(t), scaled to the proper acoustic field

units, and $\dfrac{2\pi n_1 D}{\lambda}$ is a phase modulation factor involving constants n_1 = maximum index

perturbation, υ_a = acoustic velocity, λ = optical wavelength in free space, and D =

transducer width in the z-direction. The two rectangular functions define the finite

aperture. It should be pointed out that Equation (3-4) indicates that the refractive index change is proportional to the sound amplitude given by $\hat{s}(t)$.

Figure 3-8 shows the distribution of optical intensity at the focal plane of a lens for optic illumination of a thin phase grating function, such as t_a in Equation (3-4), located at the object plane. The plots were obtained using the beam propagation software program GLAD.[16] In Figure 3-8(a) the phase function, t_a, where $\hat{s}(t,x) = \cos[\omega_a(\text{t-x}/\upsilon_a)]$, is illuminated by a plane wave that produces peaks having a sinc function width determined by the array size that defines the illumination function. Note that the multiple orders, characteristic of Raman-Nath diffraction, are generated because t_a is a phase function, whereas an amplitude grating would generate only a zero and ± 1 orders. The lower plot is the same phase transmittance function, t_a, illuminated by a truncated Gaussian beam. This illustrates the use of a Gaussian apodization function to reduce sidelobes in the Fourier transform plane.

Accurate determination of the relative intensity of the various scattered orders for thin A-O phase gratings is given by the well-known Raman-Nath solution

$$\frac{I_n}{I_{inc}} = [J_n(v)]^2 \qquad (3\text{-}5)$$

where J_n is the nth order Bessel function of the first kind, and v is the sound-induced peak phase shift (Raman-Nath parameter) given as

$$v = k\,D\,\Delta n = k\,D\,|C'|\,|S| \qquad (3\text{-}6)$$

where k is the light propagation constant, D is the crystal width, C' is the real materials constant such that $\hat{s}(t) = C's(t)$, and S is the amplitude of the sound field.[14] In addition,
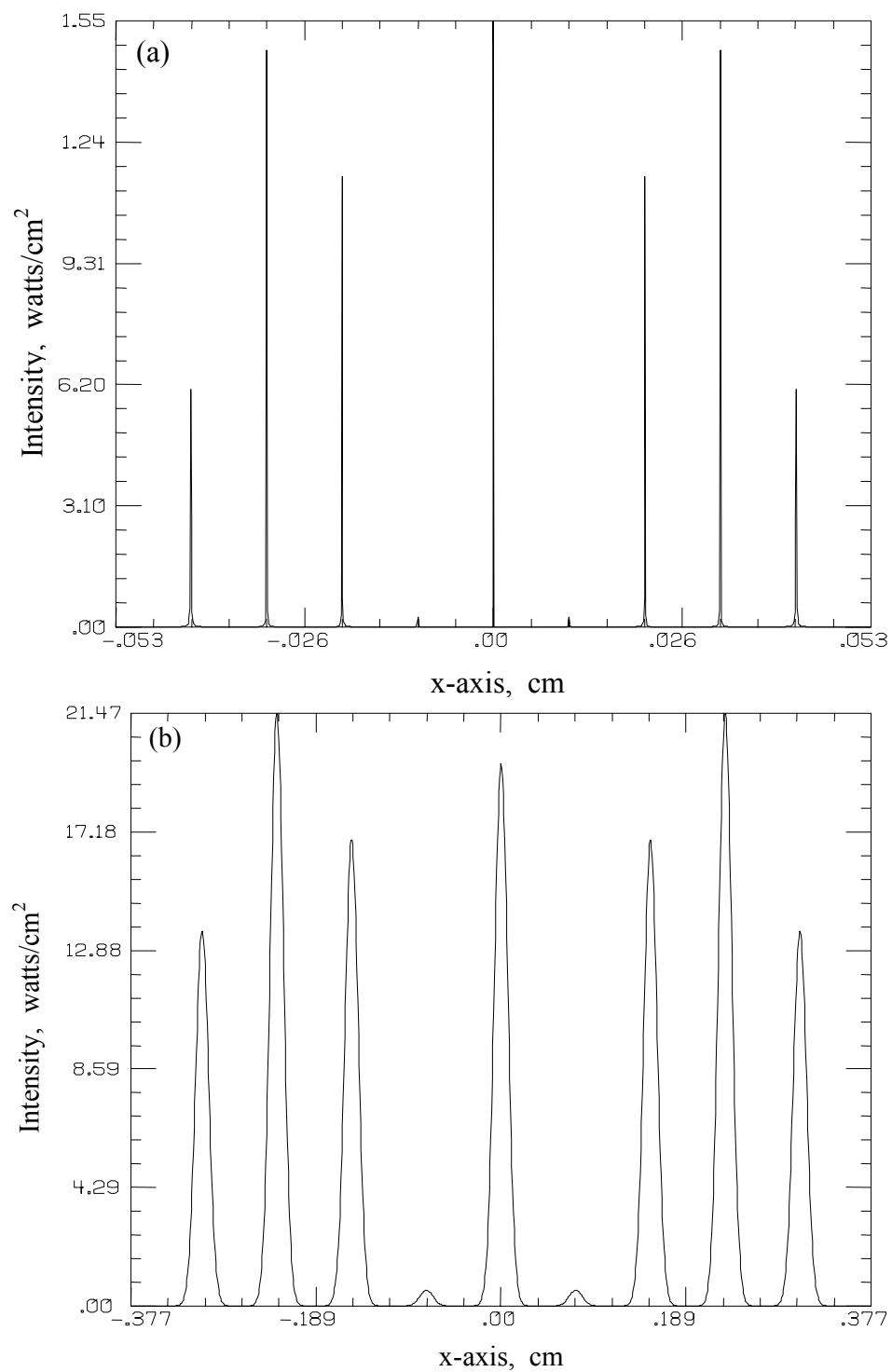
Figure 3-8 Fraunhofer diffraction for sinusoidal phase transmittance function; (a) plane wave illumination, (b) Gaussian beam illumination.

the intensity distribution of light at the focal plane of a lens (Fraunhofer region) for an illuminated sinusoidal phase grating is well known and is given by[5]

$$I(x,y) = \left(\frac{A}{\lambda f}\right)^2 \sum_{n=-\infty}^{+\infty} J_n^2\left(\frac{v}{2}\right) \text{sinc}^2\left[\frac{2w_x}{\lambda f}(x - nf_a\lambda f)\right] \text{sinc}^2\left(\frac{2w_y y}{\lambda f}\right) \qquad (3-7)$$

where f_a is the frequency of the phase grating, w_x and w_y are the aperture widths, and $z = f$ is the position of the analysis plane at the lens focal length.

Generally a single diffraction order with high diffraction efficiency is desired, and this is achieved by using volume phase gratings. Volume effects suppress the higher orders seen in Figure 3-8 and increase the efficiency of the remaining diffractive order, usually either $\pm 1^{st}$. The Klein-Cook parameter

$$Q = \frac{2\pi}{n}\frac{\lambda D}{\Lambda^2} \qquad (3-8)$$

is a measure of the relative amplitude of the diffractive orders and is directly proportional to the transducer width, D.[17] A value $Q < 1$ indicates the A-O modulator is operating in the Raman-Nath regime, and a value $Q > 7$ indicates the A-O interaction is operating in the higher efficiency Bragg regime.

A reasonable measure of first-order diffraction efficiency for the case of low modulation index is obtained by an efficiency parameter

$$\eta = \frac{I_d}{I_{inc}} = \sin^2\left[\frac{\pi^2}{2\lambda^2}\left(\frac{n_0^6 p^2}{\rho v_a^2}\right)\frac{D}{H}P_a\right]^{1/2} \qquad (3-9)$$

where p is the photoelastic coefficient, ρ is the mass density, v_a is the acoustic velocity, D is the width of the transducer, H is the height of the transducer, P_a is the acoustic power,

and $\frac{n_0^6 p^2}{\rho v^3}$ is the A-O figure of merit.[18] The efficiency parameter defined by Equation (

3-9) can be used to show that the amplitude of the diffracted light, $[I_d]^{1/2}$, is linearly

proportional to the input voltage, $V_s = [P_a]^{1/2}$, applied to the transducer. Exact calculations

for diffracted light amplitude in thick phase gratings with high index modulation require

use of the coupled-mode theory for optic diffraction.

The coupled-mode theory is used to obtain exact diffraction efficiencies for

various types of volume gratings with respect to the particular illumination angle and

wavelength.[14, 19, 20] When applied to the analysis of A-O phase gratings, a Doppler shift

must be added to the results in order to account for the frequency shift of the light due to

sound interaction. For the condition of illumination at the Bragg angle of incidence and

thick gratings, the coupled-wave theory assumes that only two waves need to be

accounted for in the grating: the incident wave entering at the Bragg angle and the wave

diffracted at twice the Bragg angle, as these two waves are not severely attenuated by

violation of the Bragg condition. Their interaction in the grating is described by the

scalar wave equation, and the analysis defines a coupling constant and coupled wave

equations that give the interaction between the incident and diffracted waves. The result

is that a transfer of energy between the two waves causes a periodic rise and fall of

energy between them according to the interaction length of the thick grating.

The transfer of energy between the incident and diffracted wave is shown in

Figure 3-9. The plot was obtained using GLAD beam propagation software to model

illumination of the same phase grating, t_a, used in Figure 3-8, but the illumination was

incident at the calculated Bragg angle, and to simulate the volume grating optical

46
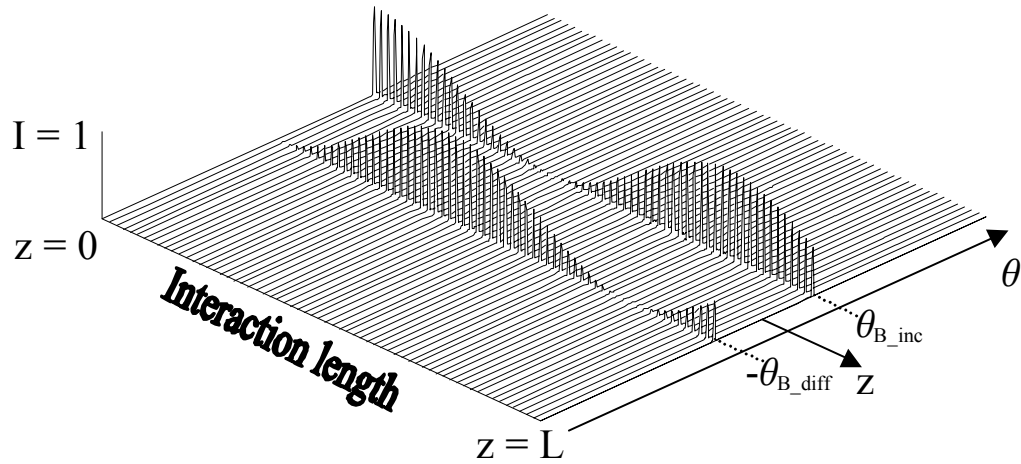
Figure 3-9 Simulated energy transfer between zero- and first-order diffraction in angular space.

transmission was calculated over a number of individual small steps in order to propagate

through the total length, $(z = 0$ to $z = L)$, of the Bragg cell.[21, 22] The light intensity across

the aperture was plotted for each propagation step. As the incident beam, I_{B_inc},

propagates through the phase grating, energy is coupled into the Bragg diffraction beam,

I_{B_diff}. The Bragg angle was 3.2°, the wavelength was 850 nanometers, and the maximum

refractive index variation was 0.0011. Note that the angular separation is twice the Bragg

angle.

Figure 3-10(a) illustrates light intensity distribution for Bragg diffraction. The

Gaussian beam illumination and aperture function are the same as in Figure 3-8(b). In

practice, slight alignment of incident light into the Bragg cell will optimize the Bragg

angle for diffraction into either the negative or positive order, and the figure simply

combines both orders. Figure 3-10(b) was obtained applying the Matlab discrete Fourier
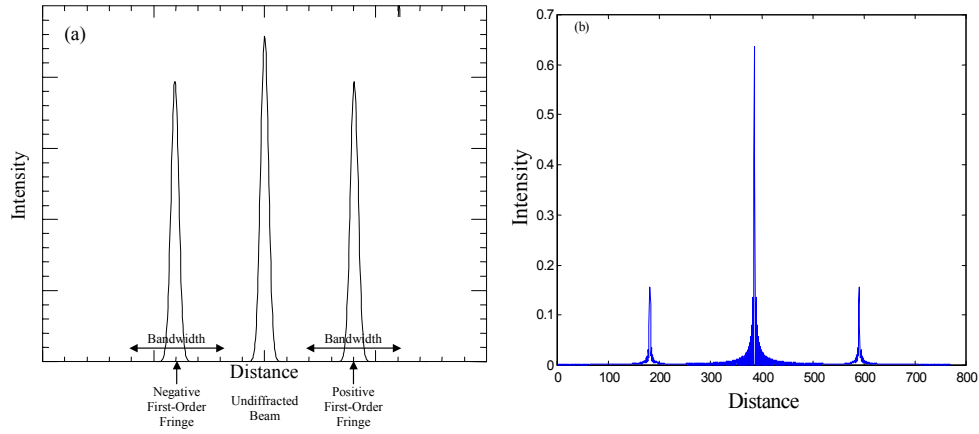
Figure 3-10 Bragg diffraction: (a) Light intensity for thick grating beam propagation model, Gaussian beam illumination. (b) Discrete Fourier transform of phase grating.

transform to the phase grating used in the GLAD® plots. It shows that the Bragg

diffraction in part (a) is a Fourier transform of the grating. The difference in amplitude is

due to mismatches in modulation index, and the width is consistent with Figure 3-8(a), a

function of the sampled array space.

Solving the coupled wave equations gives exact diffraction efficiency for thick

phase transmission gratings for any incident angle, but when the Bragg condition is

achieved, maximum diffraction amplitude is attained and the results of the coupled wave

equations are simplified. In this case, the diffraction efficiency is

$$\eta_{Bragg} = \sin^2 \frac{\pi\, n_1 L}{\lambda\, \cos(\theta_{Bragg})} \qquad\qquad (\,3\text{-}10\,)$$

where L is the interaction distance within the grating, and n_1 is the index modulation.

The maximum diffraction efficiency is reached when $\Phi=\pi/2$, and the interaction distance

becomes

48

$$L = \frac{\lambda \cos \theta_{Bragg}}{2\,n_1}.$$

(3-11)

Bragg cells should be operated in the small-signal regime in order to avoid inter-modulation products associated with high-intensity optic diffraction, so generally the small signal approximations given in Equation (3-9) apply.

Table 3-1 Acousto-optic material characteristics

Material	Optical Range microns	Refractive Index	Acoustic Velocity Km/sec	Figure of Merit $\times 10^{-15}$ m^2/W	Bandwidth (3dB) MHz
Lithium Niobate fast slow	0.6 – 4.5	2.2	6.6 3.6	7 15	1000 - 15000
Tellurium Dioxide fast slow	0.4-0.6	2.25	5.5 0.62	1000 34	40 - 200
Indium Phosphide	1.0 – 1.6	3.3	5.1	80	50 - 300
Germanium	2.0 – 12.0	4.0	5.5	180	30
Gallium Phosphide	0.59 – 10.0	3.3	6.3	44	100-1000

3.2.1.2 Multi-Channel Bragg Cells

The temporal excision filter was shown to be effective against all types of interference except wideband barrage noise.[23, 24, 25] In this case the filtered signal is degraded, because all frequencies which make up the signal can be affected either by overwhelming due to interference or excess spectral excision. Wideband barrage noise is the obvious choice for hostile jamming, but it requires more power, whereas narrowband RF interference has a more common occurrence as the inadvertent product of a cluttered

RF environment. Effective spatial filtering as shown in Figure 1-4 uses phased-array antennas to sample the spatial domain and filter according the location of the source. Because a combination of temporal and spatial filtering is desired, the additional processing capacity of multi-channel Bragg cells is being considered. Multi-channel A-O devices have been used for processing phased array signals, and investigating this approach as a potential means of countering the broadband RF interference became a goal of this research.

A linear antenna array is illustrated in the upper-left portion of Figure 3-11. The signal that reaches the receiving antenna is located a distance from the receiver so that it has the form of a traveling plane wave arriving from angle θ_{AOA}. The phase delay between each element of the antenna array is given as

$$\phi = \frac{2\pi}{\lambda_c} d_r \sin\theta_{AOA} \qquad\qquad (\text{ 3-12 })$$

which contains a term for the location angle of the source, θ_{AOA}.[26] Electronic processing of the phase information contained in the ensemble of N signals received at each element of the array requires phase delay to optimize the signal gain. However, the AOA is unknown, so all angles of interest must be processed individually.

Processing the ensemble using a multi-channel, Bragg cell and Fourier transform lens creates simultaneously a frequency spectrum and off-axis, azimuthal displacement that is proportional to the direction of arrival for each signal source received. This represents a tremendous computational advantage over electronic processing. However, this approach does not allow active positioning of the antenna's gain peak within the
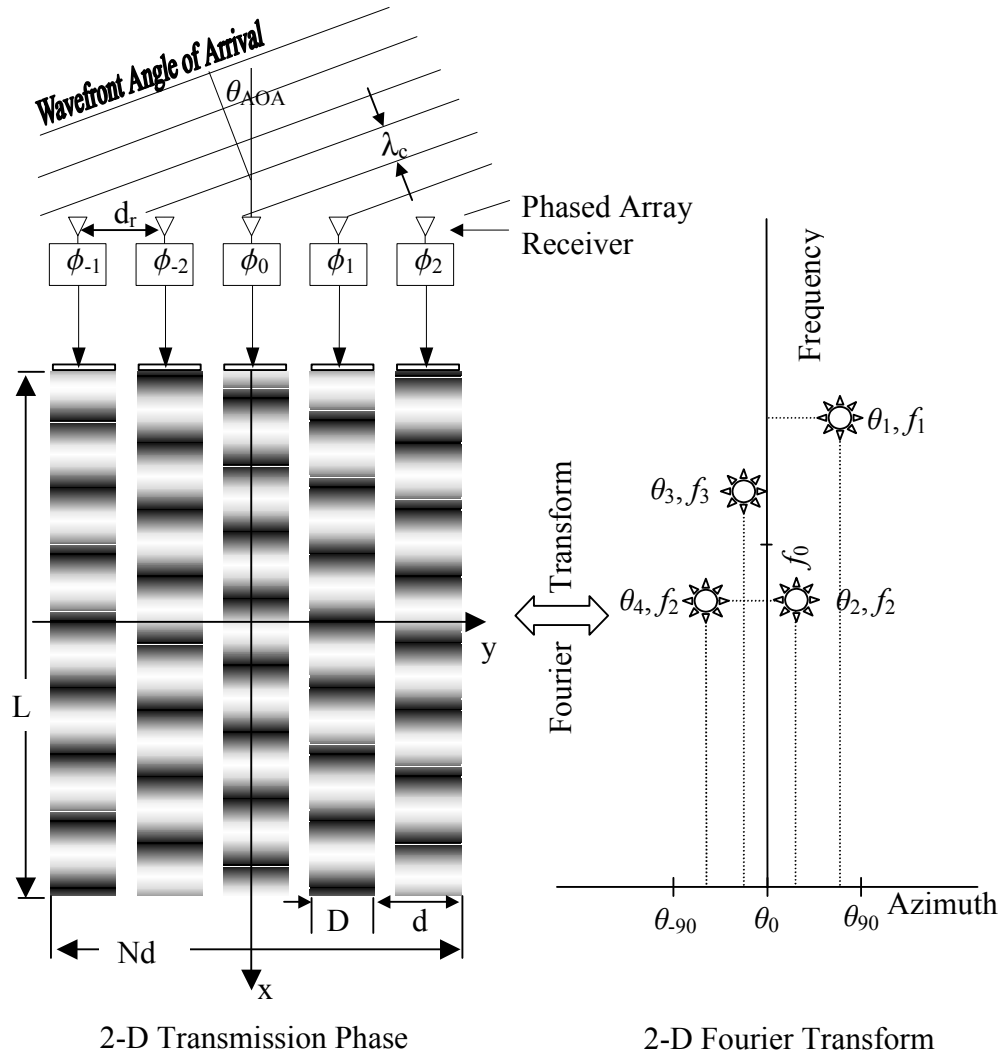
Figure 3-11 Multi-channel Bragg cell phase grating and beam forming at the Fourier transform plane.

antenna field of view, which is obtained at the cost of electronic processing and actively delaying phase.

The complex phase transmission function of the multi-channel array, which was described earlier in Section 2.6, is also illustrated in Figure 3-11. The spatial frequency due to the RF spectrum, f_x, is represented vertically, x-axis, and the spatial frequency due

to the phase difference between channels, f_y, is represented horizontally, y-axis.

Recalling Equation (3-4), the amplitude transmittance function for the single-channel

Bragg cell, a similar multiple-channel expression is

$$t_a = \sum_{n=-(N-1)/2}^{n=+(N-1)/2} \exp\left[j\frac{2\pi n_1 D}{\lambda} \hat{s}\left(t - \frac{x}{v_a} - n\phi \right) \right] \mathrm{rect}\left(\frac{x}{2L}\right) \mathrm{rect}\left(\frac{y-nd}{2d}\right). \qquad (\text{ 3-13 })$$

To obtain this expression the AOA phase term for each channel, ϕ, was included in the

term for the traveling sound field; that is, $\hat{s}(t,x,\phi)$. For each channel, the aperture

function for the width, d, and position, (y_{-nd}), is accounted for by the second rectangular

function.

The two-dimensional Fourier transform of the amplitude transmittance function

gives the optical amplitude distribution at the focal plane of a lens, and is given by[27]

$$E(f_x, f_y) = \left[\frac{\sin \pi N(f_y + \phi)}{\sin \pi(f_y + \phi)} \right] \left[\mathrm{sinc}\, L\left(f_x - \frac{1}{\Lambda_c} \right) \right] \left[\mathrm{sinc}\, f_y\, D \right]. \qquad (\text{ 3-14 })$$

The $\dfrac{\sin \pi N(f_y + \phi)}{\sin \pi(f_y + \phi)}$ function is displaced off axis by the phase difference between each

channel, and is multiplied by the wider of the two sinc functions that is due to the Bragg

cell width, D. The narrower sinc function due to the Bragg cell aperture length, L, is

shifted by the carrier frequency phase function, $1/\Lambda_c$. Experimental results for AOA

phase shifting are shown in Figure 5-11.

3.2.2 Heterodyne Detection

This brief review of heterodyne detection follows the excellent descriptions contained in

references [29 & 38]. Photodetectors are insensitive to optical phase and therefore cannot

detect the optical frequency modulation of the A-O diffracted beam. In order to recover

the RF signal, the beam is mixed with a phase-coherent optical field, and the resulting

phase interference (called beating) creates amplitude variations that a photodetector can

detect. This detection technique is called optical heterodyne or coherent optical

detection. Figure 3-12 diagrams a heterodyne detection setup that uses a beam splitter to

mix the two beams. Misalignment between angle of incidence on the detector or

mismatched polarization between the two waves reduces or washes out the interference

(or cross-product) term. For this reason polarized fiber-optic couplers provide excellent

heterodyne detection results, because the interaction between reference and signal beams

occurs in a coupled-fiber waveguide. A disadvantage of fiber coupling is the difficulty of

matching the path lengths of the signal and reference beams when using lasers with short

coherence lengths. The stringent requirements for heterodyne detection are well known.

See for example reference [29].

In the RF excision system, the axial position of the photodetector is of no

consequence, and heterodyne detection can be done anywhere after the signal and

reference beams have been combined.[31,29] That is, the optically modulated RF signal can
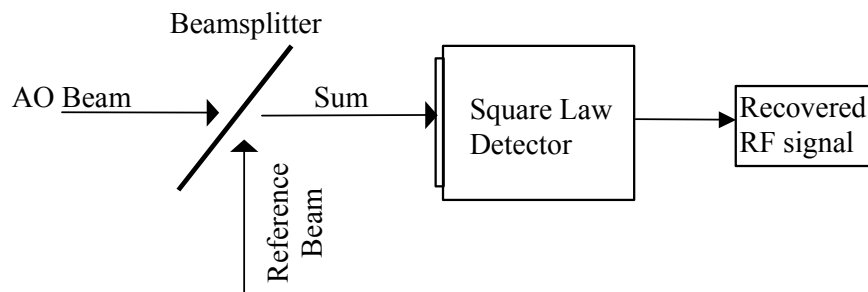
Figure 3-12 Diagram of heterodyne detection setup using beam splitter.

be detected just behind the filter by summing all spectral components at the Bragg cell

frequency plane or by using point detection at a Bragg cell image plane.

An equation for the heterodyne-detected signal is obtained by taking the absolute

square sum of the complex amplitudes of each beam.[38] The result is given as

$$\left|A_S e^{j(\omega_S t)}+A_R e^{j(\omega_R t)}\right|^2=\left|A_S\right|^2+\left|A_R\right|^2+2\left|A_S\right|\left|A_R\right|\cos[(\omega_S-\omega_R)t+(\phi_S-\phi_R)]\qquad (\text{ 3-15 })$$

Note that optical light intensity components $|A_S|^2 + |A_R|^2$ contribute to the photocurrent,

but not the cross-product term. These DC terms can be filtered. The cross-product term

varies as the cosine of the difference between the two optical frequencies, which in this

case is the frequency applied to the Bragg cell. It contains the desired magnitude,

frequency, and phase information, $g(t) = |A_S|^2 |A_R|^2 \cos(\omega_{RF}t + \phi)$. The intensity of the

reference beam becomes an amplification term. It can be made large in order to provide

gain, and heterodyne detection is a common means of amplifying weak signals as well as

reducing the carrier frequency.

To show that the detected signal, g(t), is directly proportional to the signal that

drives the Bragg cell, the following expression gives the form for the heterodyne-detected

output of an RF spectrum analyzer:

$$g(t)=a(x_0)s(t-\tau_0)\cos[2\pi f_{RF}(t-\Delta t/2)]\qquad (\text{ 3-16 })$$

where $f(t) = s(t)\cos(2\pi f_{RF}t)$ is the signal applied to the Bragg cell, $s(t)$ is the baseband

signal, $\cos(2\pi f_{RF}t)$ is the RF carrier, the time delays are proportional to the Bragg cell

transit time (time aperture), Δt, and $\tau_0 = \Delta t + x_0/v_a$ is a time delay dependent on the

position of the equivalent reference-beam probe position, x_0, at the Bragg cell (see red

dashed line on Figure 1-3, reprinted below as Figure 3-13). Finally, an amplitude

54

weighting function, evaluated at x_0, includes the illumination function, attenuation factors, optical intensity, and Bragg cell truncation.

3.2.3 Acousto-Optic RF Signal Excision

The acousto-optic RF signal excision system given in Figure 1-3 is reprinted below as Figure 3-13. This optical processing technique has been studied extensively over the last 20 years.[28, 29, 30] RF signal excision expands upon the heterodyne RF spectrum-analyzer architecture by excising undesirable interference at the frequency plane. The RF spectrum analyzer is a well-known means of analyzing the spectrum of an RF signal and has a 100% probability of intercept. The architecture is identical to Figure 3-13, except that an array of detectors is positioned at the Fourier transform plane. Heterodyne detection at each detector in the array functions as a channelized receiver. The total signal is recovered by summing the output, and signal excision is achieved by a special photodetector array that will switch each detector element to one of two summing buses. High intensity interference is switched to one bus, low intensity signal to another, and in this way, both signals are available for further processing. Another approach uses spatial light modulators to block light at the Fourier transform plane. Spatial light modulators have on-off contrast ratios on the order of 30 dB. Both approaches require electronic feedback in order to determine the frequency location of the RF interference and programming to switch appropriate channels.[31, 32, 33] To streamline the process, adaptive spatial light modulators are desired that automatically attenuate optical intensity above a predetermined threshold. Photorefractive optical power limiting devices appear suitable for this purpose.[35,34]

3.2.3.1 Notch-Filter Function

A notch filter can remove the narrowband RF interference depicted in the spectrum of the 20 MHz wideband, spread-spectrum communication channel represented in the lower portion of Figure 3-13. In this figure, the RF spectrum is now shown by the optical intensity function, $I(f_x)$ at the Fourier transform plane, rather than the temporal frequency function applied to the Bragg cell, as was depicted in Figure 1-3. Removal of the high intensity component is accomplished by a spatial-filter function, $H(f_x)$, that provides an opaque notch at the position of the high-intensity beam. As was shown in Section 2.4, and Section 3.2, the signal spectrum is represented in the Fourier transform plane by an aperture weighting function, $A(f_x)$, convolved with a Kronecker delta
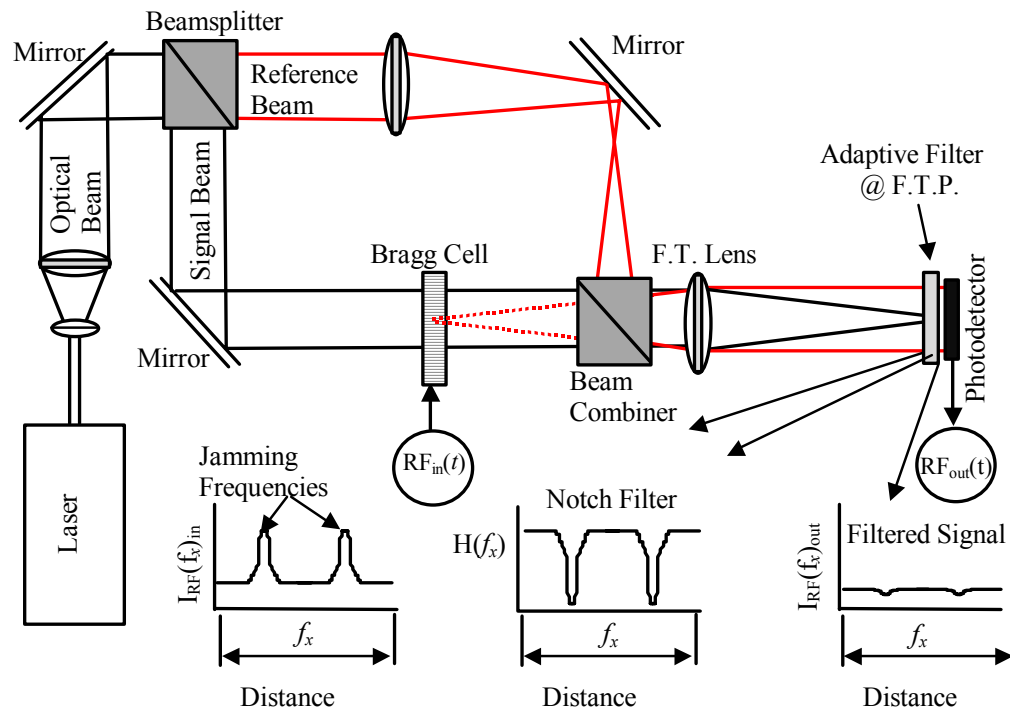
Figure 3-13 Acousto-optic RF signal excision system. Lower plots show spatial frequency in region of Fourier transform plane.

function that shifts the position of the aperture function, A(f_x), proportional to the signal power spectrum. Recall that A(f_x) is a convolution of the Bragg cell aperture and the illumination amplitude distribution, and that in order to maximize the frequency resolution the aperture should be as large as possible, and a Gaussian apodization function is used in order to maximize the excision notch depth. The system response is obtained by sweeping A(f_x) over the entire passband of the system and plotting the magnitude of the output signal, g(t), as a function of input frequency. The cross-product term of the heterodyne detector is

$$g(t)=2\,\mathrm{Re}\left\{\int_{-\infty}^{\infty}I_+(f_x,t)\,R_+^*(f_x,t)\,|H(f_x)|^2\,P(f_x)\,df_x\right\} \qquad (\,3\text{-}17\,)$$

where P(f_x) is the photodetector response, $R_+^*(f_x,t)$ is the reference signal, I$_+$(f_x,t) is the signal (interferer) response and H(f_x), is the filter transmittance function, squared, because it is applied to both the signal and reference functions. Note that the phase response of the notch-filter function is eliminated because both the reference and signal pass through it, and, in fact, this occurs everywhere the two beams share identical paths, showing the importance of using a collinear architecture.

The reference beam is a phase signal given by

$$R_+(f_x,t)=e^{j2\pi f_x x_0}, \qquad (\,3\text{-}18\,)$$

and the signal (interferer) response is given by

$$I_+(f_x,t)=e^{j2\pi f_j\left(t-\frac{\Delta t}{2}\right)}A(f_x-f_{x\_j}). \qquad (\,3\text{-}19\,)$$

Substituting these expressions into Equation (3-17) gives

$$g(t) = 2\,\mathrm{Re}\left\{ e^{j2\pi f_j\left(t-\frac{\Delta t}{2}\right)} \int_{-\infty}^{\infty} A(f_x - f_{x\_j}) e^{-j2\pi f_x x_0} \left|H(f_x)\right|^2 P(f_x)\, df_x \right\}. \qquad (\,3\text{-}20\,)$$

It is seen that the output signal has the same frequency content as the input, and its amplitude is the convolution of the notch filter function and the Fourier transform of the weighting function, with its associated exponential multiplier that indicates the position of the reference-beam probe. Convolution is a smoothing operation that adds the width of each function.

3.2.3.2 Collinear-Beam Design

The Mach-Zehnder implementation is modified by collinear architectures to reduce microphonic-induced phase noise. Erickson [32] proposed the holographic architecture illustrated in Figure 3-14. A holographic optical element (HOE) redirects part of the undiffracted beam to function as a reference beam. However, this approach causes the reference-beam power to fluctuate with the signal power, so generally the undiffracted beam should not be used as a reference beam. A better approach uses collinear propagating beams that are separated from the single laser beam prior to the Bragg cell. Various methods have been proposed to achieve a collinear interferometer,
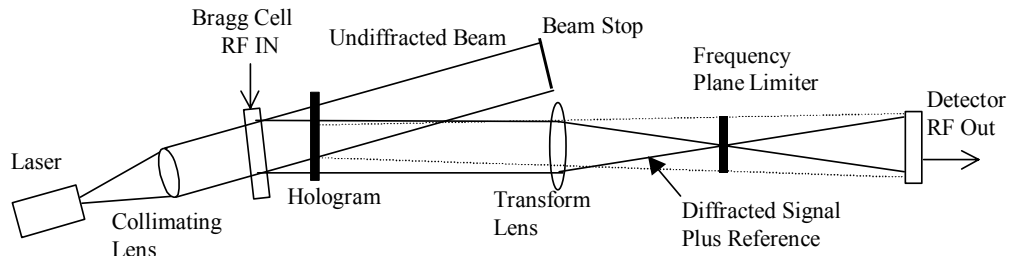
Figure 3-14 Collinear architecture for acousto-optic RF signal excision.

and a simple approach became apparent for the multi-channel Bragg cell. However, the idea was not tested or modeled and is discussed in Chapter 6 as a recommendation for further study.

Chapter 4

Electro-Optic Power Limiter

The promise of optical computing can be realized by the successful development of processes for optical control of optical signals. In early 1980 Erickson noted in his work with the acousto-optic RF excision system that adaptive excision of narrowband RF interference in broadband communication systems could be achieved by using an optical power limiter that passed low-intensity light but attenuated high-intensity light.[32] Research to develop optical and electro-optical control of light modulation was very intense at that time, and the hope of efficient optical control techniques was high. Spatial Light Modulators (SLMs) such as the Hughes liquid crystal light valve, the Texas Instruments deformable mirrors, the AT&T SEED device, were early successes. SLMs were applied to RF signal excision to block light in the Fourier transform plane,[33] but there was the burdensome requirement for feedback systems to provide apriori control to the SLM to block light where excision was needed. Hong *et al* demonstrated adaptive RF excision systems that could reject narrowband interference in wideband communication signals.[35,36] These approaches used acousto-optic correlation and two-wave mixing in a photorefractive crystal to couple time-correlated, narrowband interference energy away from the RF detector leaving behind the wideband signal. This photorefractive approach

to optical modulation was sensitive to relatively low-intensity light and was an important step in achieving a fully adaptive system; however, a drawback was that only a few, at best, narrowband RF signals could be efficiently decoupled at one time. Hong later proposed using adaptive optical power limiting based on a similar, but potentially more robust, photoconductive field-shielding approach reported by Steier in 1988.[8] Interest in this approach generated the support needed for this dissertation.

4.1 Electro-Optic Amplitude Modulation

The optical power limiting approach reported by Steier involves self-modulation of Electro-Optic (EO) birefringence by photorefractive field shielding. At the outset of this dissertation, this approach appeared very promising for adaptive signal excision. Power limiting required no external feedback circuitry, and has a low-threshold intensity and a wide field of view (cubic crystals have no birefringence). There were, however, questions regarding its suitability as a frequency domain notch filter. Investigating these questions of filter resolution and filter depth became an objective of this dissertation. Miniaturization is always an overriding objective, which puts constraints on the filter-resolution capability.

Photorefractive-charge confinement has adequate spatial resolution for holographic data storage; however, it was not known if this resolution could be maintained for very high-intensity optical and electric fields. There is also the question of what photorefractive materials are best suited for this application. The optical threshold and saturation intensity of the photorefractive material must be optimized to meet the dynamic range requirements of the Bragg cell system, which should include the

signal beam as well as the reference power. This is because the benefits of having a collinear reference beam were two-fold: phase noise is held to a minimum, and power limiting reduces both beams simultaneously, which doubles the attenuation using coherent detection.

This chapter outlines the theoretical models needed to explore the potential performance of the field shielding optical power limiting technique for application as an adaptive filter in an acousto-optic RF signal excision system. Optical power limiting and self switching in high-resistive photoconductive materials is the result of a combination of two physical processes, EO birefringence and photorefractive charge migration and trapping. These two crystal processes are discussed and modeled in this chapter, while the experimental investigations are presents in Chapter 5, Experimental Results.

4.1.1 Electro-Optical Birefringence and the Index Ellipsoid

The index ellipsoid is used to describe the normal modes of propagation of optical waves in crystals, as governed by solutions to the wave equation. The application of electric fields in EO crystals changes the dimensions and orientation of the index ellipsoid, which provides a means of controlling the phase or intensity of light propagating through the crystal. This EO effect results from the redistribution of charges due to the applied field.

The linear EO coefficients for cubic crystals such as Bismuth Silicon Oxide [$Bi_{12}SiO_{20}$] (BSO) and semiconductor GaAs in contracted notation are

62

$$
r_{ij} =
\begin{bmatrix}
0 & 0 & 0 \\
0 & 0 & 0 \\
0 & 0 & 0 \\
r_{41} & 0 & 0 \\
0 & r_{41} & 0 \\
0 & 0 & r_{41}
\end{bmatrix}
\qquad (4\text{-}1)
$$

The equation for the index ellipsoid with applied electric field is written using contracted indices as

$$
\left(\frac{1}{n_x^2} + r_{1k}E_k\right)x^2 + \left(\frac{1}{n_y^2} + r_{2k}E_k\right)y^2 + \left(\frac{1}{n_z^2} + r_{3k}E_k\right)z^2
$$
$$
+ 2yzr_{4k}E_k + 2zxr_{5k}E_k + 2xyr_6E_k = 1 \qquad (4\text{-}2)
$$

where E_k (k= 1,2,3) is a component of the applied electric field $E_1=E_x$, $E_2=E_y$, and $E_3=E_z$, x, y, z are the principal dielectric axes, and n_x, n_y, n_z are the principal refractive indices. Substitution of the EO coefficients in Equation (4-1) with the equation for the index ellipsoid in Equation (4-2) gives the following expression for the index ellipsoid for cubic crystals:

$$
\frac{x^2 + y^2 + z^2}{n^2} + 2r_{41}(yzE_x + zxE_y + xyE_z) = 1. \qquad (4\text{-}3)
$$

Note that this cubic crystal solution has no optical birefringence when the applied electric field is zero. As an example, let an electric field E_z be applied, so that Equation (4-3) becomes

$$
\frac{x^2 + y^2 + z^2}{n^2} + 2r_{41}(xyE_z) = 1. \qquad (4\text{-}4)
$$
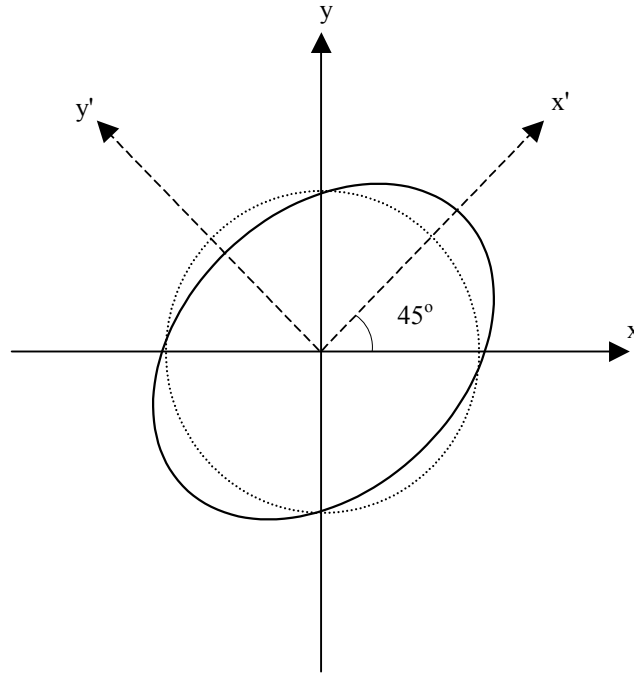
Figure 4-1 Index ellipsoid for zinc-blende cubic crystals with applied field, from [37].

The z-axis retains its principle index; however, the x-y cross term has deformed the index

ellipsoid from a circle to an ellipse. This is illustrated in Figure 4-1.

4.1.2 Electro-Optic Amplitude Modulation

The electric control of optical amplitude by modulating electro-optical birefringence is

well known,[37] and the basic form of the EOPL is the EO amplitude modulator. Yariv

[37] provides EO modulator properties for three possible orientations of zinc-blende

structure crystals such as BSO. Slight consideration is made for the optically active BSO

crystal used in this study. Optical activity is discussed in the next section. A transverse

EO amplitude modulator is illustrated in Figure 4-2. The zinc-blende cubic crystal is
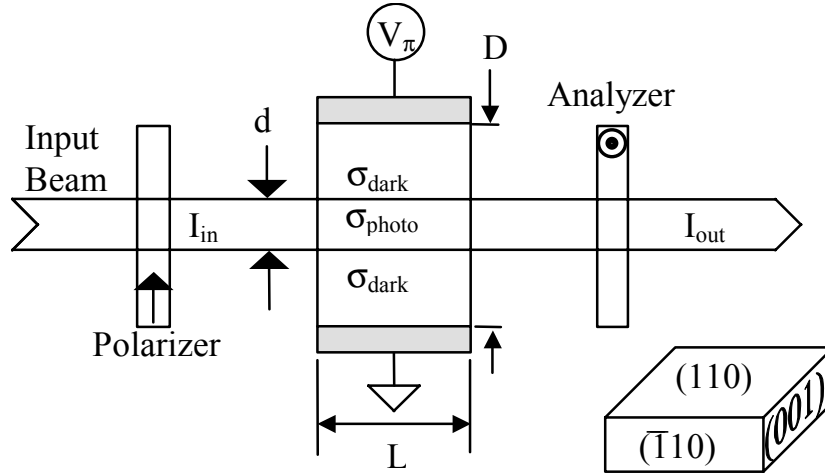
Figure 4-2 Diagram of optical power limiting device and optimum crystal orientation.

cut along the three surface planes, (110), ($\bar{1}$10) and (001), and oriented so that the electric field is applied perpendicular to the (110) plane, and beam propagation is perpendicular to the ($\bar{1}$10) plane. This is the orientation needed to maximize the EO phase retardation in cubic crystals.

The strength of refractive index modulation for a given applied field is a function of the electro-optic figure of merit, $n^3 r_{41}$. For this crystal orientation, linearly polarized light traveling along the z-axis will have an index of refraction change Δn for applied field $E(x)$ given by

$$\Delta n = -\frac{1}{2} n^3 r_{41} E(x).$$

(4-5)

A normal polarization mode for this crystal traveling along the z-axis with interaction length L and externally applied voltage V induces a phase change given by

$$\Gamma = \frac{2\pi}{\lambda} n^3 r_{41} \frac{L}{d} V.$$

(4-6)

65

Note that the strength of refractive index modulation for a given applied field is a function of two parameters, the electro-optic figure of merit, $n^3 r_{41}$, which is a crystal parameter; and the aspect ratio, L/d, which is a design parameter of crystal size.

Amplitude modulation is achieved by polarization conversion and attenuation at an analyzer (polarizer oriented 90° with respect to the input polarization). At z = 0, linearly polarized light is launched into the crystal at 45° with respect to the new principle axes, so that each polarization mode has equal magnitude when entering the crystal. The modes propagate with different refractive indices so that the composite polarization begins to acquire a new orientation as shown in Figure 4-3.

$\Delta\delta = 0$	$\Delta\delta = \pi/4$	$\Delta\delta = \pi/2$	$\Delta\delta = 3\pi/4$	$\Delta\delta = \pi$
Linear	Elliptical	Circular	Elliptical	Linear
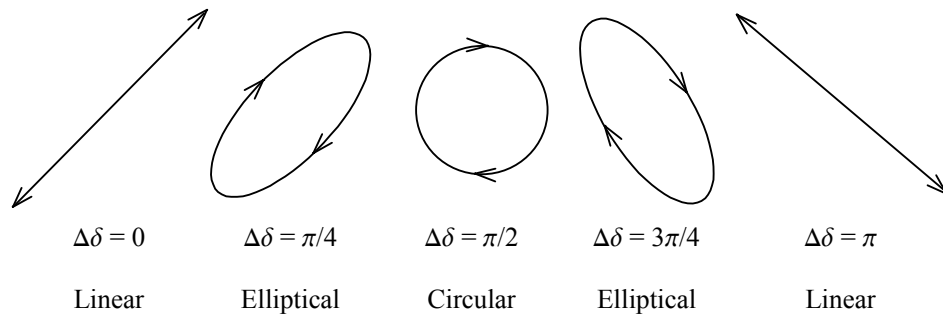
Figure 4-3 Polarization ellipses at various phase angles $\Delta\delta = 0$ - $\Delta\delta=\pi$.

The voltage required to get a full 90° polarization rotation for the composite beam as it transverses the length of the crystal is the half-wave voltage V=V$_\pi$. By equating Γ to $\pi/2$ (total phase difference between both beams is π radians) in Equation (4-6), the following expression for the half-wave voltage is obtained:

$$V_\pi = \frac{\lambda}{2} \frac{D}{L} \frac{1}{n_0^3 \, r_{41}}.$$

(4-7)

At the output plane, an analyzer will block light according to the amount of voltage applied to the crystal, and V_π is the maximum voltage needed to achieve the maximum transmission. The transmission through an amplitude modulator is given by

$$T = \sin^2 \frac{\Gamma}{2} = \sin^2 \frac{\pi}{2} \frac{V}{V_\pi}.$$ (4-8)

An expression for EOPL transmission takes into account the extinction ratio of the optical system (polarizers and crystal), as this ultimately determines the maximum notch depth.[42] An expression for the output intensity at the analyzer as a function of the input intensity of the optical amplitude modulator that includes the extinction ratio of the polarizers is

$$I_{out}(x) = I_{in}(x) \left[\sin\left(\frac{\pi}{2} \frac{E(x)}{E_\pi}\right)^2 + \xi_p \right]$$ (4-9)

where ξ_p represents the polarization extinction ratio for the crystal and polarizer pair. By using a polarized beam splitter, the applied voltage acts as a variable switch.

4.1.3 Geometrical Considerations

The half-wave voltage, V_π, is minimized by having a high EO coefficient and low aspect ratio. Recall that L is the interaction length needed to accomplish the 90° polarization rotation required for amplitude modulation. As seen in Equation (4-6), for a given material there is some flexibility with choosing d, L, and V_π, but there are trade-offs. The interaction length is usually increased to minimize the V_π voltage, which can be quite high and cause difficulty in avoiding dielectric breakdown in air. Increasing the length requires a longer depth of focus for the beams that make up the input signals. For our
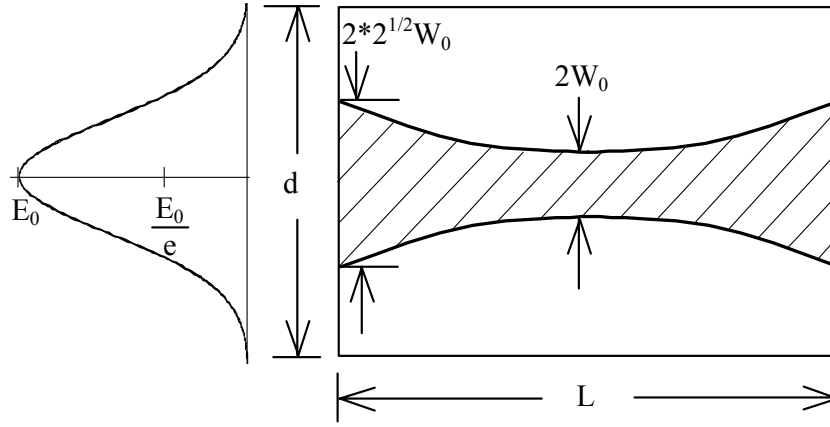
Figure 4-4 Depth of focus, Gaussian beam divergence for E-O interaction length L and transverse dimension d, from [37].

application the modulator is located at the focal plane of a lens, so the selection of spot size and focal length of the Fourier transform lens are not arbitrary. The depth of focus constraint is illustrated in Figure 4-4. Assuming the input signals applied to the power limiter approximate Gaussian beams, the best focus that can be achieved at the focal plane is $2W_0$, and this spot size diverges gradually in both directions outside the focal plane. The depth of focus is the distance the beam maintains its minimum value to within a factor of $\sqrt{2}$. This amount is twice the Rayleigh range, $z_0 = \sqrt{2}\ W_0$. Using this definition, the depth of focus is

$$2z_0 = \frac{2\pi W_0^2}{\lambda} \qquad\qquad (\,4\text{-}10\,)$$

which shows that a small spot size and long depth of focus cannot be obtained simultaneously. Equation (4-10) is used to solve for the minimum spot size

$$W_0 = \sqrt{\frac{\lambda_0 L}{2\pi n}} \qquad\qquad (\,4\text{-}11\,)$$

68

where n is the index of refraction in the crystal. Note that a large refractive index increases the depth of focus significantly.

The BSO crystal is optically active. This means that right- and left-hand circular polarizations are the normal modes of propagation, rather than linear polarizations. In this case Equation (4-3) does not apply, and the model must be modified to include optical rotation. Solving the wave equation to obtain the index ellipsoid when electric fields are applied to optically active crystals is not a trivial problem and was not done. The nature of the problem will be made clear in the next section, which gives an introduction to optical activity. Assumptions made in the next section with regard to the propagation modes for electrically biased optically active crystals are supported by the experimental results reported in Chapter 5.

4.1.4 Optical Activity

BSO is an optically active crystal, meaning that it is a natural polarization rotator. The specific rotary power of BSO at wavelength 623.8 nm wavelength, defined as the amount of rotation per unit length, is $\rho = 21°/\text{mm}$. The direction of rotation can be either right or left handed, depending on the seed used for crystal growth. The crystal used in our experiments was right handed (counterclockwise). The approximately 6 mm-length crystal, used in the experiments had a measured rotary power of 131°, so a safe assumption without using a micrometer is that a more precise measure of the crystal length is 6.24 mm.

Optical activity is found in medium with molecules having an inherently helical structure. An optically active dielectric medium is characterized by the following medium equation:[37, 38, 39]

$$\mathbf{D} = \boldsymbol{\varepsilon}\mathbf{E} + \varepsilon_0 \xi \nabla \times \mathbf{E}. \qquad (4\text{-}12)$$

Note that this result indicates a spatially dispersive material, because $\mathbf{D}(\mathbf{r})$ is dependent on points in the immediate vicinity of $\mathbf{r}$ due to the derivatives of $\nabla \times \mathbf{E}(\mathbf{r})$. It can be shown that for plane wave illumination, the normal eigenmodes of propagation in the crystal are circularly polarized rather than linearly polarized. A derivation of the right- and left-hand circular polarization modes in optically active crystals is given in the texts by Yariv [37], Saleh [38], and Yeh [39]. Circular polarization propagates through an optically active material unchanged; however, each right- and left-hand component travels at different phase velocities, and this difference creates the optical rotation for linearly polarized light. This is explained in the next paragraph.

Any arbitrary plane wave polarization can be represented as a superposition of two orthogonal polarization states. In addition to horizontal and vertical, linearly polarized light, left- and-right hand circular polarizations compose an orthogonal pair. Thus, linear polarization can be represented as a superposition of the normal modes of optically active medium. When linear polarization is launched into an optically active crystal it is decomposition into right- and left-11davidsb16hand circular polarization and each component propagates through the crystal with separate refractive indices and phase velocities. At the output, superposition of the two circular polarization components,

70

which have acquired a phase difference between them, results in a linear polarization that is rotated by an amount given by the specific rotary power of the crystal

$$\rho = \frac{\pi(n_- - n_+)}{\lambda_0}$$ (4-13)

where n- and n+ are the refractive indices for the left- and right-hand polarization modes. Values for BSO at $\lambda = .6328\ \mu$m are $\rho = 21$ deg/mm and $(n_- - n_+) = 7.383 \times 10^{-5}$.

The rotation of linear polarization can be avoided by using a quarter wave plate to convert linear polarization into a single circular polarization mode and launching circularly polarized light into the optically active crystal to eliminate birefringence. After propagation through the crystal, a second quarter wave plate is used to convert the circular polarization back to the original linearly polarized state.

When an electric field is applied to the crystal, EO birefringence alters the refractive indices, and the circularly polarized light obtains linearly polarized component as it propagates through the crystal (see Figure 4-3), during which the phase is altered due to optical activity. A result of optical activity in an EO amplitude modulator is an increase in the half-wave voltage from that predicted by Equation (4-7). For linearly polarized light, the applied voltage must be increased an additional amount in order to compensate for the total amount of polarization rotation due to optical activity. For circularly polarized light the applied voltage must be increased an additional amount in order to compensate for half the total amount of polarization rotation due to optical activity; that is, the EO effect converts the circular polarization to linear polarization over half the length of the crystal. Self-adaptive amplitude modulation can be achieved using

photorefractive charge generation, transport, and trapping that alters the EO

birefringence. The photorefractive process is the topic of the next section.

4.2 Photorefraction

Photorefraction is a term used to define a change of refractive index in EO materials that

results from localized optically induced, space-charge electric fields. The space-charge

fields develop from a redistribution of electrons and holes due to photoionization,

conduction, and charge trapping in the optical crystal.[38,40] The refractive index change

can be quite long lived due to long lifetimes of the trapped charge and was originally

thought to be optical damage. Historically, interest in the photorefractive effect has

involved wave mixing through multiple-beam interference and the self-generation of

periodic volume diffraction gratings as well as storage of volume and planar holograms.

The photorefractive effect is efficient at beam coupling because there is a quarter-

wavelength phase shift between the peak light intensity and peak refractive-index change

that creates perfectly phase-matched Bragg scatterings. Important applications of the

photorefractive effects include energy coupling for amplification of small-signal beams,

holographic recording and reconstruction for storing data, and real-time light modulation

for optical computing.

Photorefractive optical power limiting has been achieved using two variations of

the photorefractive processes. One method uses two-wave mixing to couple energy away

from a strong beam and into the propagation mode of another probe beam. This

technique was used by Hong *et al,* [35,41] to achieve adaptive RF signal excision. This

approach is limited in the number of simultaneous beams that can be efficiently power

72

limited, and only around 10 dB of attenuation was achieved. Recently, optical power limiting due to efficient back-reflection beam coupling from periodic index gratings formed by standing optical waves in photorefractive fiber has been demonstrated. These optical-fiber power limiters have applications to channelized approaches, where a linear or two-dimensional array of fibers is dedicated to each resolvable spot in a Fourier transform array or image. This approach is proposed for reducing the focal length and depth of focus of the Fourier transform lens.

The second method of photorefractive power limiting, and the one chosen for this research, is called Electro-Optic Power Limiting (EOPL). It utilizes photoionized charge to self-modulate the externally applied half-wave voltage that produces EO polarization conversion discussed in the previous section. This self-modulation results in efficient power switching at the polarized beam splitter. Both of these approaches, dynamic beam coupling and EO self-modulation, are also being examined as methods for protecting detectors/sensors from high-intensity laser illumination (laser hardened detectors). The EO approach appears more robust than the beam-coupling approach for multiple signals. Attenuation over 40 dB has been achieved. Much of the theory developed for photorefractive beam coupling can be applied to the analysis of the EO approach because of the common physical processes involved.

The objective of this section is to develop the theory needed to calculate an optical-transfer function for the EOPL. Two models will be examined. A simple analytical solution provided by Chang *et al*,[42] that is based on changes in photoconductivity within an idealized rectangular-illumination region is discussed in section 4.2.2.

73

This model describes the EOPL transfer function and can be used on a point-by-point basis to approximate the spatial profile of a large, nonuniform beam. However, the model does not take into account photorefractive charge transport. The simple model is improved by taking into account the photorefractive charge transport model, which is discussed in section 4.3, and numerically calculating the space-charge field, $E_{sc}(x)$, induced by nonuniform optic illumination, $I(x)$. $E_{sc}(x)$ is used in Equation (4-8) in order to calculate the spatial distribution of the EO modulator transmission function, $\Gamma(x)$. The simple model compares quite well with the numerical results because a very simple relationship between dark intensity and optical power limiting applies. For this reason, the simple model will be used to introduce the operation of the EOPL, and then the band-transport model of Kukhtarev et al [50] and a numerical solution of $E_{sc}(x)$ will be discussed.

4.2.1 Photorefraction and Electro-Optic Power Limiting

The EOPL is an EO amplitude modulator that operates by taking advantage of photorefractive properties in doped crystals to self-modulate EO birefringence. [2, 42] The technique was first demonstrated as a means to visualize electrical domains in GaAs:Cr, responsible for bulk differential negative resistance,[43] and was later demonstrated as an optical power-limiting device.[2] Figure 4-5 illustrates the photorefractive field-shielding process. A typical transverse EO modulator is shown using a crystal having photorefractive properties. In order to explain the photorefractive effect, two cases are illustrated. In the upper figure low optical illumination intensity is applied to the crystal, and in the lower figure high optical illumination is shown. Both beams are linearly
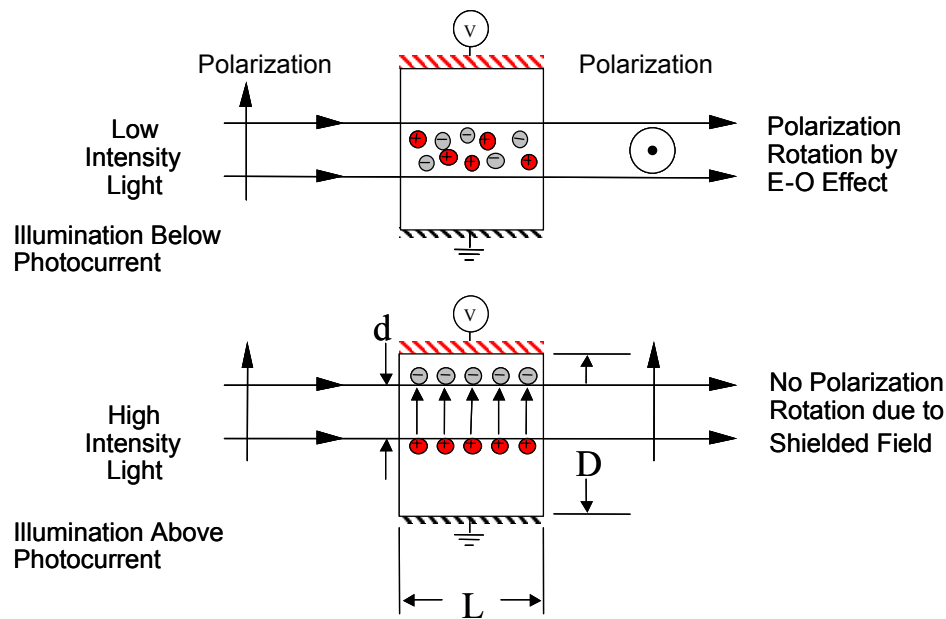
Figure 4-5 Photorefractive field-shielding in EO modulator.

polarized. The low-intensity beam has optical intensity below the dark intensity for

photoconductivity, and the basic photorefractive properties of photoionization, charge

transport, and trapping are overwhelmed by the random effects of temperature. The

externally applied electric field is distributed uniformly across the crystal, and the EO

birefringence rotates the polarization of the light propagating the length of the crystal by

90°. This is normal operation for a conventional transverse EO amplitude modulator and

when the field is at the half-wave value, ideally all light passes through the analyzer.

The lower half of Figure 4-5 shows the case when the optical intensity exceeds

the dark-intensity threshold. Photoionized charge will drift away from immobile ionized

donors and recombine to accumulate at the dark edges of the nonuniform illumination.

Charge separation creates a space-charge field oriented to oppose the applied field,

thereby decreasing the electric field strength within the illuminated area. Ideally with

adequate photoionization, this self-modulation can completely cancel out the applied field, so high-intensity light propagating through the crystal experiences no EO birefringence and will be attenuated at the analyzer (or reflected at a polarized beam splitter).

The dark conductivity is a parameter that establishes the lower threshold limit for optical power limiting. Shallow traps give rise to thermally ionized charges, resulting in a uniform, dark illumination (or dark conductivity) across the crystal that the applied optical intensity must reach before photoionization overcomes competition from thermal noise. Light representing a signal that is intended to pass unaffected through the power limiter must have a lower intensity than the dark intensity. The power-limiting threshold must be appropriately designed to meet the signal intensity requirements of the system, which is larger than the optical threshold for bulk BSO. Fortunately, illuminating the crystal with a uniform optical bias can increase the optical threshold intensity.[44] Thus, it is the uniform nature of the dark illumination that establishes the optical-limiting threshold for photorefractive effects to occur.

4.2.2 Equivalent Circuit Model

A simple model for the transmission function of the EOPL is obtained by assuming an equivalent electrical circuit for the illuminated and dark regions of the crystal and the applied half-wave voltage.[42] Figure 4-6 shows the circuit. The model ignores charge transport dynamics and assumes a single, square-profile beam, I_j (jam), with width $= d$, that must be less than the crystal width D, and uniform photoconductivity given by
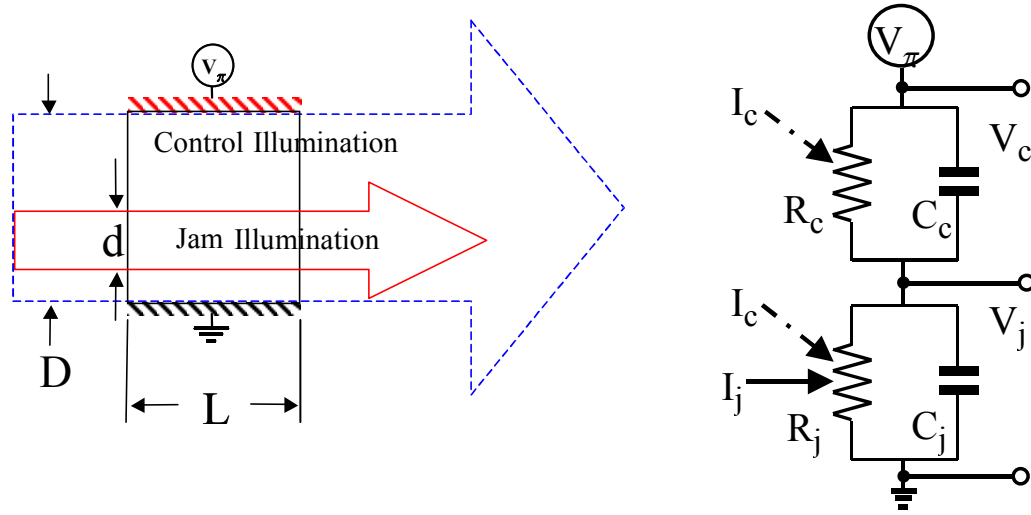
Figure 4-6 Equivalent circuit model for electro-optic power limiter.

$$\sigma_j = \frac{1}{R_j} = B I_j + \frac{1}{R_{dc}}$$ (4-14)

where B is the coefficient of photoconductivity and $1/R_{dc}$ is the control illumination plus

dark illumination conductivity. That is, the control illumination fills the crystal and has

width = D-d and uniform photoconductivity given by

$$\sigma_{dc} = \frac{1}{R_{dc}} = B I_c + \frac{1}{R_{dark}}$$ (4-15)

where $1/R_{dark}$ is the dark conductivity, and I_c the control illumination. For a steady state

analysis, the capacitance is ignored. The applied voltage produces a current, and the

conductivity can be obtained from Ohm's voltage current relation

$$\sigma = \left(\frac{D}{A}\right)\frac{I}{V}$$ (4-16)

where I = current, V = voltage, A = area of the crystal over which the voltage is applied,

and D = distance between electrodes. In the steady-state condition, the current through

the crystal is constant, so by knowing the photo and dark conductivities, the voltage in each region can be solved, and the amount of EO amplitude modulation is determined.

The conductivity is obtained in the following manner: The relationship between conductivity and charge carrier concentration is

$$\sigma = q(\mu_n n + \mu_p p) \qquad\qquad (\text{4-17})$$

where n and p are electron and hole concentrations respectively, and μ_n and μ_p are the charge mobilities. Photoionization of incident photons creates electron-hole pairs, which increases the concentration of electrons in the conduction band above their thermal-equilibrium value. For photorefractive crystals such as BSO, mobile electrons from ionized charges are responsible for conduction, while the positively ionized atoms are not mobile. The linear relationship between photoconductivity and applied optical power is shown in Figure 5-18 for BSO, obtained experimentally. The coefficient of photoconductivity, B, is obtained from the slope of the line by dividing conductivity by the optical power, $\sigma/I = B = 1.94 \times 10^{-8}$ [ohms-watts-cm]$^{-1}$. The optical wavelength used was 632.8 nm. BSO has a very low dark conductivity, $\sigma_{dark} = 10^{-15}/\Omega$-cm, which corresponds to a dark illumination of 5×10^{-8}.

The voltage relationships are obtained by using simple voltage division. The crystal has dimension D in the direction of the applied field, length L in the direction of light propagation, and cross-sectional area A over which the voltage is applied. The voltage drop across the illuminated region can be obtained from the following relations:

$$V_j = V_\pi \frac{R_j}{R_j + R_{dc}}$$

(4-18)

where, $R_{dc} = \dfrac{D-d}{\sigma_{dc} A}$, $R_j = \dfrac{d}{(\sigma_{dc} + \sigma_j) A}$.

Substituting the equations for resistance and simplifying (eliminates A = area) gives an

expression for the voltage in the illuminated region in terms of I_j, which is

$$V_j = \frac{V_\pi}{1 + \left(1 + \dfrac{B I_j}{\sigma_{dc}}\right)\left(\dfrac{D}{d} - 1\right)}.$$

(4-19)

By substituting this voltage into Equation (4-6), one obtains the total phase change, that

the I_j beam experiences in propagating through the electro optic crystal. The result is

$$\Gamma_j = \frac{\dfrac{2\pi}{\lambda} n^3 r_{41} L V_\pi}{D\left(1 + \dfrac{B I_j}{\sigma_{dc}}\right) - \dfrac{d B I_j}{\sigma_{dc}}} = \frac{\pi}{1 + \left(1 - \dfrac{d}{D}\right)\dfrac{B}{\sigma_{dc}} I_j}$$

(4-20)

where Equation (4-7) is substituted into the center expression to simplify the equation.

Equation (4-20) is used in Equation (4-8), to obtain an expression for the output

intensity of the EOPL. The result is

$$I_{out} = I_{in} \left[\sin\left(\frac{\pi}{2} \frac{1}{1 + \left(1 - \dfrac{d}{D}\right)\dfrac{B}{\sigma_{dc}} I_j}\right)^2 + \xi_p \right]$$

(4-21)

where $I_{in} = I_j$. The optical transmission is $T = I_{out}/I_{in}$. Figure 4-7 is a plot of Equation

(4-21) showing power in versus power out. Two values of dark conductivity were

plotted to show how uniform control illumination increases the optical power limiting
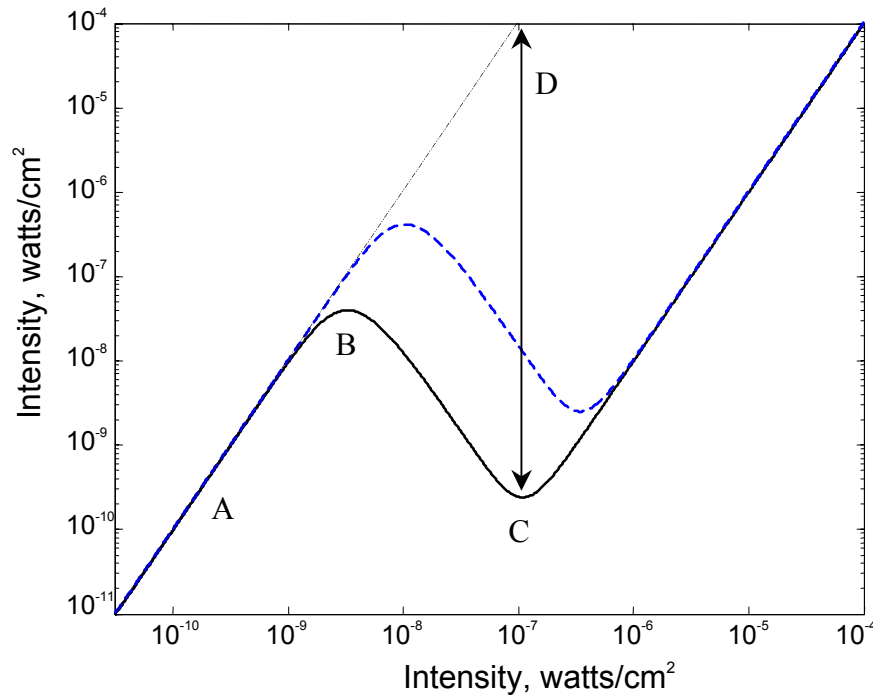
**Figure 4-7 Amplitude transmission plot for EOPL using simple
model. Dashed line shows effect of control-illumination bias.**

threshold. The parameters used for the plot were obtained experimentally for BSO. The

plot with the dashed line was calculated using a control illumination 10 times greater than

the dark illumination. Note that the threshold for the dark conductivity occurs at the dark

intensity, $I_{dark} = 5 \times 10^{-8}$ W/cm^2, and the control light intensity when it is used.

The curve has five regions of interest, labeled in the figure as (A) through (E),

which are described as follows: (A) At low -optical intensities, the ratio I_{out}/I_{in} is unity.

This region encompasses the dynamic range for the desired optical signals and can be

adjusted by uniform illumination. For acousto-optic RF signal excision this is most likely

the intensity of the reference beam used for heterodyne detection. (B) When the

threshold intensity for optical power limiting is reached, that is, any intensity above

uniform illumination of the crystal, the output intensity begins to decrease with
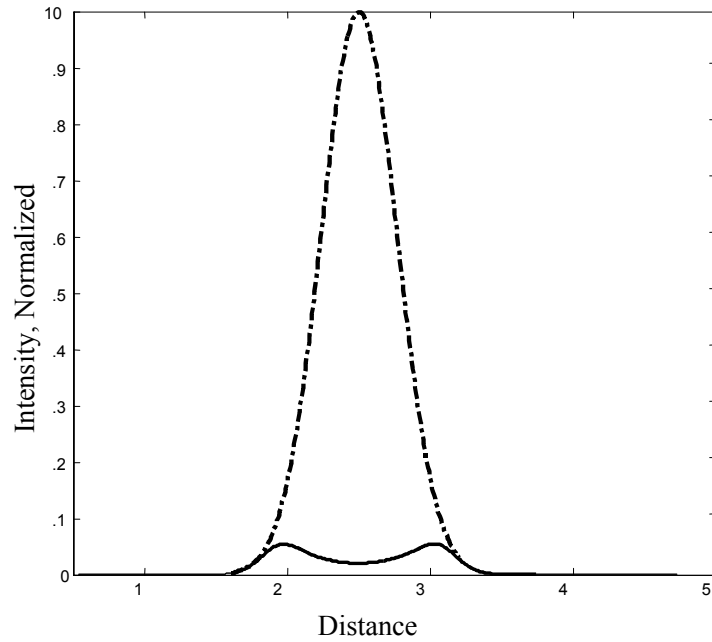
**Figure 4-8 Spatial power limiting plot using simple model for
EOPL applied on a point-by-point basis.**

increasing input intensity due to photorefractive field shielding, and the intensity follows

the sine squared relationship for EO amplitude modulation given in Equation (4-21). (C)

Minimum transmission occurs when the electric field is completely shielded. With

increased intensity the transmission increases due to leakage at the analyzer, the output

again linearly tracks the input, but it is attenuated by the value $\xi_p = 60$ dB, shown by the

line indicated by D.

While Figure 4-7 shows the transmission over a range of input values for a square

beam applied to the EOPL, the transmission as a function of the beam profile $I(x)$ can be

approximated by mapping the results of Equation (4-21) on a point-by-point basis with

the input function $I_{in}(x)$. This is illustrated in Figure 4-8; however, in order to obtain an

81

accurate beam profile, solution of the photorefractive charge transport equations is required. This approach is discussed in the next section.

4.3 The Band Transport Model of Kukhtarev

The previous simple model does not take into account the dynamics of photorefractive charge transport, which is accurately described by the Kukhtarev band transport model. The band transport model is composed of a coupled set of equations for rate, current, and Poisson's equation that account for photoionization, drift and diffusion, and charge trapping in photorefractive materials. However, the set of four coupled differential equations are intrinsically nonlinear, and analytical solutions for the space-charge field $E_{sc}(x)$ with respect to the applied illumination are approximate and do not account for external parameters that apply to the EOPL, such as high-optical intensity, arbitrary beam size and shape, and externally applied high-intensity electric fields. [39,40,45,50] For this reason, numerical solutions are used to obtain accurate values for $E_{sc}(x)$ and resulting transmission function for the EOPL.

4.3.1 Energy Band Dynamics

A generalized energy band diagram shown in Figure 4-9 illustrates the charge transport mechanisms occurring within the photorefractive crysta. This model assumes that the photorefractive effect is due to one charge carrier, the electron, which is the case for BSO and other photorefractive materials.[46,47] The material contains deep-level donor impurities with number density N_D^0 and ionized acceptor impurities with number density $N_A \ll N_D^0$. The acceptor impurities are completely filled with electrons from donors and
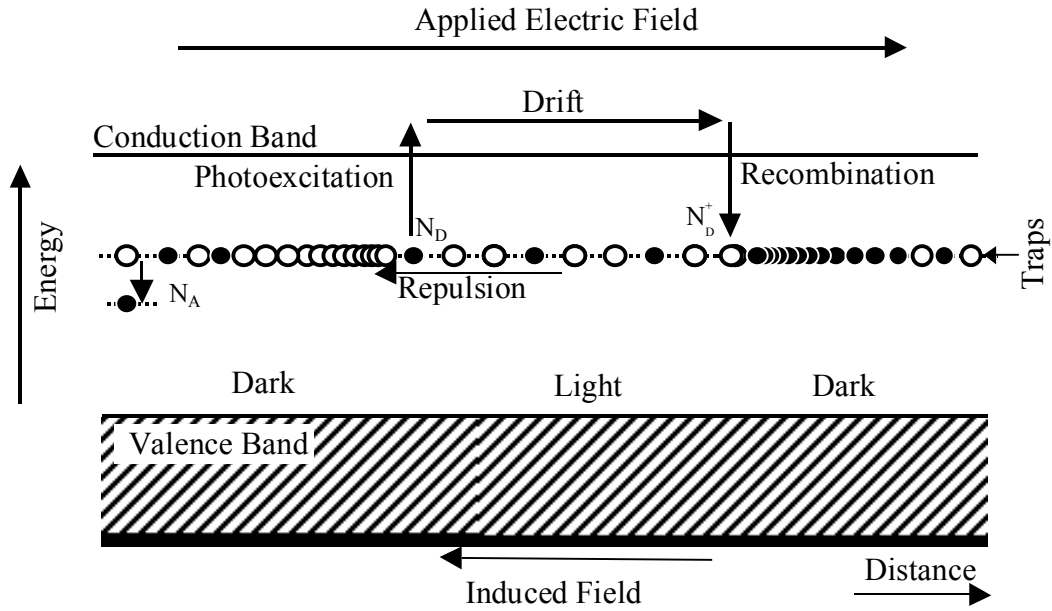
Figure 4-9 Photorefraction energy diagram, charge transport, and trapping.

have photoexcitation energy sufficiently large that these sites cannot be ionized by thermal or optical effects. The density of neutral donor levels that can participate in the photorefractive effect is $N_D = N_D^0 - N_A$. The number of ionized donors that can capture free carriers at temperature $T = 0$ and in the absence of photoionization is $N_D^+ = N_A$; that is, N_A allows positively charged, unoccupied donor sites and bulk-charge neutrality. The positively charged ionized donors are bound to the lattice and do not move with the mobile electrons. The donor energy state is near the middle of the bandgap.

The crystal in Figure 4-9 is shown illuminated with nonuniform light, such as a Gaussian optical beam having intensity $I(x) = I_0 \exp(-(x-x_0)^2/W_0^2)$ and radius $= W_0$ that is small enough so that there exists a light region surrounded by dark regions within the crystal. The requirement for an optical intensity variation in space is essential for the photorefractive effect so that charge carriers have the ability to accumulate in "dark"

regions. Uniform intensity does not provide a region for charge to accumulate. The dark

intensity is defined as β/s, where s is the photoionization cross section, and β is the dark

generation rate. In the light region electrons from deep-level impurities N_D are

photoionized into the conduction band. The density of ionized donors N_D^+ is increased,

which increases the material conductivity as discussed earlier. The energy required for

photoionization is at least the difference between the conduction band energy and the

energy level of the deep traps. Photoionized electrons are generated at a rate G that is

proportional to the optical intensity $I(x)$ and the neutral donor density $(N_D - N_D^+)$, and can

be expressed as

$$G = (s\,I + \beta)(N_D - N_D^+).$$
(4-22)

The rate of trap capture, R, is dependant on the number of electrons $n(x)$, the

recombination coefficient γ_R, and the total number of ionized donors N_D^+ and is given by

$$R = \gamma_R n\, N_D^+$$
(4-23)

By considering the generation and recombination rates for the level populations, the

following single, rate equation is obtained that describes the variations in the populations

of ionized donors and mobile electrons:

$$\frac{dN_D^+}{dt} = (s\,I + \beta)(N_D - N_D^+) - \gamma_R n\, N_D^+.$$
(4-24)

The mobile electrons have an average lifetime, $\tau_0 = (\gamma_R N_A)^{-1}$, and can drift or

diffuse before recombining with ionized donors. The migration of mobile electrons

results in a current density that may affect electron density. The current continuity

equation relates the time rate of change of the charge density to the diffusion of the current density and is given by

$$\frac{dn}{dt} = \frac{dN_D^+}{dt} + \frac{1}{q}(\nabla \cdot j)$$

(4-25)

where q is the electronic charge and $\nabla \cdot j = -\partial\rho/\partial t$ is the current continuity equation. The current density is composed of contributions from the drift and diffusion of electrons. Drift and diffusion of electrons is proportional to the electron mobility and is given by

$$j = qn\mu E + k_B T\mu \frac{dn}{dx}$$

(4-26)

where μ is the mobility, k_B is Boltzmann's constant, and T is temperature. The term on the left is current due to charge drift from the force of the electric field, while the term on the right is the current due to charge diffusion from regions of high- to low-electron concentration, which is noted by the spatial derivative of the electron concentration. Photovoltaic current is not present in BSO and is not considered here, but can be applied to the model by adding its effect to Equation (4-26). Note that the diffusion coefficient is related to mobility through Einstein's relation

$$D_n = \mu \frac{k_B T}{q} .$$

(4-27)

The diffusion and drift lengths relate charge velocity and lifetimes to charge movement. The diffusion length is the square root of the product of the diffusion coefficient and the carrier lifetime and is defined as

$$L_D = \left[D_n \tau_0 \right]^{1/2} = \left[\frac{D_n}{\gamma_R N_A} \right]^{1/2}$$

(4-28)

where the definition of carrier lifetime τ_0 is used on the right-hand side. A term for drift length relates the charge mobility, field strength, and lifetime to a distance,

$$L_e = \mu E_0 \, \tau_0 \; = \; \frac{\mu E_0}{\gamma_R \, N_A},$$ (4-29)

though this is term may be misleading. The large, externally applied fields used in the EOPL will dominate diffusion current and the distribution of charge, but the results of the coupled equations show that drift fields are affected by field shielding. The electric field $E(x)$ in Equation (4-26) is due to the applied electric field or any charge separation within the crystal. The EOPL requires an external half-wave voltage applied to the crystal. The uniform, externally applied voltage is $V_\pi/d = E_\pi$, or in general

$$V_\pi = \int_{-d/2}^{d/2} E_\pi \, dx$$ (4-30)

where d is the distance between electrodes. Figure 4-9 shows how the photoionized electrons drift toward the positive terminal where they eventually recombine with ionized donors. Charge photoionization, migration, and trapping result in charge accumulation at the illumination dark edge. The charge migration creates an electric field that must satisfy Poisson's equation, which can be expressed as

$$\frac{d}{dx}\varepsilon E = \rho = q(N_D^+ - N_A - n)$$ (4-31)

where ϵ is the static dielectric constant of the crystal given as $\epsilon = \epsilon_0 \epsilon_R$. A summary of the material properties for BSO used in this discussion is given in Table 4-1.

Table 4-1 Material Properties for BSO

Number density, donors	$N_D = 10^{+19}$ cm^{-3} [48]
Number density, acceptors	$N_A = 10^{+16}$ cm^{-3} [48]
Rate of thermal generation of electrons	$\beta = 5.3 \times 10^{-9}$ sec^{-1} [48]
Photo-excitation cross section	$s = 1.06 \times 10^{-1}$ cm^2/Joule [51]
Rate of electron recombination	$\gamma_R = 1.6 \times 10^{-11}$ cm^3/sec [48]
Mobility	$\mu = 3 \times 10^{-2}$ cm^2/(volt-sec) [48]
Diffusivity	$D_n = 7.7 \times 10^{-4}$ cm^2/sec
Excess carrier lifetime	$\tau_0 = (\gamma_R N_A)^{-1} = 6.25 \times 10^{-6}$ sec
Diffusion length	$L_D = 0.7$ μm [48]
permittivity, $\epsilon = \epsilon_o \, \epsilon_r$,	4.9584×10^{-012} coulomb/(volt-cm)
relative permittivity	$\epsilon_r = 56$ [48]
Electro-optic coefficient	$r_{41} = 5 \times 10^{-12}$ m/V [37]
Refractive index	2.5 [37]
Dark conductivity	1.0×10^{-15} (Ω cm)$^{-1}$ [49]

4.3.2 Steady-State Solutions for Kukhtarev's Band-Transport Equations

The previous section described the differential equations that are used to define the

photorefractive band-transport model of Kukhtarev *et al.*[50] The coupled differential

equations are intrinsically nonlinear so an analytic solution has not been determined.

There has been interest in approximate, analytical, steady-state solutions that describe the

optical and electric properties of diffraction gratings, including dynamic holographic

gratings. [39,40,45,51] Analytical solutions discussed in the literature are principally only

valid for small contrast gratings that take into account only the first-order solution, with

extensions to the linearized solutions being reported as well. For the case of no

externally applied field, a very simple analytical solution is useful for describing the

EOPL when the applied electric field is completely shielded. This solution is now

described.[38,51]

4.3.2.1 Analytic Solution for Zero Applied Field

A good approximation for $E_{sc}(x)$ in the steady-state condition can be obtained by solving

Equation (4-26) when no external electric field is applied. In this case the total current

density vanishes, so drift and diffusion current densities have equal magnitude and

opposite sign. Thus, solving for $E(x)$ in Equation (4-26) gives the following result:

$$E_{sc}(x) = \left(\frac{k_B T}{q} \right) \left[\frac{\beta}{s} + I(x) \right]^{-1} \frac{\partial I(x)}{\partial x} \approx \left(\frac{k_B T}{q} \right) \frac{\nabla I(x)}{I(x)} . \qquad (4\text{-}32)$$

The approximation on the right side is obtained by ignoring the dark illumination, β/s,

which can be much less than the applied intensity. Results for $E(x)$ with Gaussian

illumination are shown in Figure 4-10. Part (b) gives a plot of $E_{sc}(x)$ using Equation

(4-32) for two orders of Gaussian beam illumination intensity, $I_0 = 10^0$ & 10^2 W/cm^2,

shown in part (a). The charge density $\rho(x)$ shown in part (c) is determined from the

electric field using Poisson's equation, and the refractive index difference Δn shown in

part (d) is obtained from Equation (4-5) using the EO coefficient for BSO.

The EOPL uses an externally applied, half-wave voltage that prevents using

Equation (4-32) to solve for $E_{sc}(x)$; however, this result will be used in the next section
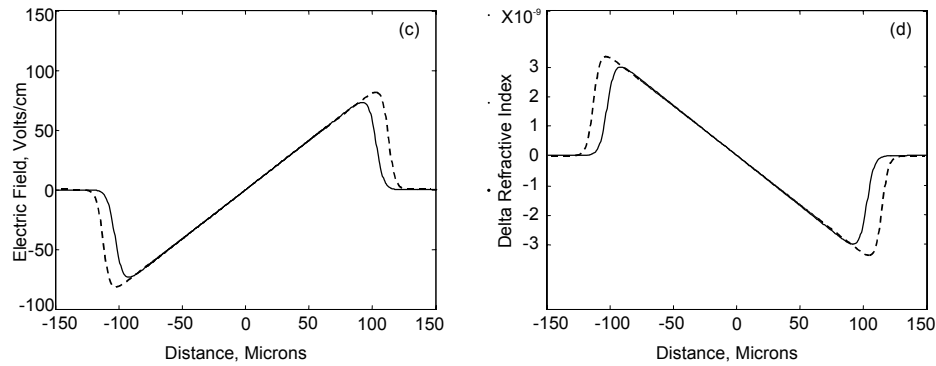
Figure 4-10 Solution for no external applied field (a) Illumination intensity, (b) charge density, (c) electric field, (d) refractive index change.

to show that in the region where space charge completely shields the externally applied field and $E_{sc}(x) = 0$, the result of Equation (4-32) applies.

4.3.2.2 Approach for Numerical Solution of Space Charge Field

The application of electric fields to enhance diffraction-grating efficiency and to generate soliton propagation modes[52,53] has generated interest in numerical solutions for $E_{sc}(x)$. Efficient numerical solutions for the photorefractive model have been developed[54] and are best used to analyze the EOPL because large optical and electric fields are applied to the crystal. The starting point for obtaining a numerical solution is the standard, coupled differential equations that comprise the photorefractive model. They are repeated here for the steady-state conditions where no differential current exists, the

electron generation rate equals the recombination rate, and the gradient of the charge density is zero. In the equations that follow, notation is made of those variables having a dependence on the independent variable x;

$$\gamma_R n(x) N_D^+(x) = (s\,I(x) + \beta)(N_D - N_D^+(x)) \qquad (4\text{-}33.1)$$

$$\frac{d}{dx}\varepsilon\,E(x) = \rho(x) = q(N_D^+(x) - N_A - n(x)) \qquad (4\text{-}33.2)$$

$$j(x) = qn(x)\mu\,E(x) + k_B\,T\mu\frac{dn(x)}{d(x)} \qquad (4\text{-}33.3)$$

$$\frac{d}{dx}j(x) = 0. \qquad (4\text{-}33.4)$$

The numerical approach outlined by DelRe et al,[54] that was used to obtain a solution for $E_{sc}(x)$ in an EOPL is now described. Considering Equations (4-33.1 - 4), a single differential equation is obtained by making three observations: (1) current density J in Equation (4-33.3) is constant, (2) Equation (4-33.2) allows $dE(x)/dx$ to be expressed in terms of N_D^+ and when substituted into Equation (4-33.1) gives an expression for $n(x)$ in terms of $dE(x)/dx$, and (3) the excess charge density $n(x)$ can be neglected with respect to N_D^+. The observations are used in order to obtain the single differential equation containing $E(x)$

$$\frac{q\mu(\beta + sI(x))\left(N_D - \dfrac{\varepsilon}{q}\dfrac{d}{dx}E(x) - N_A\right)}{\gamma\left(\dfrac{\varepsilon}{q}\dfrac{d}{dx}E(x) + N_A\right)}E + \frac{d}{dx}\left[\frac{\mu k_b T(\beta + sI(x))\left(N_D - \dfrac{\varepsilon}{q}\dfrac{d}{dx}E(x) - N_A\right)}{\gamma\left(\dfrac{\varepsilon}{q}\dfrac{d}{dx}E(x) + N_A\right)}\right] = J_c. \qquad (4\text{-}34)$$

To solve Equation (4-34) it is recast in a dimensionless form by introducing the adimensional quantities $Y \equiv E/E_{Db}$, $\xi \equiv k_{Db}x$, $Q \equiv 1 + I/(I_d + I_c)$, and $G \equiv J_c/q\mu\beta E_{Db}$, where k_{Db} is the Debye wave number defined by $k_{Db}^2 = [q^2 N_A/(\epsilon k_b T N_D)](N_D - N_A)$, $E_{Db} =$

$(k_bT/q)k_{Db}$, $I_d = \beta/s$ the crystal dark illumination, and I_c is control illumination used to increase the power limiting threshold. After defining $\alpha = (N_D - N_A)/N_A$, and $\delta = \epsilon\, k_{Db}$ $E_{Db}/(Qn_A)$, Equation (4-34) can be rewritten as

$$\frac{QY\left(\alpha - \delta\dfrac{d}{d\xi}Y\right)}{\left(1 + \delta\dfrac{d}{d\xi}Y\right)} + \frac{d}{d\xi}\left[Q\frac{\left(\alpha - \delta\dfrac{d}{d\xi}Y\right)}{\left(1 + \delta\dfrac{d}{d\xi}Y\right)}\right] = G.$$

(4-35)

By considering the case of $N_A \ll N_D$, the following approximations are noted: $\delta \approx 1$, k_{Db}^2 $\approx q^2 N_A/(\epsilon k_b T)$, and $\alpha \gg 1$. In addition, the optical densities associated with this application confine $|dY/d\xi| \ll 1$, so that $dY/d\xi$ is neglected with respect to α. Using these approximations, a simplified expression for Equation (4-35) is

$$\frac{QY}{\left(1 + \dfrac{d}{d\xi}Y\right)} + \frac{d}{d\xi}\left[\frac{Q}{\left(1 + \dfrac{d}{d\xi}Y\right)}\right] = \frac{G}{\alpha} = g.$$

(4-36)

Solving Equation (4-36) for $Y(\xi)$ yields

$$Y = \frac{Q'}{Q} + \frac{g}{Q} + \frac{g}{Q}Y' - \frac{Y''}{1 + Y'}$$

(4-37)

where the primes indicate derivatives with respect to ξ. Solving Equation (4-37) will provide the desired solution for $E_{sc}(\xi) = Y(\xi)/E_{Db}$. A numeric solution of Equation (4-37) was obtained by using the boundary-value, problem solver program, BVP4C, available with the Matlab® math analysis program (see Appendix B for the Matlab® code). The choice of a boundary-value problem solver is based on the assumption that in the steady-

state condition the electric field at the crystal surfaces contacting the electrodes is constant by virtue of the externally applied half-wave voltage. A solution is sought over the interval [0, d], where d is the crystal width between electrodes, hence the boundary conditions are $Y(\xi = 0) = Y(\xi = k_{Db}d) =$ the normalized value for the externally applied electric field, see Equation (4-30). Because boundary-value problems may have more than one solution (or none or infinitely many solutions), solvers require that an initial guess for the solution be provided, as well as, if necessary, initial guesses for the derivatives of the solution. The quality of the initial guess is critical for the solver's performance and even successful computation. The initial guess for $E_{sc}(x)$ assumes that the illumination is much smaller than the dark illumination and therefore $E_{sc}(x)$ equals the constant, externally applied field. The derivative of this field is zero.

Equation (4-37) is applied to the boundary value problem program by rewriting it as an equivalent system of first-order differential equations. Using the substitution $Y_1 = Y$ and $Y_2 = Y'$ the result is

$$Y_1' = Y_2$$
$$Y_2' = Y_1 + Y_2\, Y_1 + \frac{Q'}{Q} + \frac{Q'}{Q}Y_2 - \frac{g}{Q} - 2\frac{g}{Q}Y_2 - \frac{g}{Q}Y_2^2.$$

(4-38)

The parameter g is the normalized constant current density given in Equation (4-34). The boundary conditions used here are the field strength at the electrodes $g \equiv -V_\pi/(d\, E_{Db})$, where d is the distance between the electrodes. It is assumed that in steady state the parameter g is a constant current density. When solved numerically, g agreed closely with the definition, $g_{min} \approx -V_\pi/(D \times E_{Db})$, given in reference [54].

In order to troubleshoot the code and test the accuracy of the model, examples and results reported by Singh *et al* [51] for sinusoidal intensity gratings were compared to calculations obtained using the model discussed in the previous paragraphs. Figure 4-11 shows the space-charge field results obtained from illumination having the following form:

$$I(x)=I_0\left[1+m\cos(\frac{2\pi}{\Lambda}x)\right]e^{-(x-x_{mid})^8/\sigma^8} \qquad (4\text{-}39)$$

where m is the modulation index, Λ is the modulation wavelength, and the exponential function is a super-Gaussian, with half-width given by σ, that effectively approximates a rect function located at the midpoint of the crystal. In the figure, (a) is $E_{sc}(x)$ resulting
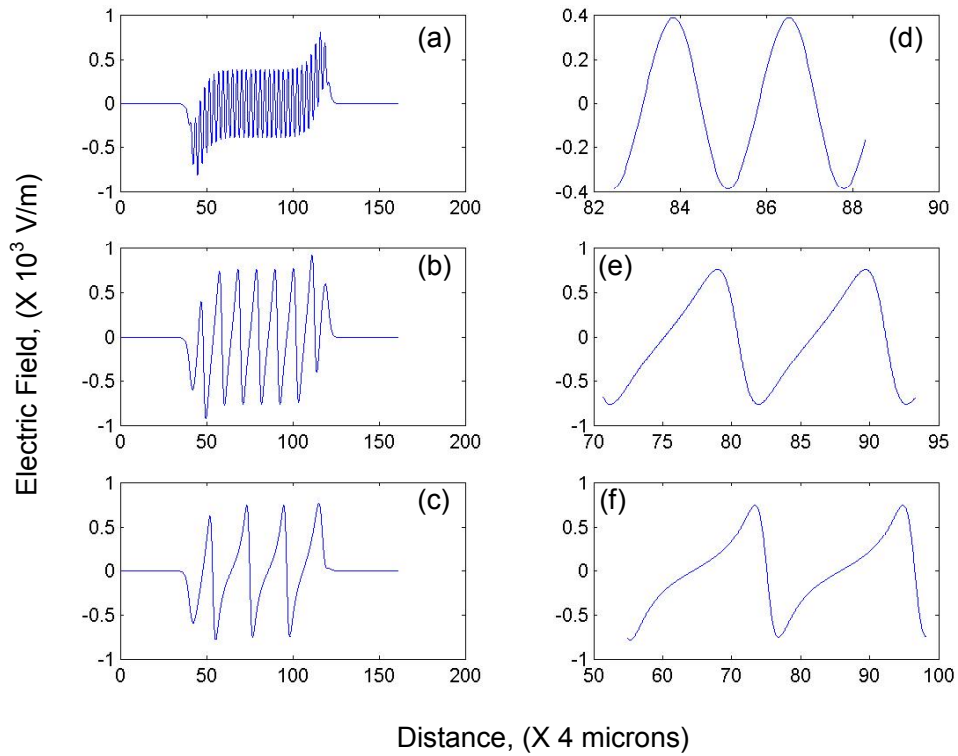
Figure 4-11 Numeric solutions for space charge field and TWM application used to compare known results from reference [51].

93

from a sinusoidal input function with modulation m = 0.1, wavelength Λ=10 μm, and

bounded by a super Gaussian function with radius σ = 120 μm. (b) is modulation m = 1,

Λ = 40 μm, and (c) is modulation m = 1, Λ = 80 μm. Subplots (d), (e), and (f) show

respective enlarged regions to give detail.

4.3.2.3 Numerical Space-Charge Field Results for Gaussian Beam Illumination

Numerical solutions for the space charge field $E_{sc}(x)$ were calculated in order to examine

the nature of the amplitude response for the EOPL notch-filter function over a range of

illumination intensities. Results of these calculations were for the most part identical to

that calculated using the analytic model of Chang et al [42],with results shown in Figure

4-7. The purpose of the numerical solutions for $E_{sc}(x)$ was to examine spatial response

for the EOPL notch-filter function over a range of illumination intensities. Results are

presented in Figure 4-12. The range of Gaussian beam input illumination intensity used

in the numeric solutions is plotted in part (a). Using an analytical equation for the input

illumination makes the calculations easier, and spline functions can be used to represent

any input function analytically. Our approach was to use simple Gaussian-beam intensity

distributions given by the equation

$$I_{in}(x) = I_0 \exp\left(-\frac{x^2}{W_0^2}\right)$$

(4-40)

where W_0 is the $1/e^2$ width, selected to be 25 microns. Figure 4-12 (a) shows seven

intensity plots that were used as input functions. The peak intensity, $I_0(x)$, is varied in

each plot by two decibels and ranges from 10^{-8} to 10^4 W/cm^2. The range of the spatial

dimension x was -150 to 150 microns, with the beam centered at zero. The results of
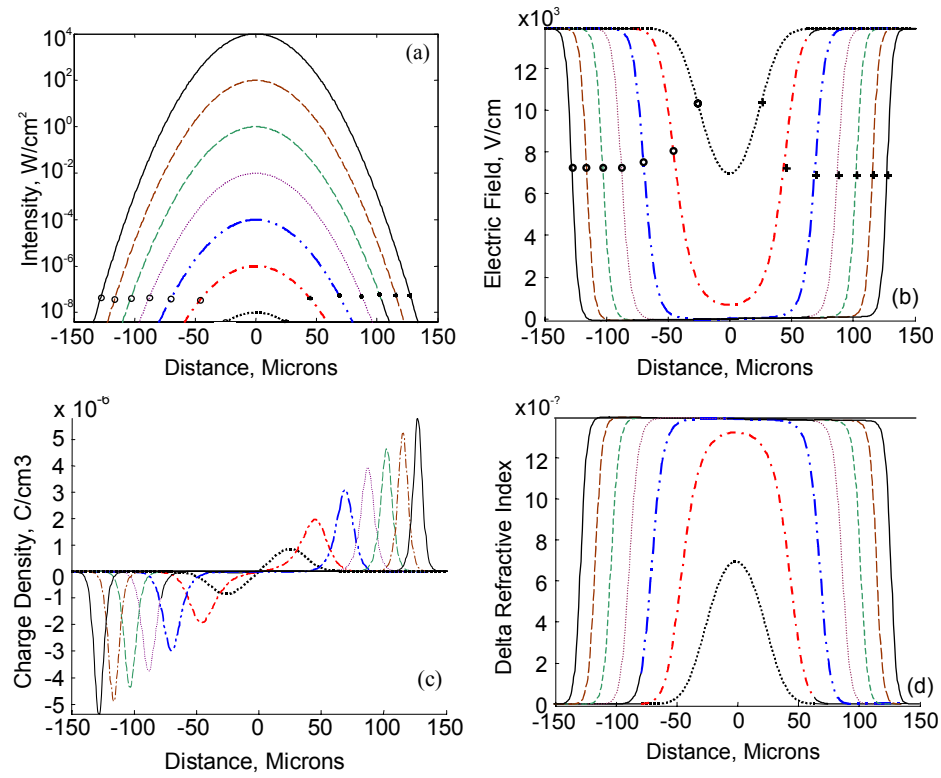
Figure 4-12(a) Gaussian beam illumination with $I_0 = 10^{-8}$ to 10^{+4} W/cm^2 and $1/e^2$ radius = 25 μm. (b) Numeric solution of $E_{sc}(x)$ for external field E = 13,913 V/cm. (c) Charge density obtained from $E_{sc}(x)$ and Poisson's equation. (d) Delta refractive index using $E_{sc}(x)$ and Equation (4-5). Note in (a) and (b) + & 0 marks the charge density peaks from (c).

Equation (4-38) for determining space charge field $E_{sc}(x)$ are plotted in part (b). These results and Poisson's equation, $dE(x)/dx = 4\pi\rho/\epsilon$, were used to calculate the distribution of charge density shown in Figure 4-12 part (c). Note that the charge distribution is symmetric (for the most part--see the enlarged detail shown in Figure 4-14) with positive and negative peaks that form an effective charge dipole. The change in refractive index due to the EO effect was calculated using the EO relation $\Delta n = n^3 r_{41} \times E_{sc}(x)$. Note that the index variation forms a Gaussian shape that flattens out with increased illumination as the space-charge field builds. When the shape of Δn is compared to Figure 4-10 (d), it is

95

apparent why an externally applied field is needed for applications where photorefractive index variations are used to create guided or soliton propagation modes.[52,53]

In Figure 4-12, parts (a) & (c) the peak charge positions are annotated on the plots by o's for the negative peaks & +'s for the positive peaks. The annotations make it easy to see that the charge accumulates about the region that is defined by the dark-illumination intensity. Thus, in the steady-state condition, mobile charges migrate (are swept by drift and diffusion forces) out of the illumination region and into the dark region where the excess carriers are trapped. Recall that the dark-illumination intensity is defined by $I_d = \beta/s + I_c$, where I_c is a uniform control beam that is used to increase the threshold intensity. In this series of calculations, I_c is zero. This result shows why the control beam works to raise the power-limiting threshold.

The mobile charge is well confined in the dark regions. Generalizations with regard to charge density at the dark edges and diffusion, drift, and Debye lengths (given respectively as $L_d = \mu k_B T/q \gamma_R N_A = 0.7 \mu m$, $L_E = \mu E_0/\gamma_R N_A = 26 \mu m$, and $L_D = \sqrt{(k_B T \epsilon/q^2 N_A)} = 0.9 \mu m$) were not seen. These parameters will be discussed in Section 4.3.2.4. Generally speaking, for beam sizes of a few microns, the notch width for adaptive power limiting is a function of the dark intensity (or uniform, control beam-intensity) and is created by charge accumulation at the uniform dark regions for the regions of the high-intensity beams that have intensity greater than in the uniform dark regions. Thus, the factor that delineates the EOPL notch width is the dark-illumination intensity I_d (or with addition of a control bias beam $I_{dc} = \beta/s + I_c$).

Greater intensity beams create wider notch widths. The width, W_d (or W_{dc}), at the dark intensity I_d (or I_{dc}) can be calculated using Equation (4-40) for a Gaussian beam and solving for the beam width at the dark intensity accordingly,

$$W_d = 2W_0 \sqrt{-\ln\left(\frac{I_d}{I_0}\right)}$$

(4-41)

where $2W_0$ is the $1/e^2$ spot size, I_0 is peak intensity, and $I_d = \beta/s$ is the dark intensity (note, $I_c = 0$). Figure 4-13 shows a plot of Equation (4-41) for $I_d = \beta/s = 5 \times 10^{-8}$ W/cm^2 and I_0 range from I_d to $I_d \times 10^{10}$ (100 dB). The location of peak charge density shown in Figure 4-12 (b & c) are also plotted in Figure 4-13 where it is clearly seen that the EOPL notch width simply grows as a function of the dark intensity. For instance, Figure 4-13 shows that an unwanted high-intensity beam with intensity 50 dB greater than the desired signal
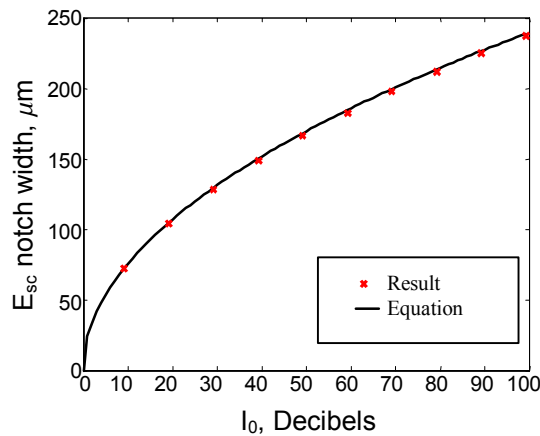
Figure 4-13 Solid line is Gaussian beam width at dark-intensity threshold for input beam intensity I_0 over a 100 dB range and half-width $W_0 = 25\ \mu$m. Numerical results are for field shielding notch width calculated for I_0 at 10 dB intervals.

97

has a notch width of 177 μm, a width that would attenuate around seven resolvable signal spots (figuring a 50 μm resolvable spot width).

Strong illumination results in a space-charge field that completely shields the applied half-wave voltage, as seen in Figure 4-12 part (b) for illumination greater than 10^{-5} W/cm^2. The numeric results show that when the applied field is completely shielded, rather than being a symmetrical dipole, there is a slight asymmetry between the positive and negative charge density peaks that have accumulated at opposite dark illumination edges. This asymmetry is difficult to see in Figure 4-12 part (c) because of the scale. In order to examine the asymmetry of charge density, $E_{sc}(x)$ was solved for different, externally applied field strengths. The results for three cases, 0, 73, and 146 V/cm are plotted in Figure 4-14. The peak Gaussian-beam illumination intensity $I_0 = 10^0$ W/cm^2 was identical for all cases. In all cases, $E_{sc}(x)$ shows identical linear dependence on position x in the central region where the external field is completely shielded by the charge dipole. The case of an externally applied field of zero was already discussed and is plotted in Figure 4-10 part (b). The linear dependence of the space charge is apparent from the analytic Equation (4-32). Substituting the Gaussian illumination intensity given in Equation (4-40) into Equation (4-32), shows that $E_{sc}(x)$ has an inverse dependence on the Gaussian-beam width W_0, as shown by

$$E_{sc}(x) \approx \left(\frac{k_B T}{q}\right)\frac{\nabla I(x)}{I(x)} = -\left(\frac{k_B T}{q}\right)\left(\frac{2}{W_0^2}\right)x \qquad (\ 4\text{-}42\ )$$

where this equation applies only to the case of zero externally applied electric field, as well as the region shielded by the charge dipole, that is, the region where the plots overlap in Figure 4-14, where the ambient coulomb field is zero. The constant slope,
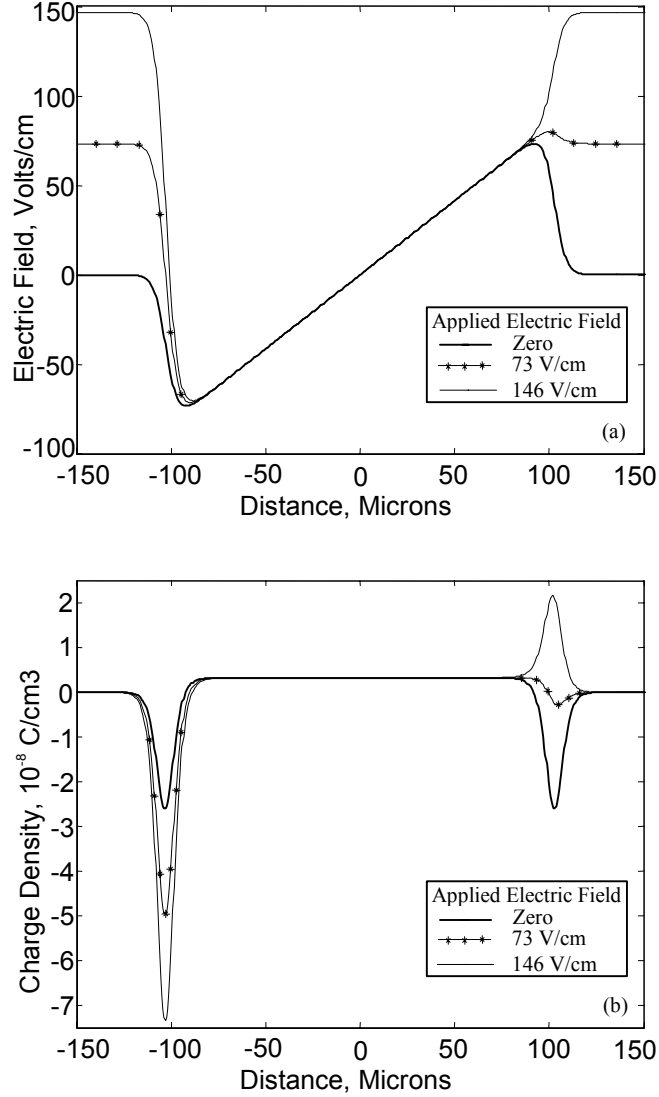
Figure 4-14 (a) Electric field for Gaussian illumination I_0=1 W/cm^2, W_0 = 25 μm, and three different external electric field values: zero, 73, and 146 V/cm. (b) Charge density for three conditions in part (a). Note: charge density, $\rho = 0.33 \times 10^{-8}$ C/cm^3, in center of the illuminated region results in a slight E_{sc} asymmetry between the two poles.

$-(k_B T/q)2/W_0{}^2$, is associated with a constant charge density, $\rho = 0.33$e-8 C/cm^3, obtained

by solving Poisson's equation, Equation (4-31), for the case where the Gaussian beam

radius is $W_0 = 25$ μm. Thus, when the externally applied voltage is completely shielded,

99

a constant charge density exists inside the illuminated region and the magnitude is dependent only on the beam radius and temperature, not intensity. This positive charge is balanced by mobile, negative charges that migrate out of the illuminated region. Figure 4-10 shows that increased illumination intensity increases the width of this constant charge density, which again is balanced by increased negative charge density at the dark illumination edges.

Figure 4-14 part (a) shows that $E_{sc}(x)$ peaks at $E_{sc} = 73$ V/cm for zero externally applied field. By externally applying 73 V/cm, a balance between $E_{sc}(x)$ and the applied field occurs. All negative charge is swept toward the positive terminal, doubling the charge density on that side and eliminating the excess negative charge density at the dark-illumination edge toward the side of the negative terminal. Increasing the externally applied field beyond 73 V/cm creates a region of positive charge density at the dark-illumination edge opposite the negative charge. The positive charge density at the edge and at the center balances the negative charge density at the opposite dark-illumination edge. Positive charge accumulates at the dark-illumination edge anytime the externally applied field cannot be balanced by the constant charge density in the illuminated region. Positive charge is bound to the lattice, yet a large accumulation of positive charge exists at a dark edge, suggesting that the positive-charge generation rate could be related to the dark intensity (control beam) where the positive charge accumulates. However, Guo *et al* [44] reports that the dynamic response of the light attenuation showed no dependence on control-beam intensity I_{dc}, only the signal beam intensity affected response time.

4.3.2.4 Numeric Space-Charge Field Solutions Using Pseudo δ-Function Illumination

When a beam of light creates a source of excess electrons in the crystal, the mobile

electrons diffuse and drift away from the source and then decay by recombination over an

average lifetime τ_0. Charge is constantly ionized within the illuminated region, and in

steady state there is an accumulation of charge density at the dark edge. It may be

assumed that charge collects at the dark edges according to an exponential decay of free

carriers in the conduction band that are trapped at a distance x from the dark edge. The

exponential decay is given according to equations

$$\delta n(x) = \delta n(x_0) e^{-x/L_D} \quad x \geq 0$$
$$\delta n(x) = \delta n(x_0) e^{+x/L_D} \quad x \leq 0$$

(4-43)

where x_0 is the location of the dark edge. Figure 4-15 shows a normalized plot of charge-

density decay according to Equation (4-3) for diffusion length defined in Equation
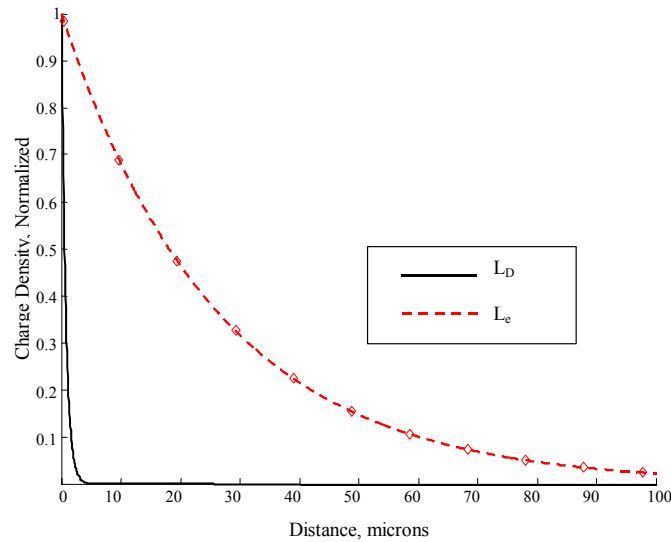
**Figure 4-15 Exponential charge decay showing idealized
drift and diffusion lengths.**

101

(4-28), where $L_D = 0.69 \mu m$ for BSO; and drift length defined in Equation(4-29),

where $L_e = 26 \mu m$ for BSO, and external applied field $E = 13{,}913$ V/cm.

The charge density plots in Figure 4-12 (c) and Figure 4-14 (b) show, for each

value of I_0, a uniform spatial confinement of charge density at the dark edges, indicating

that the confining forces, that is, coulomb, diffusion, and drift, are not showing a

preferential direction for the illumination beam width, $W_0 = 25 \mu m$, used in that example,

especially with regard to drift length. The wide spots sizes used in the previous figures

were chosen for this purpose, as well as to match experimental beam sizes. Pseudo-delta

illumination functions were applied to the model in order to investigate the limits on

charge confinement with respect to drift and diffusion lifetimes. Delta function

illumination was approximated by the following equation:

$$\delta(x) = \lim_{W_0 \to 0} \frac{1}{W_0} \exp\left[-\pi \left(\frac{x - x_0}{W_0} \right)^2 \right] \qquad (4\text{-}44)$$

and applied to the numeric space charge model. The results are plotted in Figure 4-16 for

three beam widths, $W_0 = 0.005$, 0.05, and 0.5 μm. Charge diffusion is clearly seen for

$W_0 = 0.005 \mu m$, but the one-micron beam width falls off in the manner of the applied

Gaussian illumination and shows no distortion in shape due to charge diffusion. The plot

shows that an assumption of simple exponential decay with diffusion length L_D is

consistent with the results of the numerical solutions for no externally applied field.

In another series of solutions, an electric field $E = 13{,}913$ V/cm was applied and

the illumination function was again as series of approximated delta functions having

widths $W_0 = 0.05$, 0.5, and 1.0 μm. The results are plotted in Figure 4-17. The plot
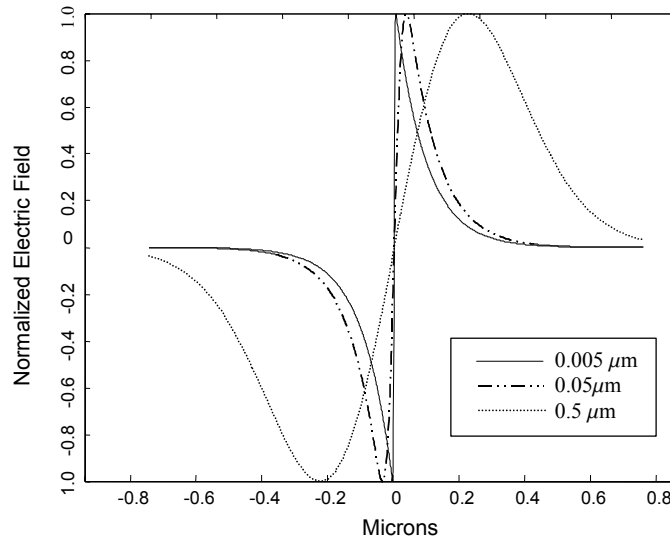
Figure 4-16 Space charge field for approximate delta function illumination having radius, $W_0 = 0.005$, 0.05, and $0.5\,\mu$m, and no external field.

clearly shows the effect of charge drift due to the external field; however, the charge is confined to within one micron of the beam center, and the result for the one-micron radius beam has no pronounced distortion in the space-charge shape. The simple assumption of exponential decay according to a drift length obtained from Equation (4-29), $L_e = 26\,\mu$m, obviously does not apply, indicating that drift length is not a useful measurement of charge confinement when applied in this manner. Figure 4-12 (c) shows that at the dark edges the charge density exponential decay length is decreased slightly as the charge density increases for increased optical power. Thus, even with large external fields applied to the crystal, the dynamic field and charge relationships provide adequate charge confinement to create useful notches in the applied field that controls EO birefringence and amplitude modulation of strong signal beams applied to the EOPL.

103
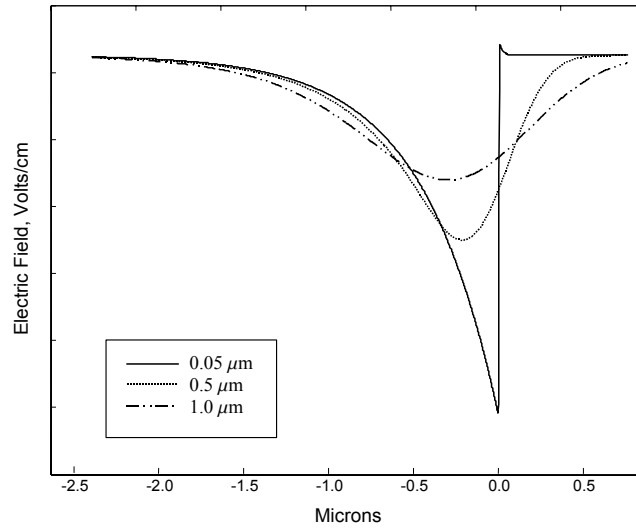
Figure 4-17 Space charge field for approximate delta function illumination having radius, W_0 = 0.05, 0.5, and 1.0 μm, and 13913 V/cm external field applied.

4.4 EOPL Notch-Filter Width Analysis

An illustrative example for EOPL notch width in a frequency-domain optical processor is given. The number of resolvable spots is 100 and each resolvable spot has 50-micron width. The A-O bandwidth is 20 MHz, and there is 2.5 mm spatial distance between the highest and lowest frequency in the optical Fourier transform plane. An EPOL is inserted at the Fourier transform plane to achieve adaptive notch filtering. A heterodyne-detection reference beam floods the crystal with 1×10^{-3} W/cm^2 optical intensity and functions as an optical control to raise the power-limiting threshold intensity of BSO by 50 dB. A probe/signal beam has an intensity 1×10^{-3} W/cm^2. Two high-intensity beams located on each side of the signal beam have power 50 dB greater than the signal beam. From Figure 4-13 this undesired high-intensity beam creates a space-charge field in the

BSO crystal that attenuates optical power over a distance of 150 microns, a width

approximately equal to $3\Delta t$ for the Bragg-cell resolvable spots. The positions of the two

undesired beams are selected for this example so that the signal beam will not be

attenuated over its 50-micron resolvable spot size. Figure 4-18 shows solutions for the

optical intensity at the output of the polarized beam splitter as a function of spatial

frequency. The upper, dashed line is the input illumination intensity. The solid line is

the output intensity calculated from Equation (4-9) using a numeric solution for $E_{sc}(x)$.

The lower dashed line is the output calculated point by point using the analytic formula

based on photoconductivity given by Equation (4-20). Note that the solution from

Equation (4-20) agrees quite well with the numerical solution except that it fails to

account for the slightly asymmetric charge density discussed earlier. The signal beam is

preserved when positioned in the dark region between the two undesired beams.
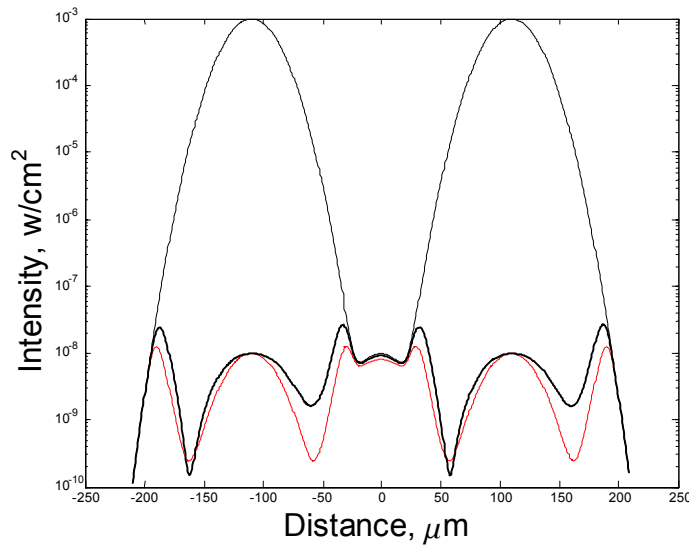
Figure 4-18 Optical power limiting calculated for three Gaussian beams, $I_0 =$ 10^{-3}, 10^{-8}, and 10^{-3} W/cm^2 respectively, $W_0 = 25 \, \mu$m, and separation 110 μm. Upper dash-dot line is input intensity, solid line is output intensity, and lower dotted line is simple model for power limiting.

Chapter 5

Experimental Results

5.1 Acousto-Optical Heterodyne RF Spectrum Analyzer

An acousto-optic RF spectrum analyzer with heterodyne detection was constructed to

demonstrate and study the principles of RF frequency excision in the Fourier transform

plane. This system is described in Section 5.1 and illustrated in Figure 5-1. Initial

experiments used a single-channel Bragg cell, and frequency excision was accomplished

by placing wire in the Fourier transform plane to excise signals.

The single-channel Bragg cell was replaced with a multi-channel Bragg cell in

order to test phase discrimination for Angle Of Arrival (AOA) excision. This system is

described in Section 5.1.3 and illustrated in Figure 5-9. Fiber-coupler heterodyning

proved most useful for these experiments, as the small acceptance angle was used to

show phase discrimination of signals, but also the spatial frequencies of the multi-channel

Bragg cell were small enough to fit into the 3dB acceptance angle of a single-mode optic

fiber. The results are shown in Figure 5-12.

Indirect measurements of EOPL notch depth and width were made by monitoring

the output while ramping power levels, sweeping an interference beam across a

stationary, small signal, and measuring the effect on the detected small signal. These

results are given in Section 5.2.3 and illustrated in Figure 5-32 through Figure 5-34.

5.1.1 Heterodyne RF Spectrum Analyzer Using Beam Splitters

Figure 5-1 shows a diagram of the A-O, heterodyne RF spectrum analyzer with frequency

excision that was built as a test-bed for these experiments.[29,30] The major features are the

Bragg-cell phase grating that forms an optical image of the RF spectrum discussed in

Section 2.5, Fourier Transform Using a Lens, page 19, the adaptive notch filter discussed

in Section 4.2, Photorefraction, page 72, and the overall system discussed in Section

3.2.3, Acousto-Optic RF Signal Excision, page 55.
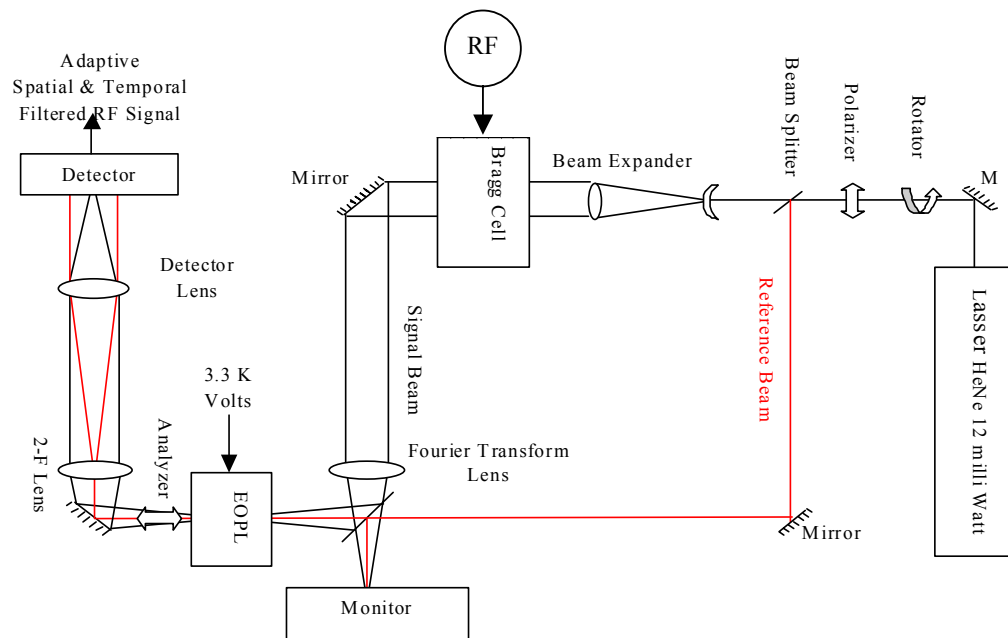
Figure 5-1 Diagram of acousto-optic RF signal excision experimental setup.

A laser beam is split into a signal and reference beam using one of two beam splitters, which forms a Mach-Zehnder interferometer. The signal beam is expanded to 6.5 mm to fully illuminate the aperture of a Bragg cell. Deflected light is focused with a 73-cm focal-length lens to form an RF spectrum of light at the Fourier transform plane. Figure 5-31, page 142, shows a beam scan (x-axis and y-axis slice) at the Fourier transform plane for two RF signals applied to the Bragg cell. The 400-micron separation between the two peaks on the x-axis is a function of the 4-MHz frequency difference between each signal applied to the Bragg cell, the number of gratings illuminated in the Bragg-cell time aperture, and the lens focal length. The width of these focused spots, 129 microns along the x-axis, and 241 microns along the y-axis, is a function of the beam size entering the lens.

Ideally, the signal and reference beams are mixed at a second beam splitter so that the reference beam uniformly illuminates the Fourier transform plane. In this manner the uniform reference beam provides the threshold intensity control for the adaptive optical power limiter. Also, the optical power limiter notch depth is doubled by decreased heterodyne detection when the reference beam is attenuated with the signal beam. Another benefit is that phase differences in the reference and signal beam are reduced as discussed in Section 3.2.3. The Mach-Zehnder configuration makes available two frequency planes for signal processing. The optical image processing device (EOPL in our case) is located at one frequency plane to excise unwanted spectral components. The other signal was not used in this experiment other than for monitoring. A detector may directly follow the Fourier transform plane, or a 2-f system of lenses can be used to

condition the beams in order to maximize heterodyne detection. Section 3.2.2,

Heterodyne Detection, page 52, details the stringent requirements for heterodyne

detection. The experiment varied from this description in a few ways that are explained

in subsequent sections of this chapter.
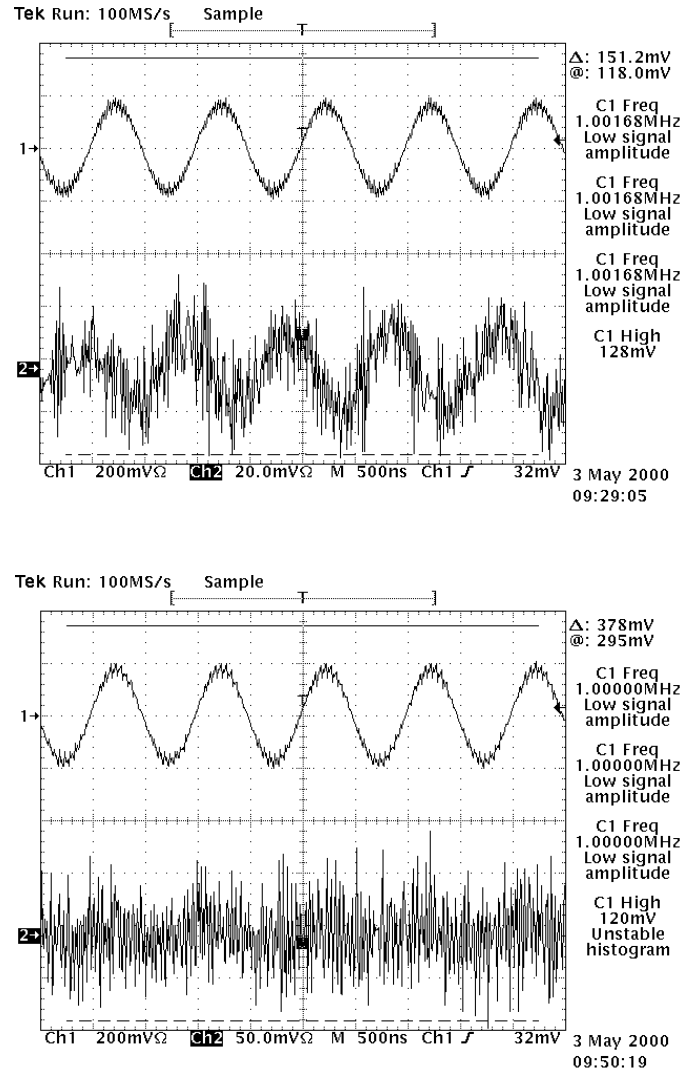
Figure 5-2 Recovery of IF signal passing through system. Lower screen has high intensity interference component that prevents recovery of the signal.

Ideally, an information-bearing, spread-spectrum signal at an intermediate frequency, IF, is mixed with a local oscillator (LO), and the resultant RF signal is applied to the Bragg cell for optical processing. The recovered RF signal is mixed with a second LO again to recover the IF signal as shown in Figure 5-9, page 116. Figure 5-2 is a display from a Tektronix TDS 460A digitizing oscilloscope showing a 1-MHz IF tone (1→) that was mixed with an 80-MHz LO and passed through the optical system. The recovered signal (2→) is shown in the lower trace. The recovered signal in the upper-scope screen shows the resultant system noise. The recovered signal in the lower-scope screen is washed out due to a high-intensity component added to the RF signal.

Figure 5-3 shows how the intensity of a weak, "desired" signal, plotted along the y-axis, is washed out as the power of an added RF interference component, of similar
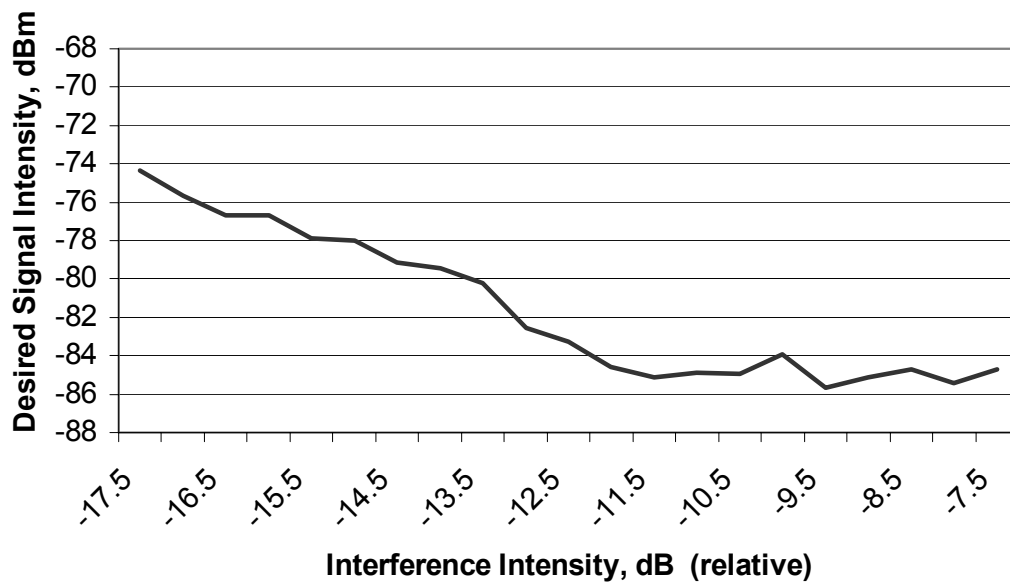
Figure 5-3 Signal washout due to high-intensity interference. Desired signal intensity versus interference intensity.

Frequency, plotted along the x-axis, is increased. The leveling off of the decreasing slope may be due to saturation of the Bragg cell or the noise floor limit was reached.

The system RF signal excision capability was tested using thin wire to block signal components at the Fourier transform plane. The results showed that RF excision resolution was half that expected from the calculations. Measurement of the deflected beam revealed that it was less than half the crystal width, so that the Bragg cell time aperture was only half the expected value. Figure 5-4 shows an image of the Bragg cell illuminated by the collimated laser beam. The white box on the right delineates a notch on the Bragg cell where the deflected beam originated. The deflected beam is seen to the left of the Bragg cell image, also delineated by a white box. A multi-channel Bragg-cell was obtained to study phase deflection, but was also used for single-channel experiments.
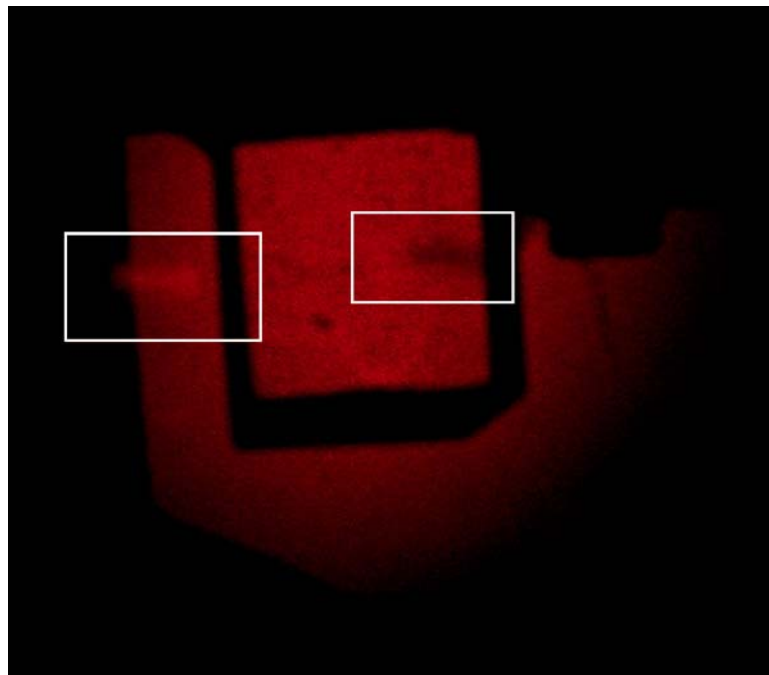
Figure 5-4 Bragg-cell deflection occurs in half the expected aperture. Deflected beam can be seen in the square on the left.

Unfortunately, signal resolution worsened because the new TeO$_2$ crystal was designed to operate in the longitudinal acoustic mode, υ_a = 5.5 Km/sec, rather than the shear mode, υ_a = 0.62 Km/sec, reducing the time aperture by almost an order of magnitude. The time aperture was not increased because of the size limitations of the lens and mirror used in the system.

Only a –70-dBm, heterodyne-detected signal (-90 RF noise level) was obtained with the Mach Zehnder interferometer. This was attributed to the low-precision alignment components that were available for this experiment, and also an oversight in conditioning the reference beam; that is, a sinc function imaged at the center of the Bragg cell as described in reference [31] was never tried. An optical power budget analysis on the Mach-Zehnder interferometer showed that a much larger signal was expected. The maximum raw signal level should have approached –16dBm (0.7 mA signal and reference beam detector current) using the 12-mW laser. Table 5-1 lists measurements of loss and power budget for each component in the setup.

Table 5-1 Power budget for AO RF signal excision experimental setup.

Device	Loss dBm				Power Level mWatts			
Laser					12.0			
Dielectric Mirror #1	0.17				11.55			
Rotator	0.61				10.04			
Polarizer	0.92				8.13			
	Signal		Reference		Signal		Reference	
Beam Splitter #1	1.15		7.34		6.24		1.5	
Bragg Cell	4.7		0.00		2.11		1.5	
Dielectric Mirror #2, #3	0.03		0.18		2.09		1.44	
Fourier Transform Lens	0.00		0.00		2.09		1.44	
	Signal 1	Ref. 1	Signal 2	Ref. 2	Signal 1	Ref. 1	Signal 1	Ref. 1
Beam Splitter #2	0.95	6.88	6.88	0.95	1.68	0.295	0.430	1.157
Detector Responsivity	0.5		0.5		Peak Signal mA		Peak Signal mA	
Maximum Signal Level	$2\times(I_{ref.}*I_{signal})^{1/2}$				0.7		0.7	
Power					-16.11 dBm			
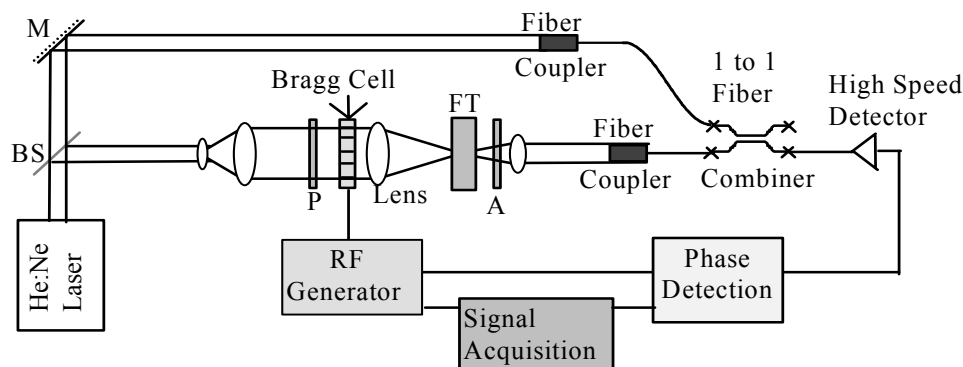
Figure 5-5 Acousto-optic RF excision using fiber optic coupler.

5.1.2 Heterodyne RF Spectrum Analyzer Using Fiber Coupler

The traditional Mach Zehnder interferometer was modified to take advantage of the precision fiber-optic components that were available in the lab. Fiber couplers provide excellent heterodyne detection results. Figure 5-5 shows a diagram of the fiber-coupler heterodyne detection approach used to increase the signal to noise ratio.

The noise created in the system was measured using an HP 8563E spectrum analyzer. Figure 5-6 shows the spectral intensity of an RF tone applied to the system and detected at the output. The laser noise extends over a 300-KHz range and is most likely due to unbalanced lengths of the signal and reference beams that exceeded the laser coherence length. The mismatch of the signal and reference beam path lengths is much different for the Mach-Zehnder and fiber optic coupler heterodyne schemes. The former matched path lengths within a centimeter, while the latter had a path length mismatch that was difficult to even estimate (so it wasn't). Unfortunately, a longer coherence-length laser was not available.

Heterodyne Detection @ 81.088 MHz
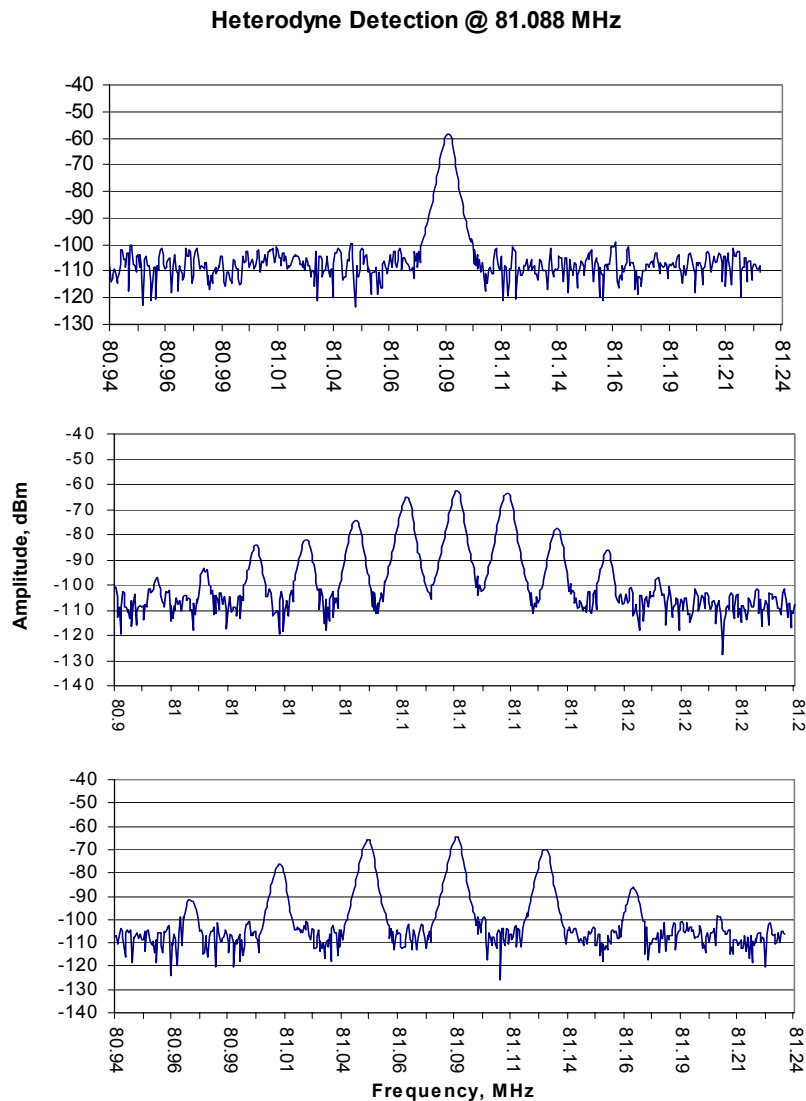
Figure 5-6 Laser noise for single tone passing through the fiber-optic heterodyne detection system.

The acceptance angle for the fiber-optic coupler was determined by measuring the

detected output as a function of the frequency applied to the Bragg cell. The results are

shown in Figure 5-7 where a 7-MHz range showed a –3-dB coupling bandwidth of

approximately 0.9 MHz. The fiber was positioned for maximum intensity at 81.1 MHz.

114
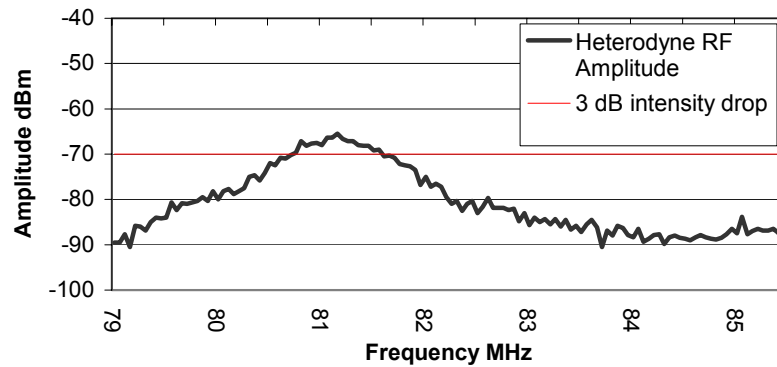
Figure 5-7 Fiber-optic coupling RF bandwidth.

The fiber-coupling bandwidth varied from 1 MHz to 3 MHz depending on the focal length of the lens (10 cm and 73 cm were used). This plot does not show the 50-dB+ signal-to-noise ratios that were eventually obtained with this fiber-coupler approach to heterodyne detection.

A decision was made that useful characterization of the optical power limiter could be simulated by using the fiber as a detector for a stationary small signal probe or test frequency. The effect on the probe signal as high-intensity interference signals were swept across the RF bandwidth would give a measure of the total system response.

5.1.3 Angle-of-Arrival Separation Using Multi-Channel Bragg Cell

A multi-channel Bragg cell was used to experimentally examine the separation of signals at the Fourier transform plane due to AOA. Our experimental results were consistent with the theory presented in Section 3.2.1.2, Multi-Channel Bragg Cells, page 49. A photo of the eight-channel Bragg cell is given in Figure 5-8.
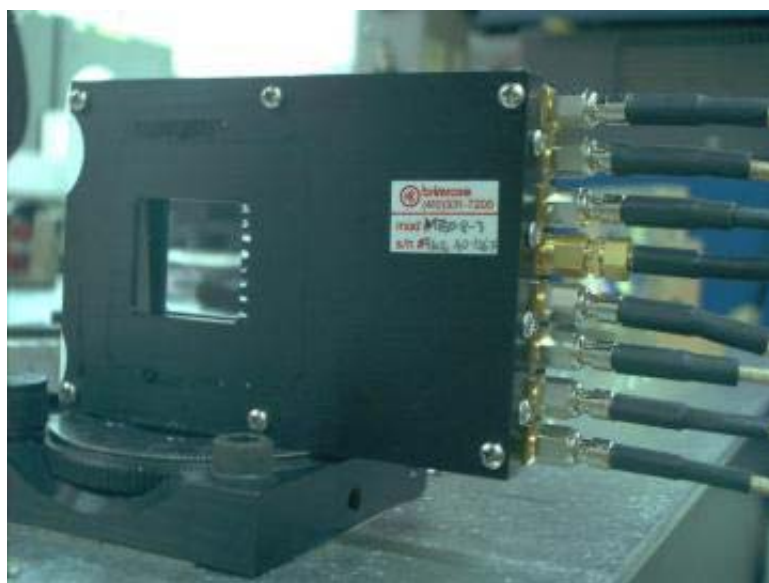
Figure 5-8 Eight channel Bragg cell.
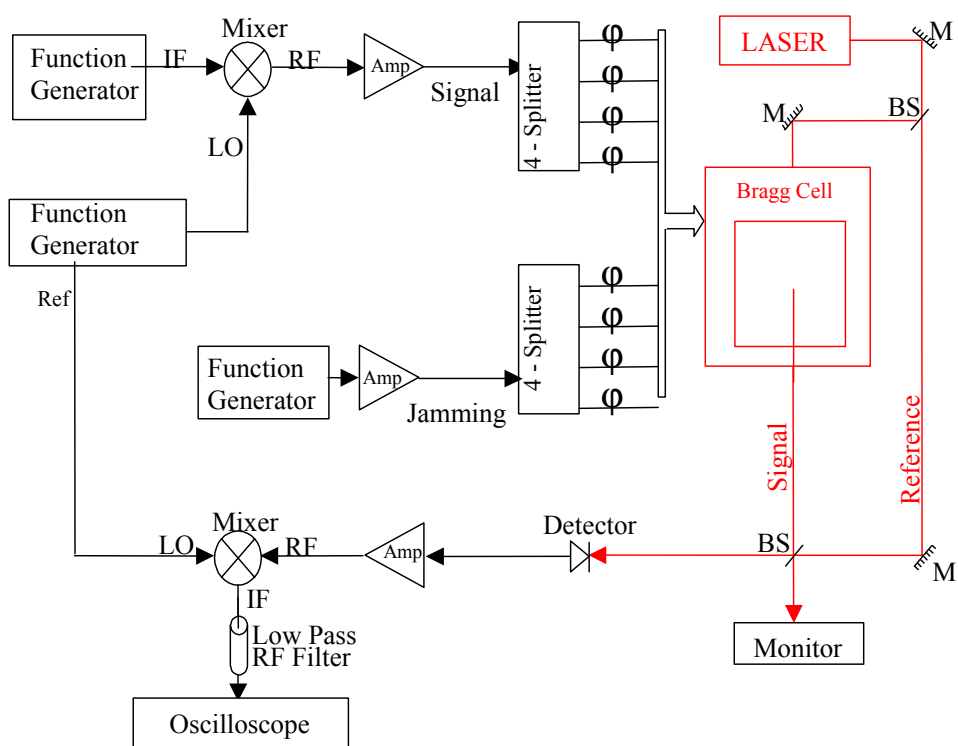
Figure 5-9 Experimental setup for 4-channel acousto-optic RF signal excision.

A diagram of the experimental setup is shown in Figure 5-9. Modifications, such as the addition of a fiber-coupler shown in Figure 5-5, were made to obtain some of the data presented. The multi-channel Bragg cell used in the experiments has properties listed in Table 5-2.

Table 5-2 Multi-channel Bragg cell properties

Item	MTED-8-3	Units
Optical wavelength range	400-840	nm
Acoustic mode	Longitudinal	-
Active aperture	1.0×20.0	Mm
Center Frequency	80	MHz
Bandwidth (3dB)	30	MHz
Optical transmission	>95	%
Maximum diffraction efficiency	70	%
Time-bandwidth product	141	-
Time aperture	4.7	μs
Number of channels	8	-
Center-center channel spacing	2.5	mm
Channel isolation	25	DB
Acoustic velocity	4.2×10^3	M/sec
Maximum electric input power	1	Watt
Input impedance	50	Ohms
V.S.W.R.	2.1:1	-
Optical polarization	Linear	-
Crystal material	TeO_2	

Figure 5-10 shows beam profiles for two cases of four-channel Bragg-cell operation, zero and 180° phase difference between each channel, that is, simulated AOA of boresight and +/-90° off-boresight. The profiles were obtained using a Photon Inc. Model # 0180–XYS/M laser-beam profiler. The resolution is 5 μm and the maximum beam width is 9 mm. The beam scanner provides two slices of the beam. The x-axis is the direction-of-frequency deflection (upper plot in figure), and the y-axis is the

direction-of-phase deflection for the multi-channel Bragg cell (lower plot). The shift in

azimuth giving the AOA for each spot is clearly seen. In the figure the plot on the left-

hand side shows the beams from each of the four individual channels at about half the

distance from the lens to the Fourier transform plane. The uneven amplitude is due to the

Gaussian illumination, and the Bragg-cell drive power gain could be adjusted to even the

optical intensity between channels. The middle plot shows the focused boresight beam at

the Fourier transform plane. Note the zero-order peak in the center and +/- first-order

peaks on either side. The first-order peaks are separated by a distance given by $f_{y\text{-max}} =$

$\lambda/d*f = 25 \ \mu m$ (50 μm total between both peaks), where $\lambda = 0.6328 \ \mu m$, channel

separation d = 2.5 mm, and lens focal length f = 100 mm. The plot on the right-hand side

had a 180° phase shift between each Bragg-cell channel, and this arrangement created

degeneracy between the +/- 90° off-boresight peaks. The +90° peak was suppressed

when the beam scan shown in this figure was captured. The four channels allow four
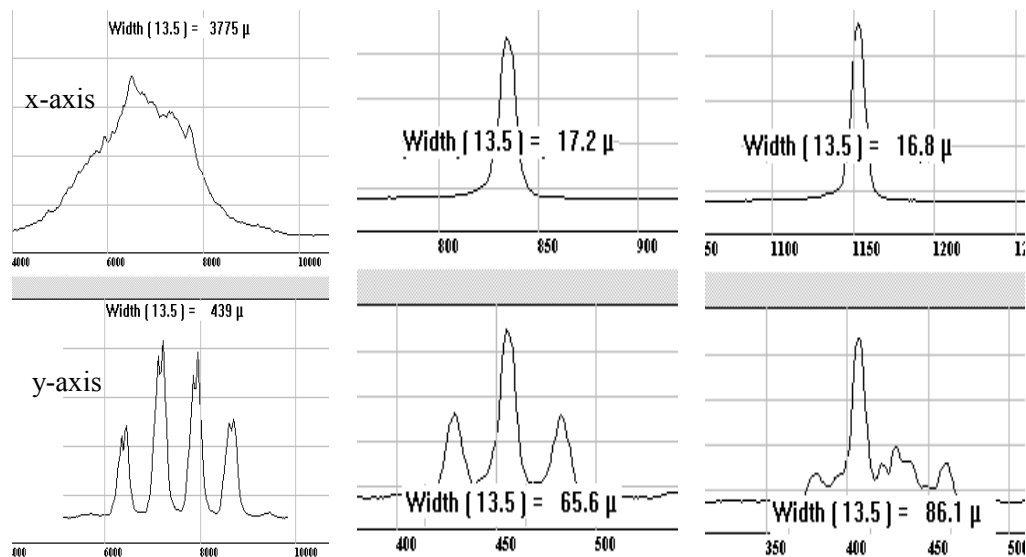
Figure 5-10 Beam scan of multi-channel A-O deflection and Fourier transform.

118

resolvable spots between the first-order bandwidth; that is, 50 μm ÷4 spots = 12.5 μm

/spot, which is close to the 17-micron spot sizes measured by the beam scanner.

The higher-order deflections that are inherent with the sin(Nx)/sin(x) relation for
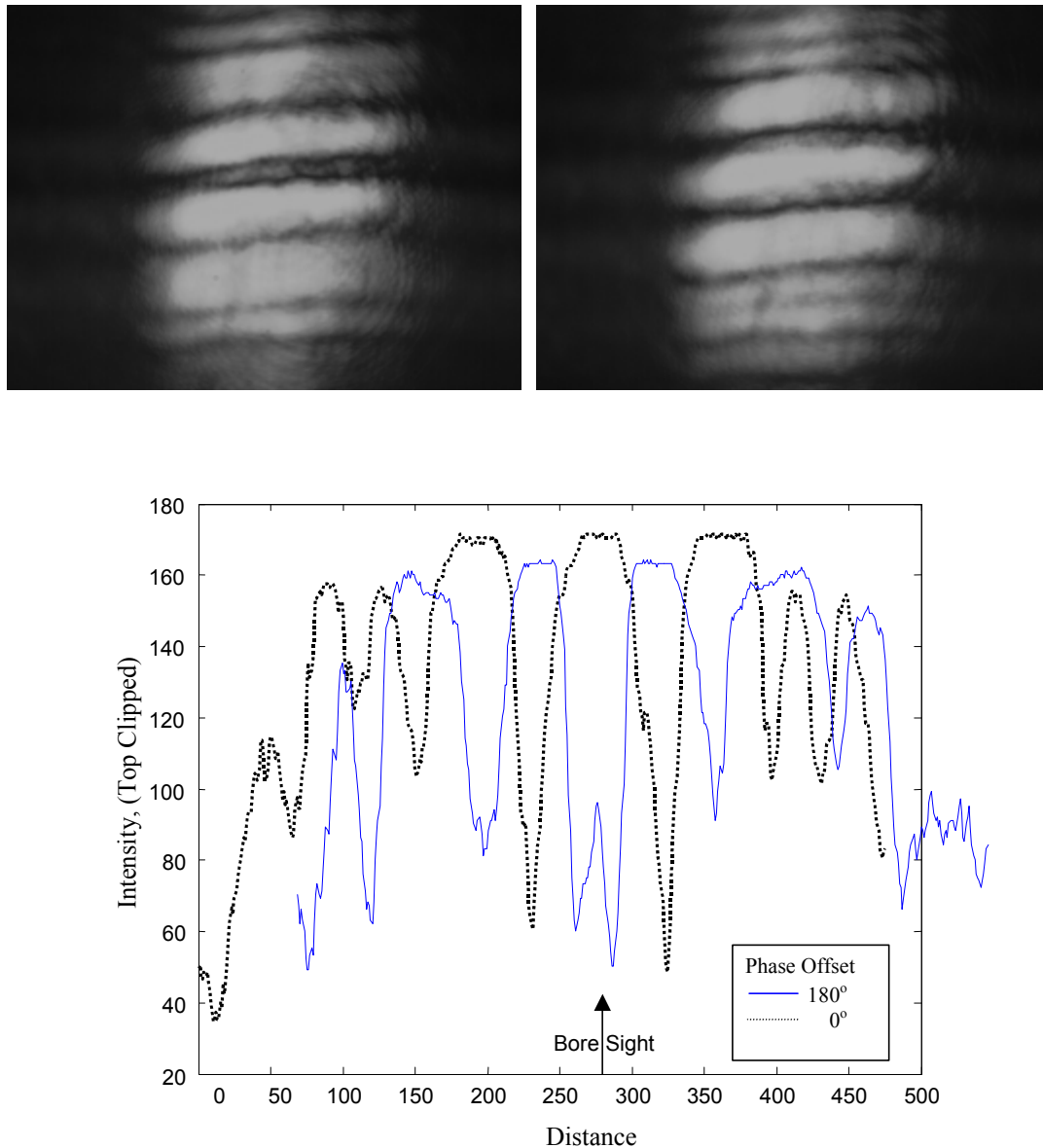
Figure 5-11 Eight-channel AOA deflection. Top left, 180° phase offset between each channel. Top right, no phase offset. Bottom, vertical slice of pixel intensity combined from both photos.

multi-channel radiators can be seen in Figure 5-11, which are CCD images of the Fourier transform plane. The CCD image on the upper, left side of the figure is the case of 180° phase offset between each channel, and the image on the upper right has no phase offset. The lower plot shows a vertical slice (Note: y-axis is rotated 90°) of the pixel intensity of each CCD plot. The two slices were laid on top of each other to show how the peaks overlapped. In order to account for slight misalignment between the capture of each plot, the 180° phase offset slice was aligned to match the first-order notch with the boresight position. The amount of shift is seen by the part of the line outside the border. Note that the strongest orders have clipped intensity, which was necessary in order to bring out the detail of the higher order, not visible using the beam scanner. Also, the 180° phase offset is degenerate between ± 90° AOA, and both peaks are clearly seen. In the beam scanner plot, a capture was made when the -90° AOA spot had subsided briefly.

Signal excision based on AOA was achieved by detecting only the signal of interest while excluding the unwanted signal. This was accomplished by positioning the single-mode, fiber-optic, heterodyne detector along the y-axis so that either both or only one signal was detected. The results for discriminating one or the other signal are shown in Figure 5-12, which clearly shows that one of the two signals is excised according to AOA. To better show the detail, the plot was created by subtracting the Bragg-cell power amplifier noise and the laser noise seen in Figure 5-6 from the detected signal. The AOA resolution for this example was better than that in Figure 5-10 because eight channels rather than four channels were used at the Bragg cell. The two tones were separated by 200 KHz so they could be identified in the spectrum-analyzer plots. The calculated beam
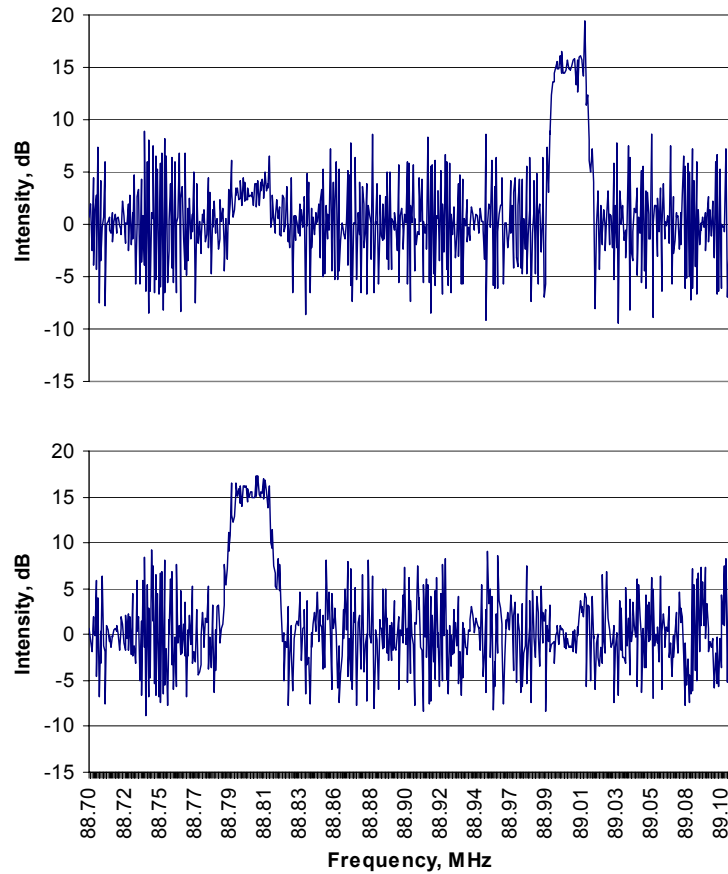
Figure 5-12 AOA signal discrimination using positioning of fiber optic detector.

separations on the y-axis (phase difference) is around 12.5 microns, and on the x-axis

(frequency difference) is 3 microns. The frequency separation is unresolved by the

system because the beam width along the x-axis is 17 microns, the same as in Figure

5-10, but the y-axis beam width is half as wide as before, as seen in Figure 5-11; thus, the

AOA excision results are clearly due to phase only and not frequency. The fiber

acceptance angle for the f = 100 mm lens used in this experiment corresponded to a

frequency bandwidth of 3 MHz. The fiber-coupling efficiency for the multi-order beams

was 16% (-7.7dB). It is assumed that only the zero order was coupled into the 5-micron

fiber core. The zero-order peak was measured to be 37.5% of the total diffracted light. The fiber-numerical aperture (NA) is 0.11.

5.2 Electro-Optic Power Limiter

The theory for the Electro-Optic Power Limiter (EOPL) is described in Chapter 4, Electro-Optic Power Limiter, page 60. The power limiter has been demonstrated in GaAs, CdTe, and BSO. Bismuth Silicon Oxide [$Bi_{12}SiO_{20}$] (BSO) is a particularly attractive photorefractive material due to its fast response, good optical quality, and high spatial resolution, so it is was chosen as the principal material to examine electro-optical power limiting for this research. The useful wavelength range for BSO is 0.4-0.7 microns. For this reason the power limiter can have wide-band wavelength responsivity. The crystal was configured for optical power limiting following the method reported by Steier *et al,* Chang *et al,* and Guo *et al* [2,42,44]. Once the crystal was properly set up for adaptive power limiting, experiments were done to determine the optical power limiting threshold, intensity transfer function, and optical notch width. The experimental results were consistent with the theoretical modeling. The EOPL reduced high-intensity optical beams by an amount equal to the extinction ratio of the polarizer and crystal combination, $\approx$ 40-25 dB for our setup. The benefit to interference reduction was apparent because with the EOPL powered off, the lock-in amplifier used to detect signals became overloaded. The notch widths were delineated by the region where optical intensity exceeded the uniform background intensity.
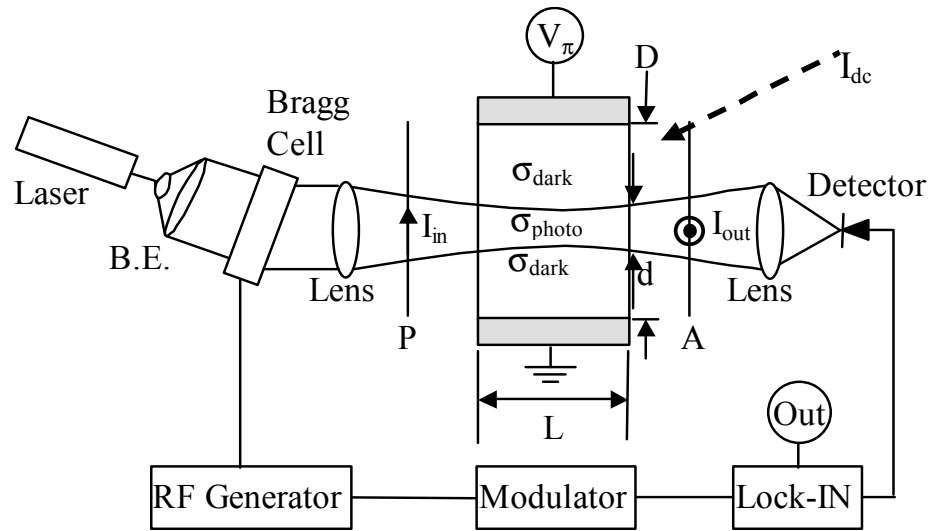
Figure 5-13 Diagram of optical power limiting device. B.E. = beam expander, P = polarizer, A = analyzer, I_{dc} = control illumination, d = beam width > I_d, D&L = crystal dimensions.

5.2.1 Preliminary Setup

BSO is a cubic crystal that was cut with three surfaces, (110), ($\bar{1}$10), and (001), and aligned as shown in Figure 4-2, which maximizes the EO effect.[37] Because the dark-intensity threshold is very low, 5×10^{-8} W/cm^2, the optic intensity was reduced by removing the Fourier transform lens, and the output from the Bragg cell was reduced in size to 1.4 mm using a diaphragm. Figure 5-13 shows the modified experimental setup.

The crystal was placed in a mount with some considerations made for applying high voltages, as well as micro-positioning in the x, y, and z (optic) axes. A picture of the mount and crystal is shown in Figure 5-14.

The crystal is placed between two crossed polarized beam splitters. The optimum angle of linear polarization was determined by finding a maximum polarization

123
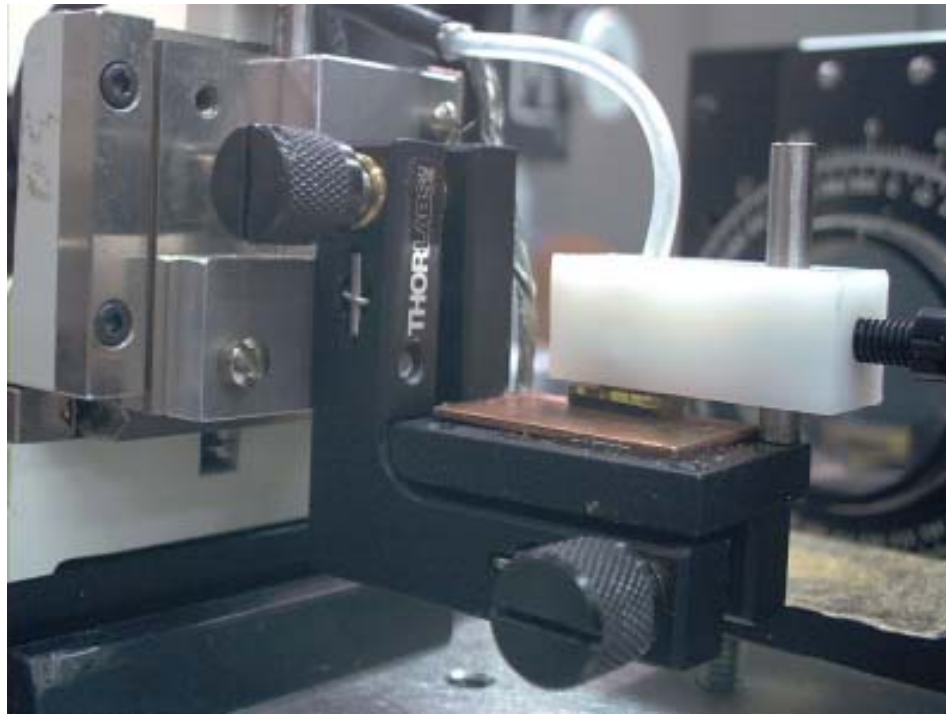
Figure 5-14 BSO crystal secured in high-voltage mount.

extinction ratio, as shown in Figure 5-15. The best angle corresponded to 45° (305°) from the x and y axes, as expected from the theory.

Figure 5-17 shows a plot of the optical output intensity versus external voltage applied to the crystal. The light intensity applied to the BSO crystal was kept below the dark-threshold intensity, because it was necessary to avoid attenuation due to any photorefractive field shielding. The plot was used to determine the half-wave voltage. Since a voltage of 3500 volts began to arc across an air gap on the mount, a value of 3100 volts was chosen as a safe half-wave voltage, slightly less than the 3300 volts half-wave voltage obtained from the plot. Even 3100 volts was a little high at times because of changes in humidity that occurred. This half-wave voltage result is much higher than Equation (4-7) predicts, due to optical activity in the BSO crystal.
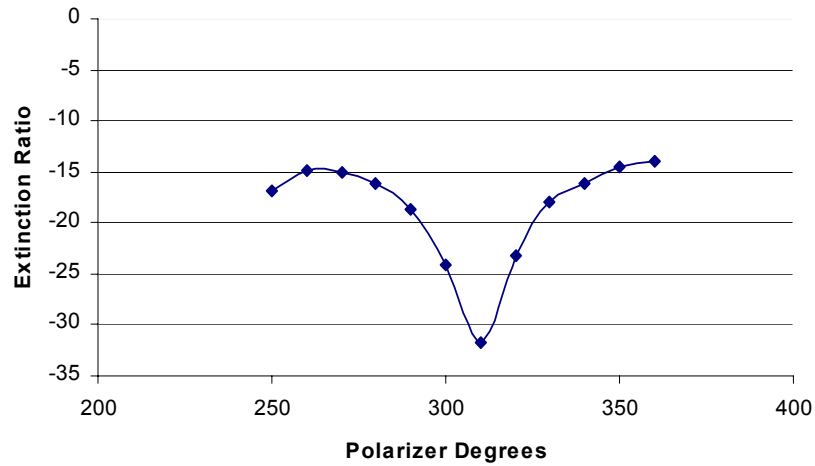
Figure 5-15 Extinction ratio for polarizer / BSO / analyzer combination versus polarization orientation.

The optical activity was removed by using a pair of quarter-wave plates between the crossed polarizers and crystal as shown in Figure 5-16. This configuration launches circular polarization into the crystal, which is a normal mode (eigenmode) for optically active crystals. The applied voltage versus transmitted light for the case of circular polarization is also plotted in Figure 5-17. Note that the half-wave voltage is about 1050 volts less for circular rather than linear polarization. Using $n^3 r_{41} = 82 \times 10^{-12}$ m/volts,[37] in Equation (4-7) gives $V_\pi = 1423$ volts for crystals with no optical activity. The difference between this value and that obtained experimentally for BSO gives the amount of additional phase delay needed to compensate for optical activity (spatial dispersion). The experimental results indicate that EO birefringence disrupts the pure circular polarization eigenmodes of the crystal for the equivalent of half the crystal length. Section 4.1.4 gave that the rotary power of BSO is 21°/mm, so a 6.24-mm long crystal has 131° polarization rotation. The difference between the circular and linear

125
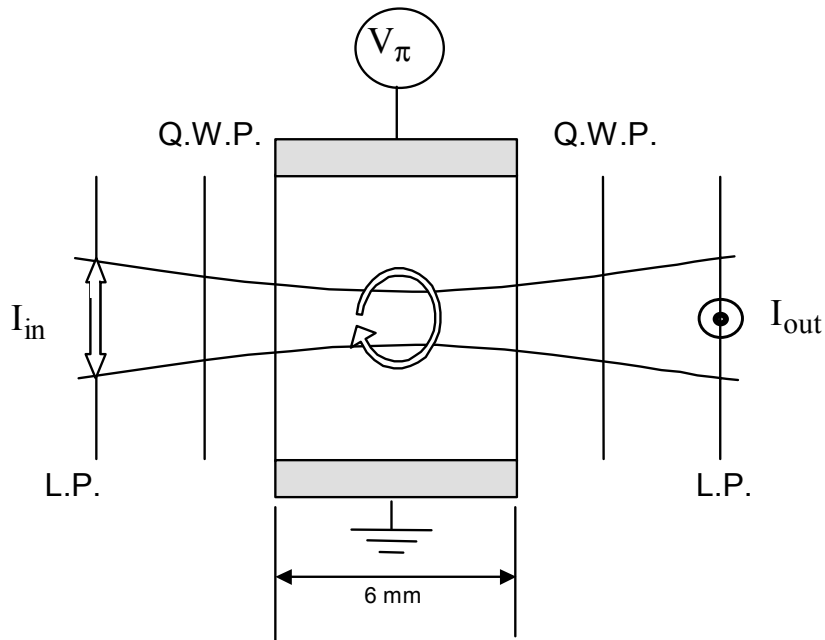
Figure 5-16 Quarter-wave plates used to launch circular polarization into crystal.

polarization half-wave voltage values obtained experimentally is 1050 volts, and

inserting this difference into Equation (4-7) gives a phase difference of $\delta = 132°$, which

amounts to a linear polarization rotation, $\delta/2 = 66°$, or half the optical birefringence. This

is an intuitive result. The difference between the experimental value for the spatially

dispersive crystal and the predicted value for nonspatially dispersive crystals is $\delta = 104°$,

which is not an expected result. In the experiments, the polarization extinction ratio for

linear polarization was −39 dB (includes $\approx$ -11 dB degradation due to BSO), while the

polarization extinction ratio obtained using quarter waveplates was degraded to −16.5 dB.

The quality of the quarter-wave plates used in the experiment was not known. Linear

polarization was used for the experiments that follow, because of the better extinction

ratio.
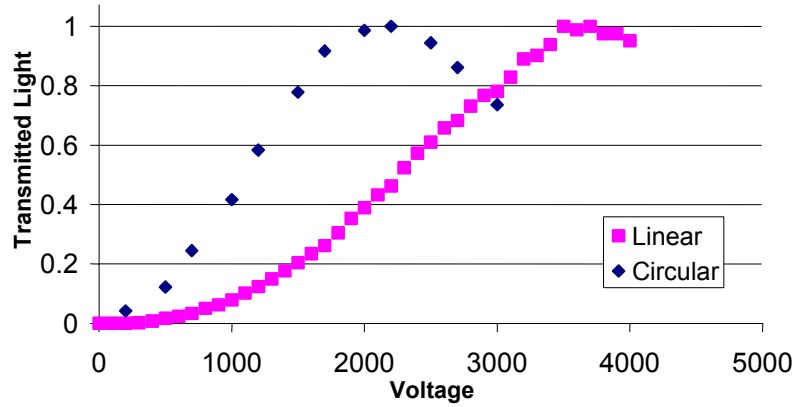
Figure 5-17 Voltage versus transmitted optical intensity through crossed polarizers for linear and circular polarization in BSO. Peak is half-wave voltage.

The linear relationship of photoconductivity to optical power obtained experimentally for our BSO crystal is shown in Figure 5-18. A log plot is used to display the optical power that varied between 10 μW/cm^2 and 2.5 mW/cm^2. The current across the crystal was measured at three voltage levels: 500, 1000, and 3000 volts (indicated by color), and 13 levels of optical power were used to obtain the photoconductivity plot. The variability seen in the data is probably due to the course alignment of the variable beam splitter that was used to vary the input power.

The coefficient of photoconductivity B is obtained from the slope of the line $\sigma/I =$ B = 1.94*10^{-8} [ohms-watts-cm]$^{-1}$. The optical wavelength used was 632.8 nanometers. BSO has a very low dark conductivity, $\sigma_d=10^{-15}/\Omega$-cm, which corresponds to a dark illumination of 5×10^{-8}.
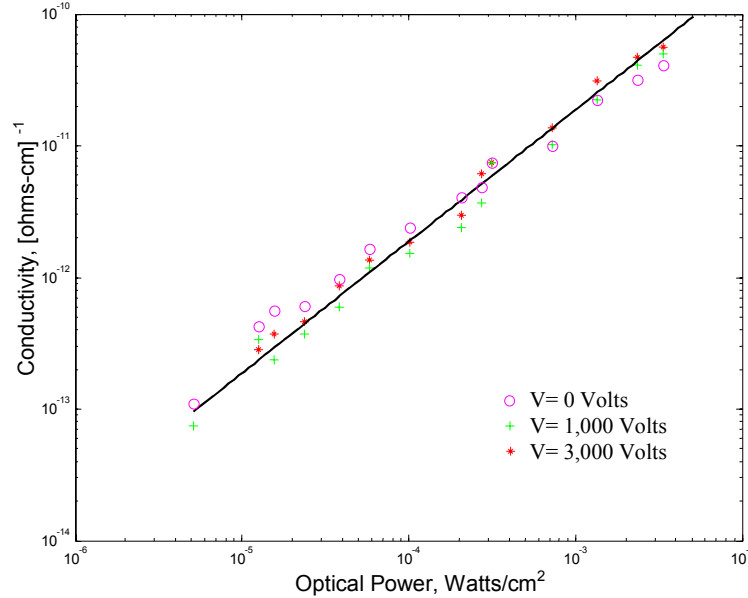
Figure 5-18 Measured photoconductivity for BSO crystal for various applied optical power (x-axis) and applied voltage.

Over the course of many hours of high-voltage operation, the performance of the BSO crystal degraded, and it was observed that the crystal had been damaged due to dielectric breakdown of the crystal itself or the air surrounding it. The damaged crystal is shown in Figure 5-19. A rule of thumb for maximum power dissipation for the crystal is to stay under one watt, so ½ watt power dissipation is chosen as a working limit. Large DC bias voltages are needed for E-O modulators in order to obtain a half-wave modulation voltage, so it is important that the photoconductivity be examined and kept inbounds. A voltage of 3300 was needed in our experiment to obtain half-wave modulation. The total optical power incident on the crystal (assuming an available carrier concentration) can be easily calculated using Ohm's relation. Using 3100 Volts and ½ watt power, the maximum resistance is 19.22 mega-ohms. The maximum conductivity is obtained by taking the inverse resistance and dividing by L/A to obtain 2×10^{-8} [ohms-
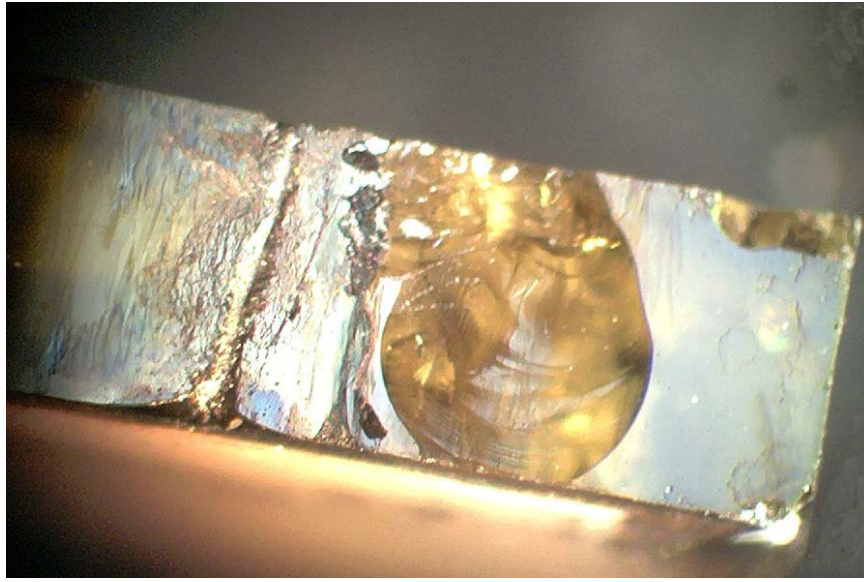
Figure 5-19 Damaged region of BSO crystal due to high-voltage dielectric breakdown.

cm]$^{-1}$. Using the result of our conductivity measurements, approximately $2*10^{-8}$ [ohms-watts-cm]$^{-1}$, the maximum optical power is limited to 1 W/cm^2 illumination across the entire crystal area. The illuminated area of our crystal is 0.23 cm^2. In order to achieve this conductivity, a majority carrier concentration of at least n=σ/(q μ) = $4.2\times10^{+9}$ cm^{-3} is needed, and this value is well below the majority carrier concentration of BSO.

5.2.2 EOPL Notch Depth Using BSO

An indication of notch depth for BSO optical power limiting was obtained by measuring the optical output while sweeping the optical input intensity to the crystal. The time between each sample of a sweep was one second. The optical power incident on the BSO crystal was controlled by RF power to the Bragg cell.   The tests were automated using GPIB and Daisy Lab software. The responsivity of the high-speed PiN diode detector

used to detect the output power was measured to be approximately 50% μamps/μwatt.

Generally for the data that follows, input optical intensity is taken as relative to the RF

power applied to the Bragg cell. It was calibrated to be approximately 8×10^{-7} W/cm^2 at -

40 dBm power into the Bragg cell. The optical power limiting threshold for BSO EOPL

in the dark was found to agree well with dark-intensity values reported in the literature

for BSO, 5×10^{-8} W/cm^2. The data presented may have some inconsistencies because

when the optical power levels increased and optical biasing was used, a 40-dB amplifier

was added to the system, and this gain may not have been added to the relative intensity

in all the plots that follow. Hopefully, this should not cause too much of a problem for

the reader.

Figure 5-20 shows a comparison of experimental data for EOPL transmission

over a 47-dB range, and the EOPL transmission model of Equation (4-21). Each point

on the plot was measured separately as the power to the Bragg cell was ramped up a step

at a time over the 47-dB range. The dwell time for each step was about 3 seconds

because this value was long enough to allow sufficient charge to accumulate. The input

power was amplitude modulated at 2KHz, and the output was detected with a lock-in

amplifier. The calculated plot had a best fit using a dark photoconductivity and

coefficient of photoconductivity parameter obtained experimentally. The differences

most likely took into account a "not quite fully dark" laboratory and reflections and

absorption in the BSO crystal. The parameters used were d_r =0.125 cm, D = 0.23 cm, B

= 2×10^{-8}, ($\sigma_{dark} + \sigma_{ambient}$) = 7×10^{-14}, and ξ_p = -25 dB. The value for ξ_p includes the

degradation of the polarizer extinction ratio due to the BSO crystal. Imperfections in the
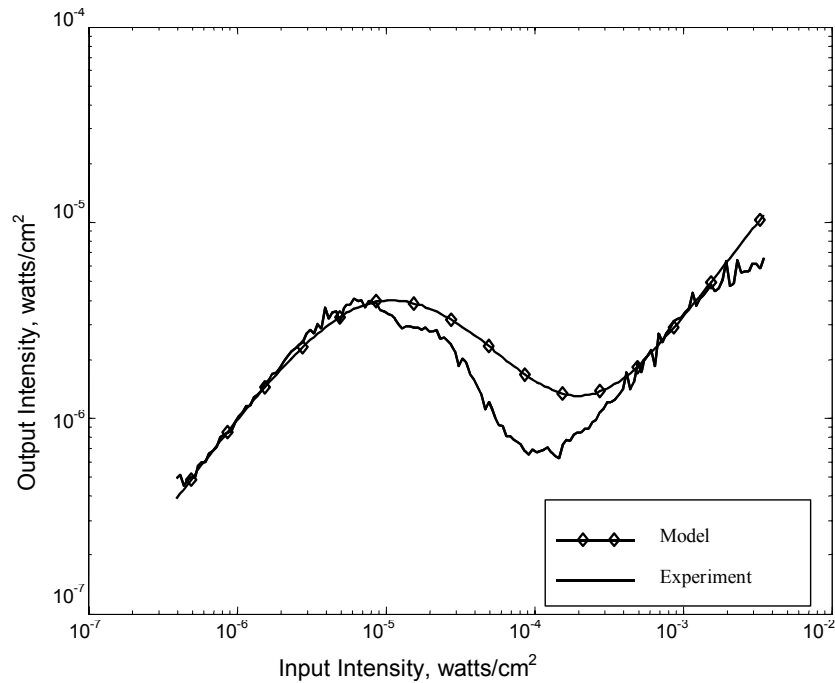
Figure 5-20 EOPL transmission plot for experimental data and results of numeric model.

BSO as well as damage over the course of these experiments limited the extinction ratio

to anywhere from 25-40 dB. Optimizing the extinction ratio by moving the active region

for each set of measurements taken was sometimes done, sometimes not. A typical

extinction ratio for birefringent polarizers is 60 dB; however, we achieved only 50 dB

extinction ratio using a sheet polarizer for the analyzer. A sheet polarizer was used for

convenience because a birefringent polarizer shifts the output beam when rotated and

would require realigning the detector each time the polarization was changed.

Unfortunately, measurements were never repeated using a birefringent analyzer;

however, it was noted that when the half-wave voltage is completely shielded, the input

beam can be attenuated by the value ξ_p. Since the reference beam was never passed

131
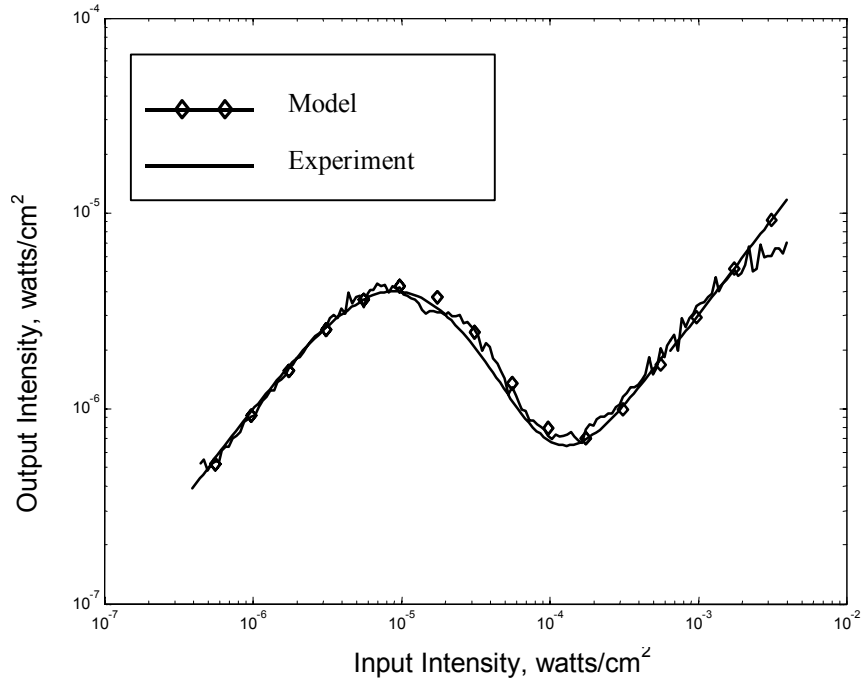
Figure 5-21 EOPL transmission plot and modified model.

through the crystal with the signal beam, doubling of the notch filter function, as

described in Section 3.2.3.1, was never observed. Figure 5-21shows an attempt at a

better fit to the experimental data by modifying Equation (4-21) to a sine cubed

relationship, $\sin^3(\Gamma/2)$ plus a slight increase in ambient dark conductivity $\sigma_{\mathrm{ambient}}$.

Figure 5-22 illustrates how the application of a uniform optical bias is used to

increase the optical power limiting threshold from the ambient, dark-intensity value, $I_d =$

5×10^{-8} W/cm^2. The optical bias was accounted for in the models [Equations (4-21) & (

4-35)] by adding an optical-control term to the dark conductivity, $\sigma_c = [\sigma_{\mathrm{dark}} + (\mathrm{B} \times I_c)]$

and the dark intensity $I_c = (I_{\mathrm{dark}} + I_{\mathrm{control}})$. The measurement of EOPL transmission versus

optical-signal input power was repeated using a range of uniform optical bias for each

input power sweep. The bias was applied using a separate laser delivered to the crystal face by fiber optic. A circular, variable, neutral-density filter was placed between the fiber coupler and the laser, so the uniform bias power is a logarithmic function of the angle marked on the circular filter (0-360°).

Note in Figure 5-22 that the optical bias in series 3 is higher than in series 2, but the power limiting appears to be reduced. This is most likely a memory anomaly due to trapped charge density that can have a long lifetime. In general, power limiting was not as well behaved as Figure 5-20 and Figure 5-22 may indicate, and a means to control any memory effects is needed. For example, alternating external voltage has been used to clear trapped charge, but not at the high-voltage values required for achieving half-wave E-O amplitude modulation. Such a large alternating voltage was not possible with our system. A time-integrating effect was observed by varying the time between each sample
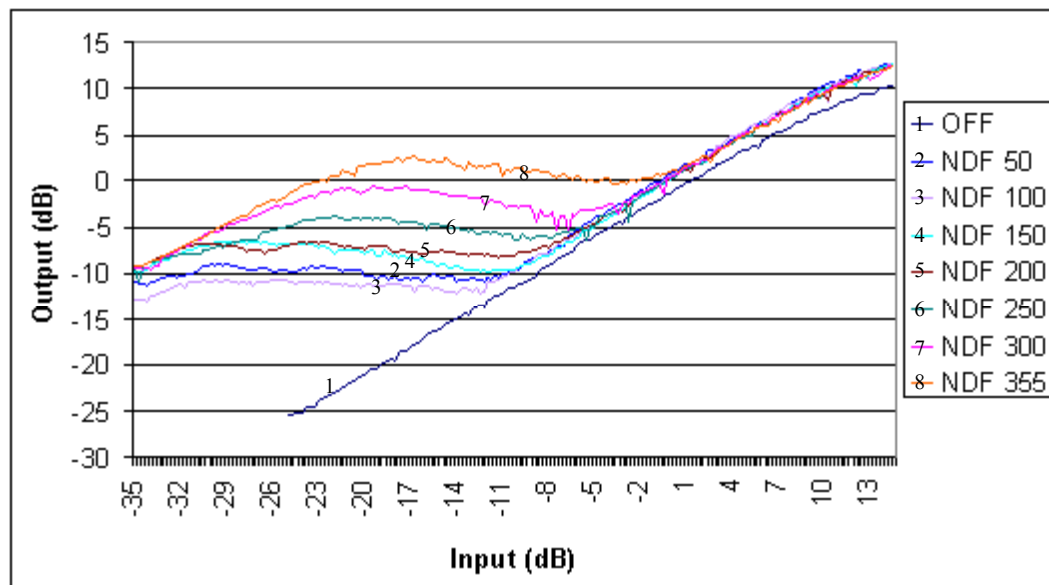
Figure 5-22 EOPL transmission for various optical bias.

of the intensity sweeps from 0.5 seconds to 16 seconds for each sweep (normally 1-3-second interval between samples). The results are plotted in Figure 5-23, which shows that longer dwell times result in deeper optical attenuation. A 10-dB difference between the 1-second and 16-second intervals between intensity samples was observed. These results may not conflict with the dynamic response reported by Guo *et al* [44], which was 25 to 2.15 msec depending on light intensity of 0.3 to 2.15 mW/cm^2, respectively. This result shows that the attenuation response slowly deepens over time, and this could have been related to other unknown factors, such as the 2KHz amplitude modulation used to detect the low-intensity beams. The numerical analysis in section 4.3.2.3 indicates that a large concentration of positive charge must build up near the dark region. Equation (4-22) gives the generation rate for dark current [s$\beta \times$ (Nd-N$_d^+$)] C/cm^3-sec, and Figure 4-12(c) shows peak positive-charge density at the illumination dark edge $\approx 6 \times 10^{-6}$ C/cm^3
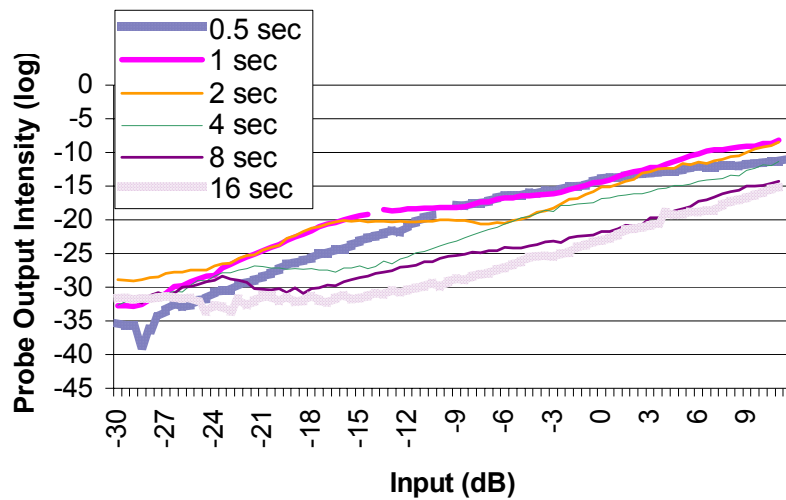
Figure 5-23 EOPL transmission for various integration times.

at 10^4 W/cm^2. Dividing the peak value by the dark generation rate gives a value between

6 and 0.006 msec depending on the ionized donors value N_d^+ 0-10^3, respectively. The

experimental results generally showed a slow attenuation rate, on the order of seconds, to

reach a steady state value.

Figure 5-24 shows a plot of EOPL output as a function of time for four different

optical bias intensities (0°, 30°, 60°, 90° is decreasing light bias intensity). The data was

obtained by opening a shutter and collecting readings of the output intensity at 0.1-second

intervals over a 10-second period. No change in time response is apparent for the

different optical bias intensities.

Figure 5-25 illustrates the linear relationship between power limiting and

photocurrent versus the applied optical bias. The optical bias is plotted in the figure as a

function of neutral-density filter position. As the optical bias increases, the photocurrent
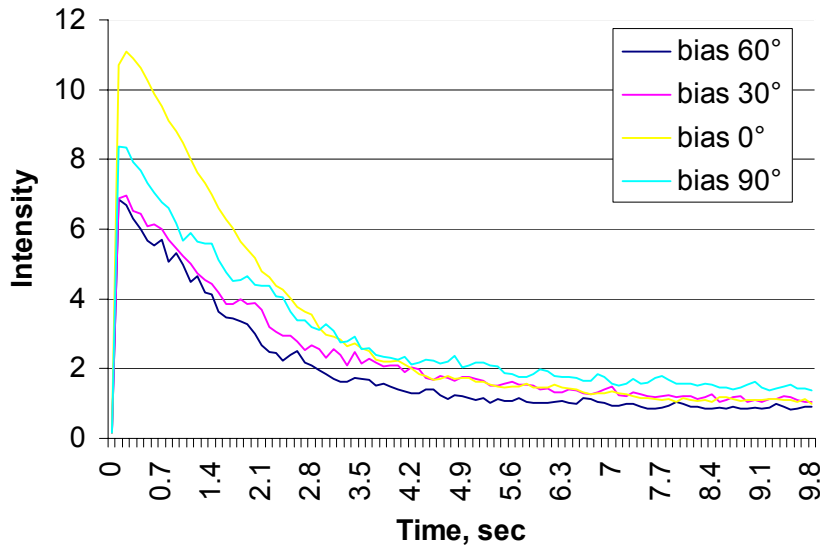
Figure 5-24 EOPL time response for four different optical bias intensities.

and optical transmission increases; that is, there is less attenuation of the input signal by field-shielding. The signal continues to increase (less attenuation) until its maximum intensity passes through the EOPL.
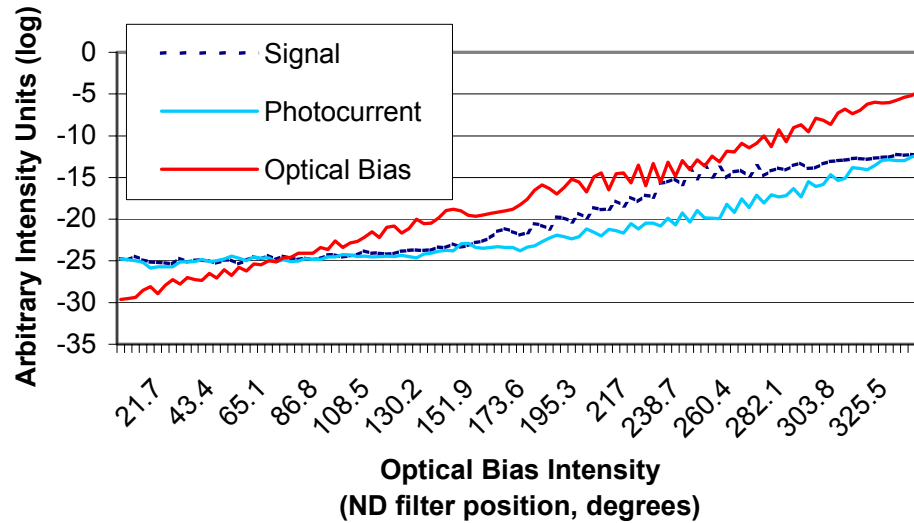
Figure 5-25 EOPL photocurrent and power limiting versus optical bias.

Figure 5-26 illustrates the role that an optical bias plays in erasing the memory effect. A small signal is monitored for its transmission through the EOPL. A high-intensity interference component is applied and ramped up and back down in intensity four times. The interference component creates space-charge field shielding that attenuates the signal beam. With no optical bias, as the high-intensity component illuminating the crystal is removed, the small signal is not restored. If an optical bias is present, the signal beam is restored as the high-intensity interference component is removed.
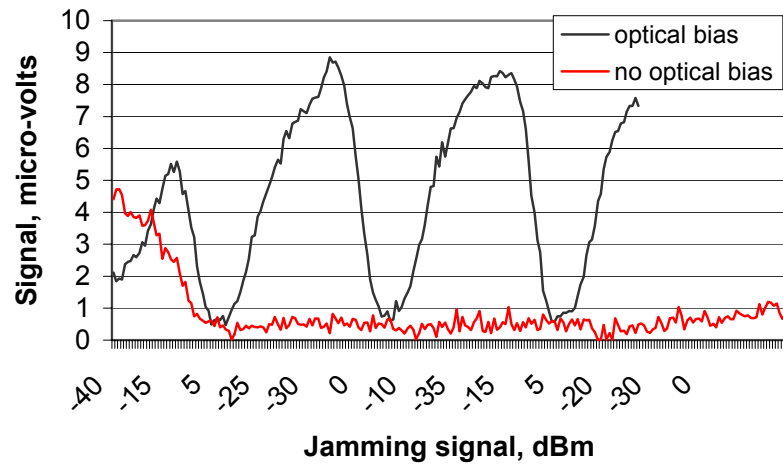
Figure 5-26 Optical bias used to clear trapped space charge memory.

Figure 5-27 shows the temporal response for removal of trapped space-charge field by application of an optical bias. The intensity of the optical input is constant. As optical bias is increased, attenuation of the input beam is reduced. The optical bias is
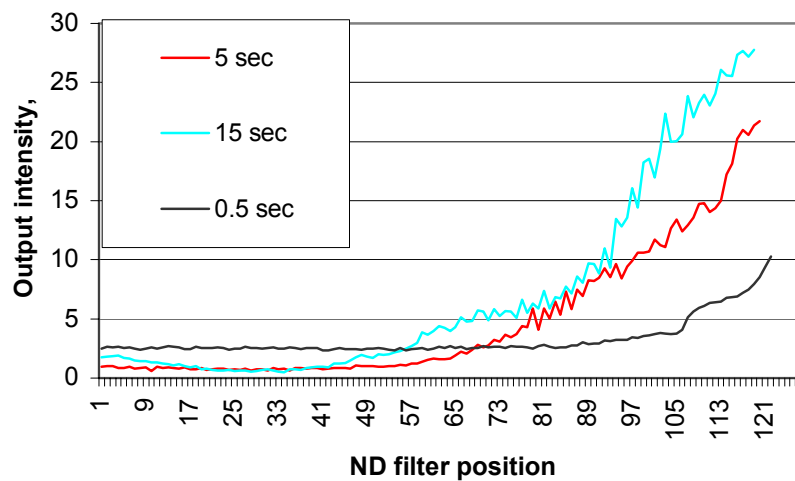
Figure 5-27 Time response of optical bias charge clearing.

increased at a rate given in the legend for each series. The number of samples taken per series was 127.

5.2.3 EOPL Notch Width

A direct measurement of the notch depth and width of the EOPL in response to a narrowband RF interference component can be done by examining the system output spectrum for a wideband input signal. As explained earlier, indirect measurement of notch depth and width are made for this research because of noise and poor wideband heterodyne detection in our system. To simulate a wideband signal and narrow-band RF interference, the intensity of a small signal probe beam was monitored and plotted as a higher-intensity beam (or interference, as in RF interference, not optical phase interference) was swept across its position in the Fourier transform plane, located at the EOPL crystal. It is believed that this arrangement is completely analogous to a direct measurement of the system response as described in Section 3.2.3.1, Notch-Filter Function, page 56. Two different detection methods were used: (1) amplitude modulation and lock-in amplifier detection, and (2) fiber-coupling and heterodyne detection.

The uniformity of the BSO crystal was determined by using the Bragg cell to sweep a beam across the crystal face and measuring the output intensity. Figure 5-28 shows the two scans made. The active BSO had a half-wave voltage applied and 90° polarization rotation, and a control had no voltage applied and the polarizer was rotated to pass the beam. Variability in the central region (15 MHz) stayed within 1.8 dB.
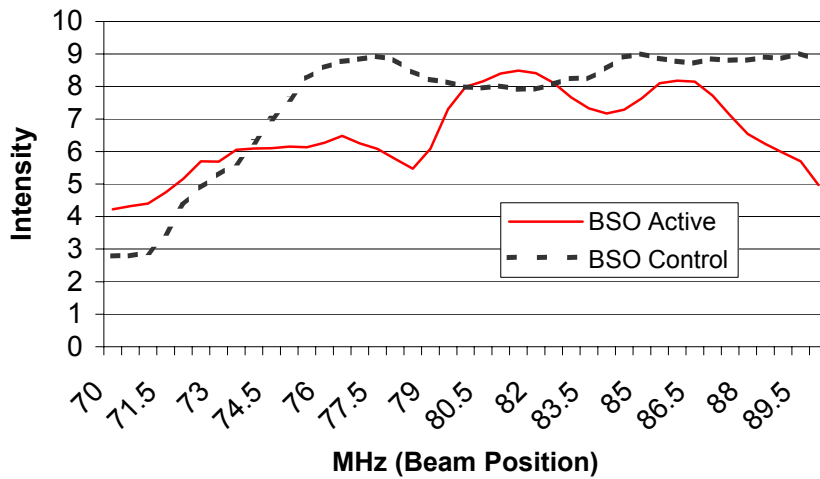
Figure 5-28 EOPL uniformity scan using Bragg cell RF sweep.

Figure 5-29 shows a series of notch-width measurements for various interference component intensities: 5, 15, 25, and 35 dB are applied. A subtle point with regard to these plots is that attenuation of the interfering beam is not measured directly; rather, the effect that adaptive attenuation has on the probe beam (desired signal) intensity is measured. The sample increment for each step of the interference beam sweep is 3.125 microns, which was generated by 250-KHz increments applied to the Bragg cell with $f_0 =$ 100MHz. The figure shows both the experimental and numerical results, as described in Section 4.3.2, Steady-State Solutions for Kukhtarev's Band-Transport Equations, page 87. The probe beam intensity was slightly less than the applied uniform optical control light, $I_c = 10^{-2}$ W/cm^2, that was needed to increase the dark-threshold intensity because optical power was concentrated by the Fourier transform lens. The probe beam was amplitude modulated and detected using a PiN diode and lock-in amplifier as shown in
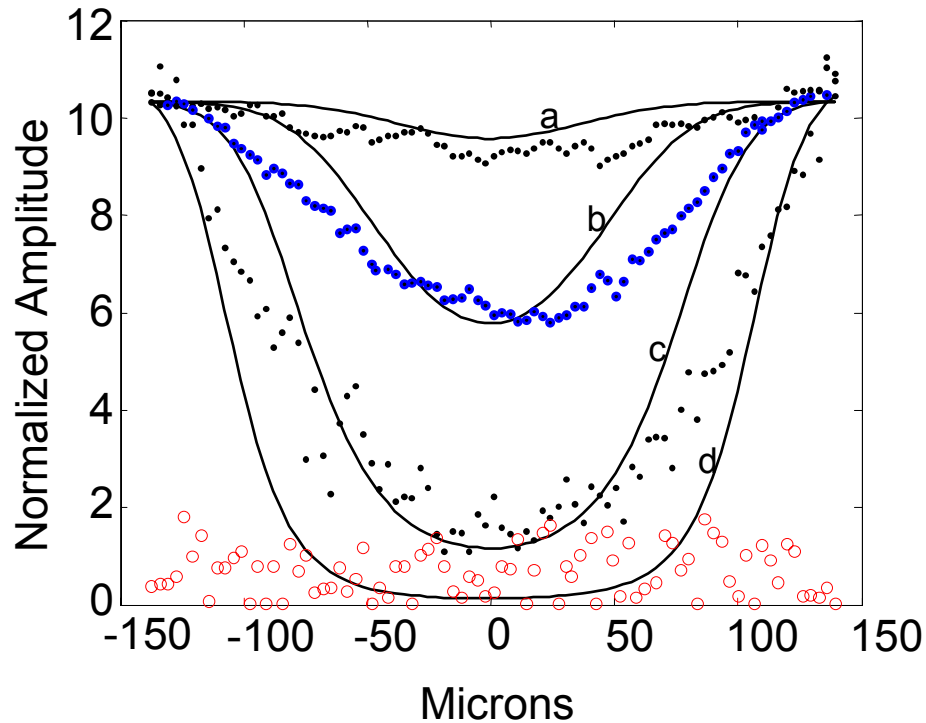
Figure 5-29 Experimental results for BSO notch width. $I_c = 10^{-2}$ W/cm^2 uniform optical bias. Optical interference beam intensity relative to bias is a) 5, b)15, c) 25, and d) 35 dB. Numeric results are shown with solid lines.

Figure 5-13. Useful interference reduction was indicated by noting that without the

EOPL in the system, detection of the probe signal was overwhelmed for series b, c, and d.

The 300-micron sample region corresponds to a 20 MHz RF bandwidth. The resolvable

spot size was slightly less than 100 microns because the aperture had been reduced in an

effort to obtain functional power levels in the power limiter.

The spot size needed to fit the numerical calculations with the experimental data

was much larger than the expected value, that is, the signal spot size convolved with the

interference spot size, multiplied by the aperture sinc function. This discrepancy revealed

problems with matching the E-O modulator interaction length with the depth of focus for

the focused beam. The first series of notch-width measurements was made using a 10-cm *f* lens. Calculations of beam width over a 6.0-mm region centering the focal plane are given in Figure 5-30 for refractive index of air and BSO and two different lenses used in the experiments. It is apparent that for the 10-cm *f* lens, slight misalignment of the crystal along the optic axis will dramatically change the average beam size propagated through the modulator. Thus for a 10-cm *f* lens, the beam size in the EOPL crystal is difficult to determine, and if the crystal is perfectly centered in the Fourier transform plane, the average beam size will be 3 to 4 times the minimum resolvable spot size.
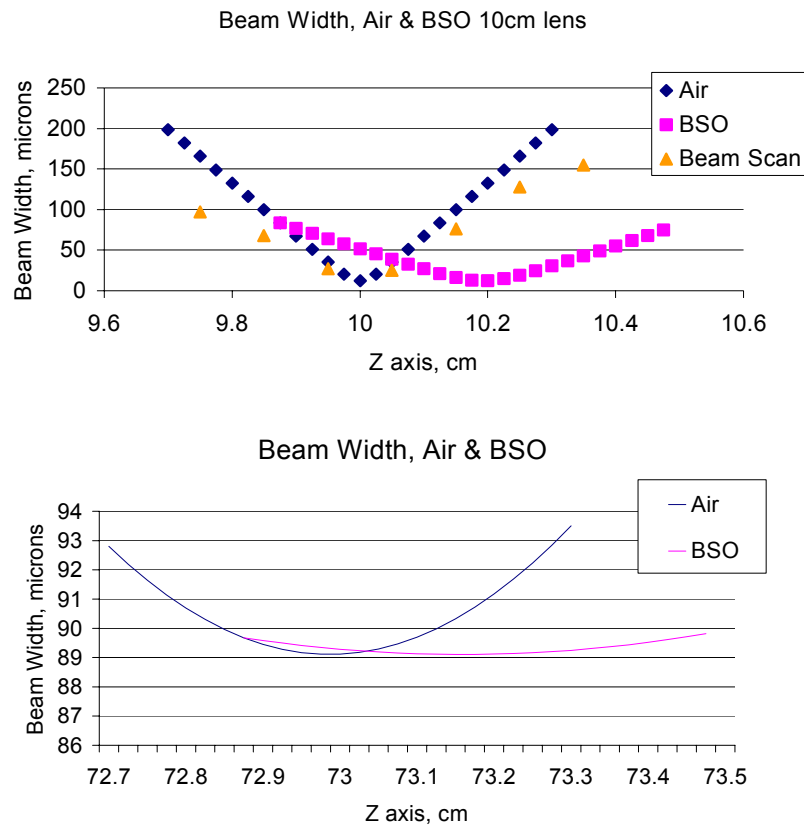
Figure 5-30 Depth-of-focus calculations for 10-cm and 73-cm focal length lens. Note experimental results (for air) using beam scanner are indicated in upper plot.

Initially a short focal length was chosen to minimize the overall system size. The

initial plan at the outset of this research was that a portable system could be used in a

wideband communications test laboratory available in our organization. This was also

the reason the (what turned out to be) inadequate heterodyne mounts were used, as they

were part of a portable optics table that was available. The 10-cm f lens was replaced

with a 73-cm f lens which gave a uniform beam over the interaction length of the crystal,

as can be seen in the lower plot of Figure 5-30.

The remaining series of notch-width measurements were performed using the 73-

cm f lens. Two of these measurements used amplitude modulation and lock-in amplifier;

the other used heterodyne detection. The beam spot size for these notch-width

measurements was measured in air using the beam scanner located at the lens focal plane.

The beam scan indicated that the beam width varied little over the 6-millimeter
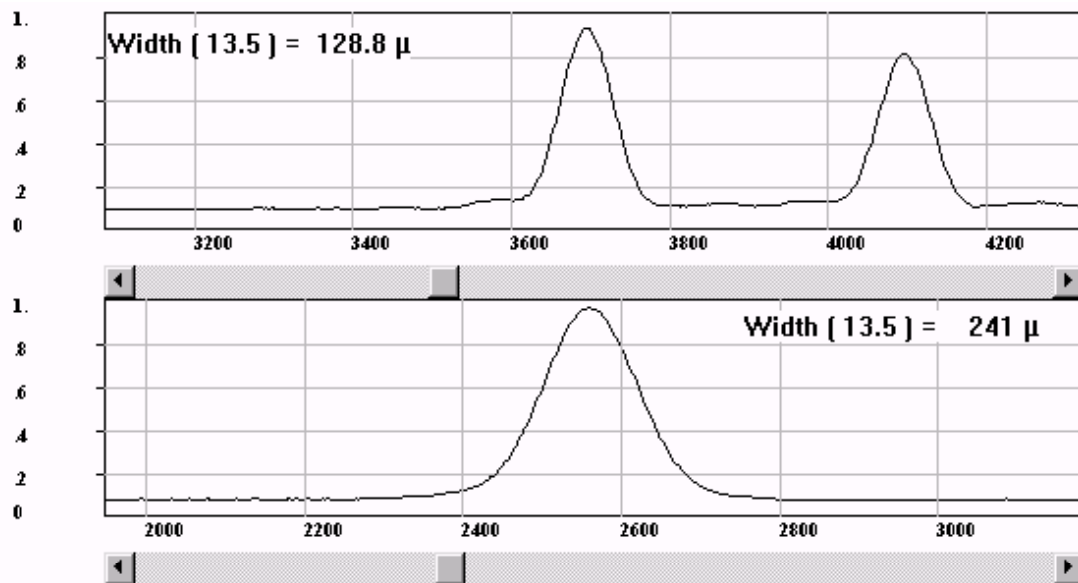
**Figure 5-31 Beam scan at Fourier transform plane for 73-cm focal length lens.
Beam width is 128.8 × 241 microns.**

interaction length of the crystal, and the 13.5% beam size was 129 microns along the x-axis and 241 microns along the y-axis. The results are shown in Figure 5-31.

Notch widths were again measured by tracking the intensity of a small signal probe generated at the Bragg cell by a –22 dBm RF signal. This probe power was just below the EOPL threshold. The results are shown in Figure 5-32. The RF interference beam drive voltage was varied between -15 dBm and 0dBm for each sweep across the probe. The RF interference beams have intensity 7, 12, 17, and 22 dB higher than the signal. By using Equation (4-41), the notch width of the space charge field generated by the RF interference beams can be calculated as follows: The threshold intensity is $I_c =$ -25 dB, and RF interference beams have intensity 10, 15, 20, and 25 dB greater intensity; that is, $I_0 = $ -15, -10, -5, and 0 dB. The Gaussian beam diameter is $W_0 = 64.4 \ \mu$m, so at the threshold intensity I_c, the beam width is $W_{dc} = $ 195, 240, 275, and 310 μm, respectively. Convolution of the signal and RF interference beams expands the resulting notch width to the sum of each beam (take the high intensity beam width as W_{dc}) so the calculated notch widths are approximately (195 + 129) = 324, (240 + 129) = 369, (276 + 129) = 405, and (310 + 129) = 439 μm, respectively. The x-axis scale in the plot is approximately 1MHz = 100 μm. Measuring from the plot, the 13.5% notch widths are approximately 300, 600, 800, and 900 microns. The percent difference between the experimental and calculated (calculated:experimental) notch widths are 324:300 = -8% for 10 dB intensity difference, 369:600 = 39% for 15 dB, 404:800 = 50% for 20 dB, and 439:900 = 51% for 25 dB. Table 5-3 lists the data for all the notch-width measurements using the 73-cm f lens.
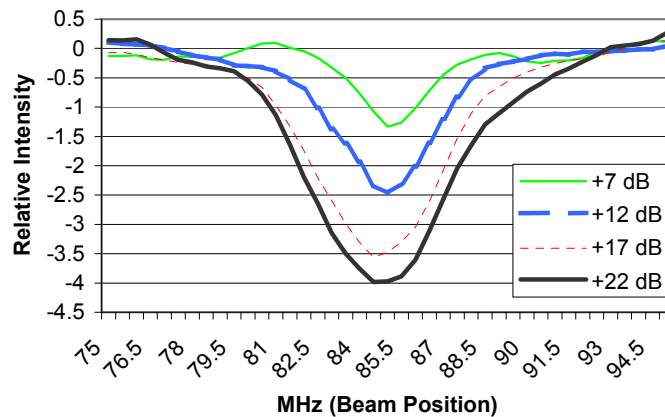
Figure 5-32 EOPL notch width for 73-cm lens, 128-micron spot size beams, and Δ1.0 MHz RF is deflected 100 microns.

The next set of notch-width measurements used fiber-optic coupling, but the signal was amplitude detected in the same manner as the previous series of measurements. This data is presented to supplement the amplitude detection results and was collected in response to a problem that occurred with the first set of fiber-optic coupling heterodyne detection measurements. Amplitude oscillations, later found to be a result of back coupling of the reference beam into the BSO, had rendered useless the first series of heterodyne detection data. This problem was corrected by reducing the reference beam intensity.

Figure 5-33 shows the plot of EOPL notch-width sweeps that used amplitude detection and fiber-optic coupling. Attenuation of the probe signal was slightly more pronounced, but the results were similar. The signal probe was generated by a –29 dBm RF signal. The –20-dBm RF interference signal did not attenuate the probe, so the baseline threshold (dark intensity) is taken to be –20 dBm. Expected notch widths were

144
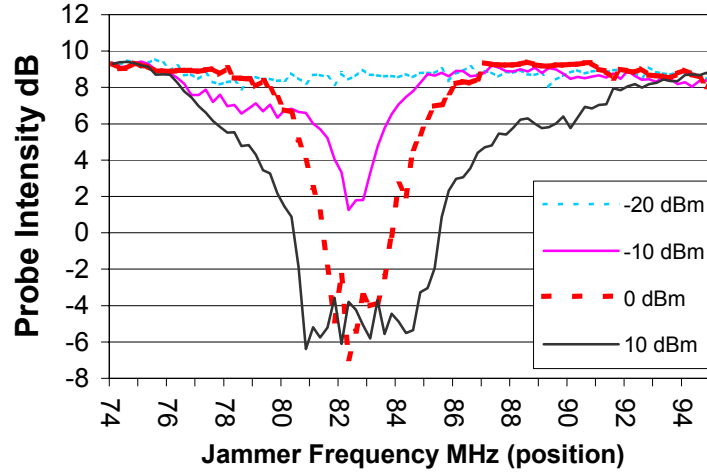
Figure 5-33 EOPL notch width using fiber amplitude detection. -29 dBm small signal probe, RF interference intensity as indicated.

again calculated using Equation (4-41) for I_0 = 10 dB, 20 dB, and 30 dB; I_b = 0 dB; and

$2W_0$ = 129 μm, W_{dc} = 165, 233, and 285 respectively. The percent difference between

the calculated (W_{dc} jam + W_0 probe) and experimental (approximate from plot) notch

widths are (calculated:experimental) 300:400 = 25% for 10 dB intensity difference,

362:500 = 27% for 20 dB, and 414:1000 = 58% for 30 dB.

Figure 5-34 shows notch-width measurements that used heterodyne detection of a

probe signal generated by a –15-dBm RF voltage applied to the Bragg cell. Again, as

with all the heterodyne detection signals, the laser noise was large, so in order to show

the detail, the upper and lower sweeps are offset by ±10 dB respectively from the center

sweep. That is, the plots all had the same initial intensity of around –117 dBm. Also, a

baseline average power level was added to each plot in order to help show the start of

power limiting. That is, the horizontal lines are averages for the regions where no

interaction occurred. The small arrow at the bottom of the scale marks the frequency of

145
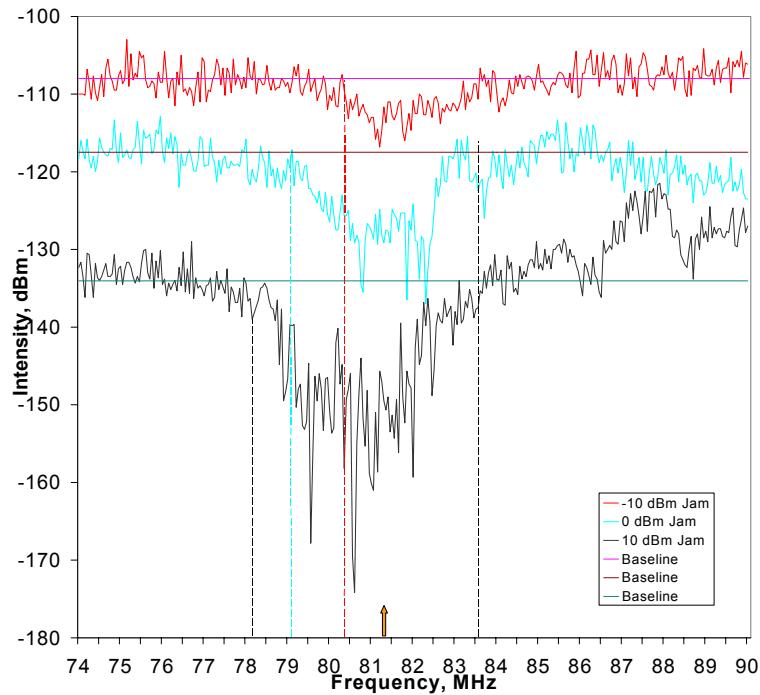
Figure 5-34 EOPL notch-width measurement using heterodyne detection.

the probe signal. Also, vertical lines were added to mark the frequencies that appear to

delineate the notch width. The approximate 13.5% notch widths taken from the plot are

-10-dB RF interference = 3.25 MHz (325 μm), 0-dB RF interference = 4.0 MHz (400

μm), and +10-dB RF interference = 5.25 MHz (525 μm). Note that the right hand side

appears to have one notch delineation point for each of the three scans, while the left-

hand side notch delineation point shifts as the beam intensity increases. This result was

not seen in the amplitude measurements, most likely because they were less precise, as

can be seen from Table 5-3. Comparing all the expected and measured values for notch

widths showed variability from 10% to 50%, but this variability seemed to be confined to

146

the amplitude detection schemes, while the heterodyne detection scheme had very consistent results.

Table 5-3 EOPL notch width measurements and calculations

Detection	Decibel Jam Power	5 dB	10 dB	15 dB	20 dB	25 dB	30 dB
Amplitude	Calculated Width, μm	267	324	368	404		
	Measured Width, μm	300	600	800	900		
	Percent Difference	11%	46%	54%	55%		
Amplitude (Fiber Optic)	Calculated Width, μm		324		404		467
	Measured Width, μm		400		500		1000
	Percent Difference		19%		19%		53%
Heterodyne (Fiber Optic)	Calculated Width, μm	267		368		438	
	Measured Width, μm	325		450		525	
	Percent Difference	18%		18%		17%	

5.3 Experimental Recommendations

RF noise from the RF generators and amplifiers used to drive the Bragg cell created problems in the lab for heterodyne-detected signals. In addition, recovered baseband signals included a lot of noise generated by the system. A careful consideration of how to avoid this source noise is necessary. Of course, this is exactly the reason an interference-reduction system is needed outside the lab where cluttered RF environments also exist.

The fiber-coupling approach was useful for obtaining measurements on the EOPL as a last resort, but this approach was only used because the mirror and beam splitter mounts lacked good micro-positioning features, and heterodyne detection was never optimized because of an oversight (a flat-top optical illumination profile was sought, but never obtained). Future experiments should make careful consideration for optimizing heterodyne detection, such as outlined in reference [29], and a collinear process should be considered.

Optimum notch depth is achieved by maintaining the highest quality of polarization extinction. The quality of the power-limiting crystal is most important, as nonuniformity in the BSO was the biggest degrading factor for the polarization extinction ratio. Also, the high half-wave voltage for BSO eventually degraded the crystal. Quarter-wave plates can reduce this voltage, but they might also factor into polarization extinction ratio degradation.

Chapter 6

Conclusions and Recommendations

6.1 Conclusions

The experimental results for the photorefractive, EOPL adaptive notch-filter depth and width showed good agreement with solutions of the steady-state numerical models. The notch-filter width was seen to grow to three to four times the Rayleigh resolution criteria for interference that was 40 dB greater than the desired signal intensity. In this regard, it is apparent that the trade-off between notch-filter width and depth that Erickson describes, ref [32], is simply a statement of the discrepancy for the Rayleigh resolution criteria when comparing high-intensity interference (+40dB) spot sizes to low-intensity signal spot sizes in the frequency plane, as is shown in Figure 2-6. Therefore, the optical power limiter can adaptively create a notch-filter function with ideal width and depth needed to reject RF interference. The aforementioned expansion of the spot size by three to four times should be considered when designing the time-bandwidth product for the system.

With regard to system size and the Fourier transform lens, a long focal length is needed to maintain a long depth of focus through the interaction length of the EOPL, which required spot sizes on the order of 40 microns. There is much less restriction on

the minimum spot size with respect to charge confinement and photorefractive field-shielding, which can maintain notch widths to a few microns in size. Decreasing the Fourier transform lens focal length results in decreased spot size resolution at the excision plane, but again this requires increasing the time-bandwidth product. Approaches for mitigating the long depth of focus are discussed in the next section.

The crystal appeared to have response-time limitations. The models used in this analysis dealt with steady-state conditions, and this research did not attempt to verify experimentally the dynamic response for BSO reported in the literature. However, the experiments showed that reaching a steady-state value for optical attenuation could take up to a few seconds. Memory effects did not seem to be a factor if a uniform control beam is used.

Finally, AOA resolution was shown to be a function of the number of antenna elements, N, but the $4/\Delta t$ notch-filter width needed to reject +40-dB RF interference washes out the capability of broadband RF interference rejection based on just a few channels of AOA.

6.2 Recommendations for Future Work

Many system improvements are required before the potential of this A-O-based frequency plane filter is realized. Unfortunately, the limited resources available for this research effort allowed investigation of only a small portion of the required effort. The following subsections list a few topics that were considered for this research, but could not be fully developed.

6.2.1 Collinear-Beam Architecture

The importance of reducing system-generated noise was an obvious result of the experiments. Collinear-beam, Mach-Zehnder designs reduce phase noise and allow use of lasers with short coherence lengths.[55,56,57] A collinear-beam design that might improve upon the one illustrated in Figure 3-14,[32] could be achieved by modifications such as those illustrated in Figure 6-1. This approach avoids using the undiffracted beam as a reference. A Fresnel lens is used as a beam splitter but produces two different types of beams: (1) a collimated signal beam that illuminates the full aperture of the Bragg cell and (2) a reference beam deflected at an angle equal to the center frequency, f_0 of the Bragg cell and focused between two separate Bragg-cell channels so that the reference beam does not interact with the sound waves. The second lens, a Fourier transform HOE, reverses the roles of the two beams at the Fourier transform plane. The reference beam uniformly illuminates the EOPL, while the signal beams are focused at the EOPL. Heterodyne detection might be achieved immediately behind the EOPL, as shown, or optimized in some other fashion using additional lenses.
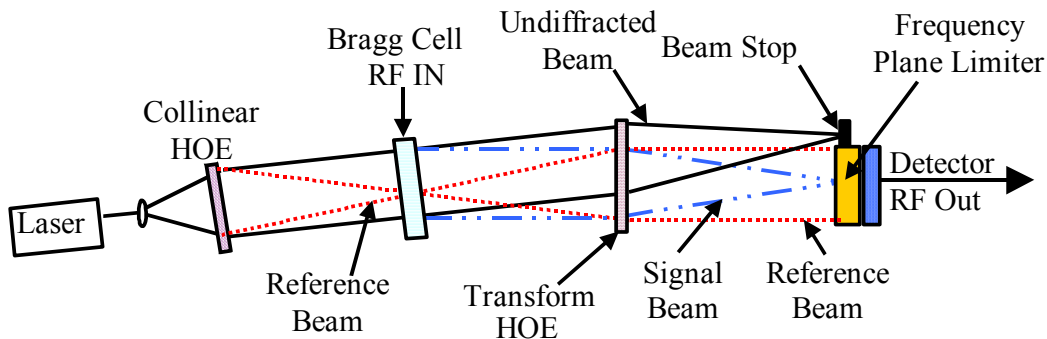
Figure 6-1 Collinear design for multi-channel Bragg cell.

Gray-scale manufacturing techniques have reduced higher-order diffraction of light for Fresnel lenses, or HOEs; and high-efficiency, dual-focus lenses are now available.[58] In addition to the two-beam lens, an HOE Fourier transform lens might be designed to minimize the power lost to higher-order diffraction due to the multiple Bragg-cell channels. Historically, the analysis of multi-channel, Bragg-cell beam forming processors has been for radar signal processing or beam finding. The applicability to more complex receiver arrangements, such as those required for GPS, could be investigated. For example, an HOE Fourier transform lens may also be applied to allow multi-channel Bragg-cell processing on other types of phased array antennas, rather than just linear placement of elements, and may improve the coverage needed for receiving signals from multiple satellites. In addition, perhaps methods could be examined for keeping the number of antenna-array elements to a minimum while increasing the separation between AOA spots in the Fourier transform plane, for example, using redundancy at the Bragg cell.

6.2.2 Waveguiding in Photorefractive Crystals

Obviously, system size is a factor that must be considered for any practical system application.[59] Originally the experimental system used in this research was designed for portability to other laboratories, and a 1.0×0.5-meter optics bench was envisioned. However, a 1.0-meter f lens was eventually used to achieve the 6-millimeter depth-of-focus requirement for the adaptive power limiter, and this ideas was abandoned. The depth-of-focus limitation was determined to be more restrictive than the inherent resolution capability of the adaptive power limiter. A long depth of focus is needed in a

bulk photorefractive power limiter unless an overlap of the resolvable spots at the Fourier transform plane can be tolerated by the overall system resolution. Other approaches are self-focusing of the beam and beam confinement in the crystal by coupling the light into waveguides. Waveguiding due to photorefractive effects has been demonstrated in crystals with external electric fields applied.[52] These self-focusing effects might be optimized for the notch-filter application. In addition the use of stacked waveguides, or fiber-optic bundles that also limit optical power intensity, could be considered.

6.2.3 System Insertion Point

The center frequency and bandwidth of Bragg cells vary depending on a particular A-O crystal type and design. GPS satellites broadcast in a 1-2-GHz range, and a natural intermediate frequency for the GPS system is 173 MHz. This is a convenient Bragg-cell operating frequency, but further down converting of the carrier frequency may be desired in order to obtain optimum Bragg-cell performance. Any additional frequency conversion adds to the burden of inserting an acousto-optic RF interference reduction system into the communications receiver. The broadband receiver design should be examined to determine the optimum insertion point for an A-O-based system. Also, the Bragg-cell limitations with respect to signal levels and dynamic range are known and were not addressed here.

Appendix A

Useful Bragg Cell Formulae

This appendix summarizes convenient formulae for Bragg-cell systems that were referred to constantly while working in the lab. See the *List of Symbols* for identification of parameters.

Bragg angle:

$$\alpha = \frac{\lambda \cdot f_a}{\upsilon_a} = \frac{\lambda}{\Lambda} \qquad \{ \text{A-1} \}$$

The incident laser beam passing through a Bragg cell is deflected at an angle linearly proportional to the applied signal frequency. Higher orders are usually suppressed, for higher orders multiply the right-hand side by the order number.

Diffraction efficiency:

$$\eta = \sin^2 \left(\frac{\pi}{\lambda} \left(\frac{M_2 \, P_{ac} \, L}{2 H} \right)^{1/2} \right) \qquad \{ \text{A-2} \}$$

The light diffraction efficiency is proportional to acoustic power, material figure of merit, crystal geometry and is inversely proportional to the square of the wavelength λ.

Spot Position:

$$x = \alpha \cdot F = \frac{\lambda \cdot f_a}{v_a} F \qquad \{ \text{A-3} \}$$

The position of the focused spot in the Fourier transform plane is the deflection angle multiplied by the lens focal length.

Minimum resolvable deflection angle:

$$\Delta\theta_{min} = \frac{\lambda}{D} \qquad \{ \text{A-4} \}$$

Two wavefronts can be resolved if the tilt between them is one wavelength of light over the aperture diameter.

Minimum resolvable spatial frequency:

$$\Delta x_{min} = \frac{\lambda}{D} F \qquad \{ \text{A-5} \}$$

Two wavefronts focus with a distance between peaks of the minimum resolvable angle times the focal length.

Minimum resolvable acoustic frequency:

$$\Delta f_{a-min} = \frac{v_a}{D} \qquad \{ \text{A-6} \}$$

The minimum resolvable acoustic frequency is the lowest cycle that will span the aperture ($D = v_a / f_{a-min}$).

Total sweep angle:

$$\theta = \lambda \frac{B}{\upsilon_a} = \frac{\lambda}{\Lambda_B}$$

{ A-7 }

The Bragg cell has total angular sweep given by the optical wavelength over the acoustic

bandwidth wavelength.

Number of resolvable spots:

$$N = \frac{\theta}{\theta_{min}} = \frac{\theta D}{\lambda}$$

{ A-8 }

The number of resolvable spots is the total scan angle divided by the minimum resolvable

deflection angle.

Time bandwidth product:

$$N = B \Delta t$$

{ A-9 }

The acoustic bandwidth times the Bragg-cell time aperture gives the number of

resolvable spots.

Multi-channel maximum deflection angle:

$$\alpha_{max} = \frac{\lambda}{d}$$

{ A-10 }

The maximum diffraction angle for multi-channel device is the optical wavelength over

the channel-to-channel spacing.

Multi-channel minimum resolvable angle:

$$\alpha_{min} = \frac{\lambda}{n \cdot d}$$ 　　　　{ A-11 }

The minimum resolvable deflection angle for multi-channel device is the optical

wavelength over the width of all channels combined.

Multi-channel number of resolvable AOA:

$$N = \frac{\lambda}{d} \frac{n\,d}{\lambda} = n$$ 　　　　{ A-12 }

The number of resolvable angles of arrival is the maximum deflection angle divided by

the minimum resolvable angle.

Multi-channel phase difference between channels:

$$\phi = \frac{2\pi \cdot d_r}{\lambda_{RF}} \sin \theta_{AOA}$$ 　　　　{ A-13 }

The phase difference between channels is proportional to the AOA and the distance

between antenna receiver elements.

Multi-channel, y-axis spatial period:

$$\Lambda_y = \frac{2\pi \cdot d}{\phi} = \frac{d \cdot \lambda_{RF}}{d_r \cdot \sin \theta_{AOA}}$$ 　　　　{ A-14 }

The spatial period in the y-axis is inversely proportional to the phase difference between channels.

Multi-channel beam forming:

$$y = \frac{\lambda}{\Lambda_y} F = \lambda \cdot F \cdot \frac{d_r \cdot \sin\theta_{AOA}}{d \cdot \lambda_{RF}}$$ { A-15 }

The AOA deflection is the optical wavelength divided by the spatial period, times the focal length of the lens.

Appendix B

Matlab Code

B.1 Numerical Differential Equation Solver Collocation Method

This appendix describes the *Matlab* collocation program and code used to solve the state variables found in Equation (4-38). The Matlab reference file is the source used to write the code.

1. Rewrite the problem as a first-order system and code in Matlab: see for example

   function dydx = mat33g1code(x, y)

2. Code the Boundary Conditions Function: see for example function res = mat3gbbc

3. Create an initial guess: see for example function yinit = mat3binit(x,y)

4. Apply the BVP solver: sol=bvp4c(@mat33code, @mat3bbc, solinit);

```
%Commands used to call BVP4C to solve Y and find unknown parameter g
xint=linspace(0,2.5673e+004,4096);  % solution space,  variable ξ  (approximately 2.3
%mm width)
solinit=bvpinit(linspace(0,2.5673e+004,4096), @mat3binit,  -4.8174e+000); % guesses
%at solution
sol=bvp4c(@mat33g1code, @mat3gbbc, solinit);      % output of BVP4c
Sxint=bvpval(sol, xint);   %  evaluate the numerical solution for given linespace
E3g1=Sxint(1,:).*2.8881e+003;   %EDb=2.8881e+003;  % solution for space charge
%field
```

```
% Initialization function used in BVP4C
function yinit = mat3binit(x,y)
                        % V/d*E_Db)=4.8173 normalized applied electric field
yinit = [4.8173
            0];


% Boundary condition function used in BVP4C
function res = mat3gbbc(ya, yb, g)
res = [ ya(2)-4.8173
        yb(2)-4.8173
        ya(1)+4.8174e+000];


% Boundary condition function used in BVP4C
function dydx = mat33g1code(x, y)
V = 3200;                       % Applied Voltage
H=.23;                          % crystal height, voltage bias distance
EDb= 2.8881e+003;               % Electric Field normalization parameter used in DelRe's
%paper
I0=1e-3;                        % peak intensity
s=1.06e-1;                      % ionization cross section cm2/joule
Beta=5.3333e-009;               % rate of thermal excitation
Ib=0;                           % background/control illumination
Id=Beta/s;                      % Dark Illumination
kDb=1.1162e+005;                % normalization for all x values.
xmax=.23*kDb;                   % xmax = 61684.0   2^16 = 65536
o=.115*kDb;                     % Gaussian Beam offset from ground plane *
%normalization
a=25e-4*kDb;          % Radius of Gaussian Beam*kDb=1.1162e4
Q=(1+I0/(Ib+Id)*exp(-((x-o)/a).^2));         % DelRe Equation (8) illumination term
Qp=(-2.*(x-o)./a.^2.*exp(-((x-o)./a).^2).*I0./(Ib+Id));       % Derivative of Q
% in the equation that follows, solving for y and y(2)=y(1)' and y(1) = y' so that y(2)=y'

dydx=[  y(2)
    y(1)+y(2).*y(1)+Qp./Q+Qp./Q.*y(2)-g./Q-2.*g./Q.*y(2)-g./Q.*y(2).*y(2)];


% Finish



% Commands used for BVP4C to solve for Y when not solving for g
xint=linspace(0,2.5673e+004,4096);
solinit=bvpinit(linspace(0,2.5673e+004,4096), @mat3binit);       % guesses at solution
sol=bvp4c(@mat33code, @mat3bbc, solinit);                       % output of BVP4c
Sxint=bvpval(sol, xint);                     %  evaluate the numerical solution for given
%linespace
```

E3=Sxint(1,:).*2.8881e+003;

```
% Initialization function used in BVP4C
function yinit = mat3binit(x,y)
                        % V/d*EDb)=4.8173 normalized applied electric field
yinit = [   4.8173
                0];


% Boundary condition function used in BVP4C
function res = mat3bbc(ya, yb)
res = [ ya(1)-4.8173
        yb(1)-4.8173 ];


% Boundary condition function used in BVP4C
function dydx = mat33code(x, y)
V = 3200;                       % Applied Voltage
H=.23;                          % crystal height, voltage bias distance
EDb= 2.8881e+003;               % Electric Field normalization parameter used in DelRe's
%paper
g = V/(H*EDb);                  % gmin DelRe Equation (23)
I0=1e-3;                        % peak intensity
s=1.06e-1;                      % ionization cross section cm2/joule
Beta=5.3333e-009;               % rate of thermal excitation
Ib=0;                           % background/control illumination time address
Id=Beta/s;                      % Dark Illumination
kDb=1.1162e+005;                % normalization for all x values.
xmax=.23*kDb;                   % xmax = 61684.0   2^16 = 65536
o=.115*kDb;                     % Gaussian Beam offset from ground plane *
%normalization
a=25e-4*kDb;            % Radius of Gaussian Beam*kDb=1.1162e4
Q=(1+I0/(Ib+Id)*exp(-((x-o)/a).^2));            % DelRe Equation (8) illumination term
Qp=(-2.*(x-o)./a.^2.*exp(-((x-o)./a).^2).*I0./(Ib+Id));         % Derivative of Q
% in the equation that follows, solving for y and y(2)=y(1)' and y(1) = y' so that y(2)=y'
dydx=[  y(2)
    y(1)+y(2).*y(1)+Qp./Q+Qp./Q.*y(2)-g./Q-2.*g./Q.*y(2)-g./Q.*y(2).*y(2)];
```

B.2 Digital Wideband Receiver Simulation

The input signal is a sequence of discrete time samples representing the GPS Pseudo-

random Noise (PN) code. It is generated using a random number generator. For

purposes of this model the PN code is 800 bits long, which represents 40 μseconds. The

GPS P-code clock rate is 10.23 Mbps and the bandwidth is approximately 20 MHz. The

PN code is correlated in the receiver to provide gain, which is part of the spread-spectrum

architecture. The complete sequence in this simulation is 1600 bits long. The PN code is

positioned somewhere within the 1600 bits, and the rest of the sequence is filled with

random ±1s. Note: 10.23e6/800 bits gives 78 μsec, thus each code bit was two bins long

due to Nyquist sampling. The PN code is mixed with time-varying interference

represented by sinusoidal functions. The sinusoids must be generated using frequencies

that can be resolved by the sample space, or the result of the Fourier transform is

broadband noise that cannot be notch filtered. It is interesting to note that it is easiest to

create this interference sequence using frequency components in a Fourier series, such as

$$x(n) = a_0 + \sum_{k=1}^{N/2} a(k)\cos\left(2\pi \frac{k}{N\,\Delta} t(n)\right) + b(k)\sin\left(2\pi \frac{k}{N\,\Delta} t(n)\right), \qquad \{\text{ B-1 }\}$$

and then apply it to the system as a time signal. However, the ultimate purpose of the

system is to determine the frequency components of the time signal, so this approach

"stacks the deck," so to speak. However, it would be difficult to think of creating these

narrow-band, single-frequency, time-correlated sequences in any other way. Note in

Equation { B-1 }that N is the number of bins in the sequence, and Δ is the differential

time, and the radian frequency, $\omega = 2\pi k/(N\Delta)$, is later determined by the DFT operation.

The fast Fourier transform simply determines the frequency component, $1/(N\Delta)$, that was

used to create the time signal. The same situation applies in the next section. AOA time

sequences are needed that have space-correlated phase delay. In the real world the phase

differences are due to the spatial location of the RF source, and in order to create

sequences for the digital simulation that work, AOA information is used to generate the

signal, then the AOA components are conveniently determined (and extracted) using the

Fourier transform.

The length of the tapped delay line is chosen to correspond to the Bragg-cell

length, or time aperture. The Bragg-cell time aperture was chosen to obtain 0.05%

frequency resolution, that is, 100 kHz resolution for the 20 MHz signal bandwidth. The

number of resolvable frequencies, or spots, for a Bragg cell is given by N=BW÷Δf,

where BW is the signal bandwidth; Δf is the frequency resolution; and in this case, N=

200 spots. The time aperture of the Bragg cell is given by T=N÷B=10 μsec. Note that

one cycle of the lowest resolvable frequency fills the Bragg-cell time aperture; that is,

1÷10 μsec = 1 kHz, and one cycle of the highest resolvable frequency fills two bits of the

sequence. For 200 spots, the number of bits representing the Bragg cell is 400 (20×10^6 ÷

$100 \times 10^3 \times 2$ bits ÷ resolvable spots).

As the bits are fed into the tapped delay line, a Fourier transform is performed.

The Fourier transform is filtered according to the power-limiting model. Two models

were used: one preserved signal phase and clipped amplitude while the other simply set

the value to zero. No difference was seen between these two types of filters.

B.2.1 Temporal Model

```
% This Matlab code was inspired from IDL source code written by Sung Choi, Gerald
%Falen, and also reference [8]
%constants
Nt=1600;        %total length of signal
Nc=768;         %size of code
Nc2=2;          %length of PN code bit
```

```matlab
Nc1=Nc/Nc2;
offset=50;              %amount of offset...Don't exceed 512
Nf=256;                 %size of Bragg cell, must go evenly into Nt, the signal window.
Np=1;           %number of interference sinusoids, must match Ap & Tp dimension
Ap(1:100)=100;          %amplitude of interference
AAA=linspace(1,100,100);            % Used for generating 100 frequencies
Tp=3.9608e+000;
%Tp=[200./AAA];                     %Period of interference generated by AAA. Tp is 200/1,
                        %200/2, 200/3...200/100,
X0=.2;          %lower limit of clipping threshold used for nonlinear function
DR=120;
X1=10^(DR/20);          %upper limit of clipping threshold used for nonlinear function

%Create a random code will be added to this sinusoidal signal. Note that each bit code is
%expanded to occupy NC2 time slots.
rand('state',1);   %set random generator state to #1. This is needed to repeat code,
%otherwise it changes for every call.
code1=(2*(round(rand(1,Nc1))))-1;   %random signal generated, round generates ones
%and zeros.
code(1:Nc)=0;
for i=1:Nc1   %loop to create code that has 4 bits length
   code((i*Nc2)-(Nc2-1):i*Nc2)=code1(i);  %This is the PN code used to correlate signal
   end
%Create bit noise
rand('state',2);
bitnoise1=(2*(round(rand(1,offset))))-1;
rand('state',3);
bitnoise2=(2*(round(rand(1,(Nt-Nc-offset+1)))))-1;

%add code and bitnoise to Signal: code is positioned @ offset
Signal(1:Nt)=0;
Signal(1:offset-1)=bitnoise1(1:offset-1);
Signal(offset:offset+(Nc-1))=code(1:Nc);
Signal(offset+Nc:Nt)=bitnoise2(1:Nt-Nc-offset+1);

%Add noise to Signal array, with length Nt, having Np=4 sinusoidal signals of amplitude
%Ap and period Tp.
%NoisySignal=Signal;
%for i=1:Np, NoisySignal=NoisySignal+Ap(i)*cos(2*pi/Tp(i)*(0:(Nt-1))-pi./8*i);
%Sinusoid is created using cos(2Pi*x/period).
%end
NoisySignal=awgn(Signal,-15, 'measured'); %new toolbox had AWGN function
figure(1)
```

subplot(2,3,1), plot(NoisySignal(1:Nt)), title('Noisy Signal'), AXIS([0 Nt min(NoisySignal) max(NoisySignal)])

%To represent the Bragg cell being filled, a vector, X, having Nc zeros at front and end
%and total length 2*Nf+Nt is
%created, i.e. the signal is centered between 2*Nf amount of zeros. The Bragg cell
%vector is filled sequentially with this
%vector, so that to start with it is all zeros except for the 1st bit, then one-bit-by-one-bit
%the Bragg cell is filled with the signal
%until it is filled with zeros on the other end except for the last bit.
X(1:Nt+2*Nf)=0;
X(Nf/2:Nf/2+Nt-1)=NoisySignal;

for i=1:(Nt+Nf-1),
   BraggCell(1:Nf)=X(i:i+Nf-1); %load Bragg cell with portion of the signal equivalent
%to transit time.
   Y=fft(BraggCell)./Nf;   %take Fourier transform of Bragg cell signal.
   Yout=nonlinear(Y, X0, X1); %call to nonlinear filter function
DetectorFiltered(i)=sum(Yout);   %sum of Fourier transform acts as detector,
%i.e. a signal integrator.
DetectorNoFilter(i)=sum(Y);
Maxmag(i)=max(Y); %check out the maximum magnitude of the input signal.
end
SizeD=length(DetectorFiltered);
subplot(2,3,3), plot(1:SizeD,real(DetectorFiltered))
AXIS([0 Nf+Nt min(real(DetectorFiltered)) max(real(DetectorFiltered))]), title('Summed
Output: Filtered')
subplot(2,3,2), plot(1:SizeD,real(DetectorNoFilter))
AXIS([0 Nf+Nt min(real(DetectorNoFilter)) max(real(DetectorNoFilter))]),
title('Summed Output: Unfiltered')

%The following plots the frequency components of the summed unfiltered signal.
Fourier=fft(NoisySignal(501:(500+Nf)));

N=length(Fourier);
%Fourier(1)=0;
Power=(abs(Fourier(1:N/2+1)).^2)/(max(abs(Fourier))^2);
nyquist = 20/2;
freq = (1:N/2+1).*(nyquist/(N/2));
period = 1./freq;
subplot(2,3,4), plot(freq(1:N/2+1),Power(1:N/2+1),'*')
axis([0 nyquist 0 max(Power)])
title('Power Spectrum'), xlabel('MHz')

%The following "for loop" correlates the code signal with the system output.
%The correlation function output is a 2X2 matrix called Dummyarray. (The
%autocorrelation coefficient is at indices
%(1,1 & 2,2) correlation coefficient is at indices (1,2 & 2,1).
%The correlation coefficient at index (1,2) is saved in an array called Xcoef.
%Correlation then steps up one unit, so that the code signal is correlated with the original
%signal + one bit.
%This process continues until the whole signal has been correlated (up to Nt-Nc index).
%The correlation coefficients are then plotted to indicate a peak.

```
for i = 1:(Nf+Nc-1),
    Dummyarray=corrcoef(DetectorFiltered(i:i+(Nc-1)),code(1:Nc));
    Dummyarray2=corrcoef(DetectorNoFilter(i:i+(Nc-1)),code(1:Nc));
    Xcoef(i)=Dummyarray(2,1);
    Xcoef2(i)=Dummyarray2(2,1);
    clear Dummyarray;
    clear Dummyarray2;
    end
    subplot(2,3,6), plot(1:(Nf+Nc-1),real(Xcoef(1:(Nf+Nc-1))))
    title('Correlation Filtered')
    subplot(2,3,5), plot(1:(Nf+Nc-1),real(Xcoef2(1:(Nf+Nc-1))))
    title('Correlation Unfiltered')

    figure(5)
    plot((1:Nf),fftshift(abs(Fourier)), '*');
```

%nonlinear function
function Yout=nonlinear(Y, X0, X1)
%nonlinear   The nonlinear transversal filter.
%nonlinear(Y, X0, X1) Y is the Fourier transform of a signal, X0 is lower threshold
%limit, X1 is upper threshold limit.
%Logic is used to compare the input values and map them to the appropriate output
%value.
%Maps one-to-one until reaching a value X0. Then maps as X0/Y i.e. 1/Y attenuation
%occurs until input exceeds X1 value.
%The leakage component maps one to one thereafter, but is diminished by the value 1-
X0^2/X1^2.

```
N=length(Y);    %determine length of vector Y.
for i=1:N        %Logic uses "if loop" to compare input and map to appropriate output.
if abs(Y(i)) <= X0
    Yout(i)=Y(i);                %maps one to one
 elseif abs(Y(i)) <= X1
```

```
    Yout(i) = X0^2.*Y(i)./((abs(Y(i))).^2);      %nonlinear mapping X0/Y(i): the bigger
Y(i) gets the smaller Yout(i), due to polarizer.
else
    Yout(i) = (X0^2/X1^2).*Y(i);                  %leakage component maps one to one, but
diminished by 1-X0^2/X1^2
end
end
```

B.3 Digital Wideband Receiver Simulation:
Spatial and Temporal Model

```
% This mixes a signal on-axis, and a Noise source off-axis.
% This approach did not work with just clipping and summing all points on a 2-D array
% The only way that I could get correlation with a true broad band interferer was to
% isolate the DC row in the DFT corresponding to the Signal AOA and use it by itself.
% In other words, clipping and then summing all points in the DFT does not work for this
% model, because the total noise was too great.
% constants:
Nt=1024;        %total length of signal
Nc=512;         %size of code
Nc2=2;          %length of PN code bit
Nc1=Nc/Nc2;
offset=50;      %amount of offset...Don't exceed 512
Nf=256;                 %size of Bragg cell, must go evenly into Nt, the signal window.
Np=1;           %number of interference sinusoids, must match Ap & Tp dimension
Rt=16;   % Number of Bragg Cell channels; i.e. Phased Array Receiver
Ap(1:100)=100;          %amplitude of interference
AAA=linspace(1,Nf,Nf); % Used for generating 100 frequencies
Tp=16;
%Tp=3.9608e+000;
Tp2=13.356;
AOA=4;  % 0=DC, 1 = first resolvable AOA, 2 = second resolvable AOA, ... Rt/2 =
%highest resolvable AOA.
AOAnoise=6; % see above, this is used for the noise.
%Tp=[Nf./AAA(32)];                        %Period of interference generated by AAA.
%Tp is 200/1, 200/2, 200/3...200/100,
X0=0.003;     %lower limit of clipping threshold used for nonlinear function
DR=600;
X1=10^(DR/20);                %upper limit of clipping threshold used for nonlinear
%function
% End Constants
```

```matlab
% Generation of PN Signal (code) vector (+30 dB AWGN representing channel goes
%here).
% Note that each bit code is expanded to occupy NC2 time slots.
rand('state',2);   %set random generator state to #1. This is needed to repeat code,
%otherwise it changes for every call.
code1=(2*(round(rand(1,Nc1))))-1;   %random signal generated, round generates ones
%and zeros, 2*#-1 gives +/- 1 values.
code(1:Nc)=0;   % used to expand code to a length determined by the constant Nc2
for i=1:Nc1   %loop to create code that has Nc2 bits length
    code((i*Nc2)-(Nc2-1):i*Nc2)=code1(i);  %This is the PN code used to correlate signal
    end
%Create bit noise that fills the space between the shorter code length and total signal
%length (we are looking for the position of the code as a test of the system).
rand('state',3);
bitnoise1=(2*(round(rand(1,offset))))-1;
rand('state',4);
bitnoise2=(2*(round(rand(1,(Nt-Nc-offset+1)))))-1;

%add code and bitnoise to Signal: code is positioned @ offset
Signal(1:Nt)=0;
Signal(1:offset-1)=bitnoise1(1:offset-1);
Signal(offset:offset+(Nc-1))=code(1:Nc);
Signal(offset+Nc:Nt)=bitnoise2(1:Nt-Nc-offset+1);
%Signal=awgn(Signal,10,'measured');




% The transformed domain has 4 quadrants, the center is the nyquist value of each
%dimension.  How is this value applied?
% The position of information in quadrants determine the +/- direction of the AOA.
% Assume that DC term + 7 AOA is one quadrant and Nyquist + 7 AOA is the other
%quadrant, this give Length/2 for each quadrant.
% Add phase to the broadband signal proportional to angle of arrival (AOA).
% The (AOA) phase is unique for each frequency (or wavelength) so the signal must be
%constructed in the
% frequency domain.  There are Rt channels in the Bragg cell.  Since each channel
%corresponds to a resolvable AOA
% in the Fourier transform plane, then the AOA information will be constructed there.
%Remember that you have to
% include the negative and positive frequencies (complex conjugate).
SignalFreq=fft(Signal);
SignalFreqP(1:Rt,1:Nt)=0;
SignalFreqP(AOA+1,1:Nt/2)=SignalFreq(1:Nt/2).*Rt;
SignalFreqP(Rt-(AOA-1),(Nt/2+1):Nt)=SignalFreq((Nt/2+1):Nt).*Rt;
```

% The following commented lines is an alternate approach, where the nyquist term is
%included with the DC term.
% SignalFreqP(AOA+1,1:(Nt/2+1))=SignalFreq(1:(Nt/2+1)).*Rt;
% SignalFreqP((Rt-(AOA-1)),(Nt/2+2):Nt)=SignalFreq((Nt/2+2):Nt).*Rt;

% Take signal back to time domain
SignalP=ifft2(SignalFreqP); % inverse to time domain
% SignalRecovered=SignalP(1,:)+(conj(SignalP(Rt,:)).*SignalP(2,:));

% Create angle of arrival noise signal
rand('state',3);   %set random generator state to #1. This is needed to repeat code,
%otherwise it changes for every call.
Noise=(2*(round(rand(1,Nt))))-1;   %random signal generated, round generates ones and
%zeros, 2*#-1 gives +/- 1 values.
Noise=awgn(Noise,-55,'measured');
NoiseFreq=fft(Noise);
NoiseFreqP(1:Rt,1:Nt)=0;
NoiseFreqP(AOAnoise+1,1:Nt/2)=NoiseFreq(1:Nt/2).*Rt;
NoiseFreqP(Rt-(AOAnoise-1),(Nt/2+1):Nt)=NoiseFreq((Nt/2+1):Nt).*Rt;
NoiseP=ifft2(NoiseFreqP);

%combine signal and noise
NoisySignalP=real(SignalP)+real(NoiseP);
NoisySignalFreqP=fft2(NoisySignalP);

%Bragg: To represent the Bragg cell being filled, a vector, X, having Nc zeros at front
%and end and total length 2*Nf+Nt is
%created, i.e. the signal is centered between 2*Nf amount of zeros. The Bragg cell
%vector is filled sequentially with this
%vector, so that to start with it is all zeros except for the 1st bit, then one-bit-by-one-bit
%the Bragg cell is filled with the signal
%until it is filled with zeros on the other end except for the last bit.
X(1:Rt,1:Nt+2*Nf)=0;
for i=1:Rt
X(i,Nf/2:Nf/2+Nt-1)=NoisySignalP(i,1:Nt);
end

for i=1:(Nt+Nf-1),
  for j=1:Rt
   BraggCell(j,1:Nf)=X(j,i:i+Nf-1); %load Bragg cell with portion of the signal
%equivalent to transit time.
end

169

```
   Y=fft2(BraggCell)./Nf./Rt; %take Fourier transform of Bragg cell signal.
      Yout=nonlinear2(Y, X0, X1); %call to nonlinear filter function

DetectorFiltered(i)=sum(sum(Yout));                %sum of Fourier transform acts as
%detector, i.e. a signal integrator.
DetectorNoFilter(i)=sum(sum(Y));
Maxmag(i)=max(max(Y));    %check out the maximum magnitude of the input signal.
end
SizeD=length(DetectorFiltered);
subplot(2,3,3),  plot(1:SizeD,real(DetectorFiltered))
AXIS([0 Nf+Nt min(real(DetectorFiltered)) max(real(DetectorFiltered))]), title('Summed
Output: Filtered')
subplot(2,3,2),   plot(1:SizeD,real(DetectorNoFilter))
AXIS([0 Nf+Nt min(real(DetectorNoFilter)) max(real(DetectorNoFilter))]),
title('Summed Output: Unfiltered')


%The following "for loop" correlates the code signal with the system output.
%The correlation function output is a 2X2 matrix called Dummyarray. (The
%autocorrelation coefficient is at indices
%(1,1 & 2,2) correlation coefficient is at indices (1,2 & 2,1).
%The correlation coefficient at index (1,2) is saved in an array called Xcoef.
%Correlation then steps up one unit, so that the code signal is correlated with the
%original signal + one bit.
%This process continues until the whole signal has been correlated (up to Nt-Nc index).
%The correlation coefficients are then plotted to indicate a peak.

for i = 1:(Nf+Nc-1),
   Dummyarray=corrcoef(DetectorFiltered(i:i+(Nc-1))/Rt,code(1:Nc));
   Dummyarray2=corrcoef(DetectorNoFilter(i:i+(Nc-1))/Rt,code(1:Nc));
   Xcoef(i)=Dummyarray(2,1);
   Xcoef2(i)=Dummyarray2(2,1);
   clear Dummyarray;
   clear Dummyarray2;
   end
   subplot(2,3,6), plot(1:(Nf+Nc-1),real(Xcoef(1:(Nf+Nc-1))))
   title('Correlation Filtered')
   subplot(2,3,5), plot(1:(Nf+Nc-1),real(Xcoef2(1:(Nf+Nc-1))))
   title('Correlation Unfiltered')
% end
```

Bibliography

[1] J. Rhea, "The year of decision for GPS vulnerability," Military & Aerospace Electronics April 1998.

[2] W.H. Steier, J. Kumar, and M. Ziari, "Infrared Power Limiting and Self-Switching in CdTe," Appl. Phys. Lett. **53**, No. 10, (840-841), 1988.

[3] S.S. Soliman and M.D. Srinath, *Continuous and Discrete Signals and Systems*, Prentice Hall, Englewood Cliffs, NJ, 1990.

[4] C.D. McGillem and G.R. Cooper, *Continuous and Discrete Signal and System Analysis*, 2nd ed., Holt, Rinehart and Winston, New York, 1984.

[5] J. W. Goodman, *Introduction to Fourier Optics*, 2nd ed., McGraw-Hill Co., Inc., New York, 1996.

[6] J.D. Gaskill, *Linear Systems, Fourier Transforms, and Optics*, John Wiley & Sons, Inc., New York, 1978.

[7] P.P. Banerjee and T.C. Poon, *Principles of Applied Optics*, Irwin Inc. Homewood, IL 1991.

[8] J.G. Proakis and M. Salehi, *Contemporary Communication Systems using Matlab®*, PWS Publishing Co. Boston, MA, 1998.

[9] G.R. Cooper and C.D. McGillem, *Modern Communications and Spread Spectrum*, McGraw-Hill, Inc., New York, 1986.

[10] Matlab®, BVP4C function, Version 6.0.088, Release 12, Mathworks Inc., Natick, MA, 2001.

[11] A. VanderLugt, "Optical Transversal Processor for Notch Filtering," Opt. Eng., **23**, (312), 1984.

[12] I.C. Chang, "Acoustooptic Devices and Applications," IEEE Trans. On Sonics and Ultrasonics, Vol. SU-23, **1**, (2-22), January 1976.

[13] C.R. Scott, *Field Theory of Acousto-Optic Signal Processing Devices*, Artech House, Boston, MA, 1992.

[14] A. Korpel, *Acousto-Optics*, 2nd ed., Marcel Dekker, Inc., New York, 1997.

[15] D.J. Torrieri, "Introduction to Acousto-Optic Interaction Theory," *Acousto-optic Signal Processing, Theory and Implementation*, 2nd ed., N.J. Berg and J.M. Pellegrino, (eds.), Marcel Dekker, Inc. New York, (3-20), 1996.

[16] GLAD©, Version 4.5, Applied Optics Research, Austin TX, glad@aor.com, 2000.

[17] W.R. Klein and B.D. Cook, "Unified Approach to Ultrasonic Light Diffraction," IEEE Trans. Sonics Ultrasonics, SU-14, (723-733), July 1967.

[18] Harris Corporation, "Acousto-Optic Device Technology: Basic Principles," *Acousto-optic Signal Processing, Theory and Implementation*, 2nd ed, N.J. Berg and J.M. Pellegrino, (eds.), Marcel Dekker, Inc., New York, (21-45), 1996.

[19] H. Kogelnik, "Coupled Wave Theory for Thick Hologram Gratings," Bell System Technical Journal, **48**, (2909-2947), 1969.

[20] P. Hariharan, *Optical Holography Principles, Techniques, and Applications*, 2nd ed., Cambridge University Press, New York, 1996.

[21] D. Yevick and L. Thylén, "Analysis of gratings by the beam-propagation method," J. Opt. Soc. Am., **72**, No. 8, (1084-1089), 1982.

[22] J.M. Jarem and P.P. Banerjee, *Computational Methods for Electromagnetic and Optical Systems*, Marcel Dekker, Inc., New York, 2000.

[23] J.A Lascody, "Narrowband Interference Suppression in Spread Spectrum Communication Systems," Masters thesis, Air Force Institute of Technology, Dayton, OH, 1995.

[24] C.B. Madden, "Effects of Jamming and Excision Filtering Upon Error Rates and Detectability of a Spread Spectrum Communications System," Masters thesis, Air Force Institute of Technology, Dayton, OH, 1995.

[25] G.L Falen, "Analysis and Simulation of Narrowband GPS Jamming Using Digital Excision Temporal Filtering," Masters thesis, Air Force Institute of Technology, Dayton, OH, 1994.

[26] D. Casasent, "Optical Information-Processing Applications of Acousto-Optics," *Acousto-optic Signal Processing, Theory and Implementation*, 2nd ed., N.J. Berg and J.M. Pellegrino, (eds.), Marcel Dekker, Inc., New York, (305-345), 1996.

[27] L.B. Lambert, M. Arm, and A. Aimette, "Electro-optical Signal Processors for Phased Array Antennas," *Optical and Electro-optical Information Processing*, ed. Tippett, Berkowitz, Clapp, Koester, and Vanderburgh, 1964.

[28] J. L. Erickson, "Linear Acousto-Optic Filters for Programmable and Adaptive Filtering," Ph.D. Thesis, Stanford University Electrical Engineering Department, June 1981.

[29] A. VanderLugt, *Optical Signal Processing,* John Wiley & Sons, Inc., New York, 1992.

[30] A. VanderLugt, "The Theory of Acousto-Optic Spectrum Analyzers," *Acousto-optic Signal Processing, Theory and Implementation*, 2nd ed., N.J. Berg and J.M. Pellegrino, (eds.), Marcel Dekker, Inc. New York, (100-138), 1996.

[31] A. VanderLugt and R. N. Ward, *Adaptive presort processing*, Final Technical Report, RL-TR-91-253, DTIC, October, 1991.

[32] J.L. Erickson, "Optical excisor performance limits versus improved signal detection," SPIE, **639**, Optical Information Processing II, 1986.

[33] R.W. Brandstetter and P. G. Grieve, "Excision of Interference from Radio Frequency Signals by Means of a Recursive Optical Notching Filter," Optical Engineering, **29**, No. 7, (804-815), July 1990.

[34] J.H. Hong and T.Y. Chang, "Adaptive Signal Processing with Photorefractive Systems," SPIE **2489**, (36-44).

[35] J.H. Hong and D. Psaltis, "Acoustooptic Adaptive Signal Processing," SPIE **551** Adaptive Optics, 1985.

[36] J.H. Hong, "Applications of Photorefractors for Signal Processing," *Photorefractive Materials, Effects, and Applications*, P. Yeh and C. Gu (eds.), SPIE Optical Engineering Press, Bellingham, WA, 1994.

[37] A. Yariv and P. Yeh, *Optical Waves in Crystals,* John Wiley & Sons Inc., New York, 1984.

[38] B.E.A. Saleh and M.C. Teich, *Fundamentals of Photonics,* John Wiley & Sons Inc., New York, 1991.

[39] P. Yeh, *Introduction to Photorefractive Nonlinear Optics*, John Wiley & Sons, Inc., New York, 1992.

[40] R.W. Boyd, *Nonlinear Optics*, Academic Press, Inc., Boston, MA, 1992.

[41] J.H. Hong and T.Y. Chang "Adaptive RF Notch Filtering Using Photorefractive Two-Beam Coupling," IEEE J. of Quantum Elect. **30**, No.2, (314-317), 1994.

[42] T.Y. Chang, I. McMichael, J.H. Hong, M. Khoshnevisan, "Electro-Optic Power Limiter: Broadband, Self-Actuating Optical Limiter for Visible and Infrared Radiation," Materials Research Society Symposium Proceedings **374**, (61-71), 1995.

[43] H. Rajbenbach, J.M. Verdiell, and J.P. Huignard, "Visualization of Electrical Domains in Semi-insulating GaAs:Cr and Potential Use for Variable Grating Mode Operation," Appl. Phys. Lett. **53**, No.7, (541-544), 1988.

[44] J. Guo, T.Y. Chang, I. McMichael, J. Ma, and J.H. Hong, "Light -Controlled Electro-Optic Power Limiter with a $Bi_{12}SiO_{20}$ Crystal," Opt. Lett., **24**, No. 14, (981-983), 1999.

[45] F. Vachss and L. Hesselink, "Nonlinear Photorefractive Response at High Modulation Depths," J. Opt. Soc. Am. A, **5**, No. 5, 1988.

[46] R.A. Mullen and R.W. Hellwarth, "Optical Measurement of the Photorefractive Parameters of $Bi_{12}SiO_{20}$," J. Appl. Phys. **58**, (40-44), 1985.

[47] M.B. Klein and G.C. Valley, "Beam Coupling in $BaTiO_3$ at 442nm," J. Appl. Phys. **57**, (4901-4905) 1985.

[48] A. Bledowski, J. Otten, and K.H. Ringhofer, "Photorefractive Hologram Writing with Modulation I," Optics Letters, **16**, No. 9, 1991.

[49] P. Gunter, "Holography, Coherent Light Amplification and Optical Phase Conjugation with Photorefractive Materials," Physics Reports (Review Section of Physics Letters), **93**, No. 4, (199-299), 1982.

[50] N.V. Kukhtarev, V. B. Markow, S.G. Odulov, and V.L. Vinetskii, "Holographic Storage in Electrooptic Crystals. I. Steady State," Ferroelecrics **22**, (949-960), 1979.

[51] N. Singh, S.P. Nadar, and P.P. Banerjee, "Time-Dependent Nonlinear Photorefractive Response to Sinusoidal Intensity Gratings," Optics Comm. **136**, (487-495), 1997.

[52] M. Segev, B. Crosignani, A. Yariv, and B. Fischer, "Spatial Solitons in Photorefractive Media," Physical Review Letters, **68**, No. 7, (923-926), 1992.

[53] G.C Valley, M. Segev, B. Crosignani, A.Yariv, M.M. Fejer, and M.C. Bashaw, "Dark and Bright Photovoltaic Spatial Solitons," Phys. Rev. A, **50**, No. 6, 1994.

[54] E. DelRe, A. Ciattoni, B. Crosignani, and M. Tamburrini, "Approach to Space-Charge Field Description in Photorefractive Crystals," J. of Opt. Soc. of Am. B, **15**, No. 5, (1469-1475), 1998.

[55] J.N. Lee, R. B. Brown, and A.E. Craig, "High stability configuration for an acoustooptic heterodyne rf spectrum analyzer using slow shear TeO_2," Appl. Opt. **28**, No. 18, (3796-3799), 1989.

[56] N.A. Riza, "Optically efficient interferometric acousto-optic architecture for spectrum analysis," Appl. Opt., **31**, No. 17, (3194-3196), 1992.

[57] J.M. Schmitt, "Compact in-line interferometer for low-coherence reflectometry," Opt. Lett., **20**, No.4, (419-421), 1995.

[58] W. Däschner, P. Long, R. Stein, C. Wu, and S.H. Lee, "Cost-effective mass fabrication of multilevel diffractive optical elements by use of a single optical exposure with a gray-scale mask on high-energy beam-sensitive glass," Appl. Opt. **36**, No. 20 (4675-4680) 1997.

[59] M.D. Koontz, "Miniature Interferometric Spectrum Analyzer," SPIE **639**, (126-130), 1986.